Technical Report Documentation Page

1. Report No.	2. Government Accession No.	3. Recipient's Catalog No.
FHWA/TX-88/1215-1F		

4. Title and Subtitle
Computer Analysis of Falling-Weight Deflectometer Data, Part I: Vertical Displacement Computations on the Surface of a Uniform (One-Layer) Half-Space Due to an Oscillating Surface Pressure Distribution

5. Report Date
November 1988

6. Performing Organization Code

7. Author(s)
Allen H. Magnuson

8. Performing Organization Report No.
Research Report 1215-1F

9. Performing Organization Name and Address
Texas Transportation Institute
Texas A&M University System
CE/TTI Building, Room 508
College Station, Texas 77843

10. Work Unit No. (TRAIS)

11. Contract or Grant No.
2/3-18-88-1175, 2-10-88/8-1215

12. Sponsoring Agency Name and Address
State Department of Highways and Public Transportation
Maintenance Operations & Transportation Planning Divisions
P. O. Box 5051
Austin, Texas 78763

13. Type of Report and Period Covered
Final - September 1987 November 1988

14. Sponsoring Agency Code

15. Supplementary Notes
Research performed in cooperation with DOT, FHWA.
Research Study Title: Dynamic Analysis Techniques for Falling Weight Deflectometer

16. Abstract

A computer algorithm SCALPOT, consisting of a set of programs and linked files, has been developed that computes responses for physical and geometrical conditions simulating the Dynatest Falling-Weight Deflectometer. Related work on dynamic analysis of layered elastic and viscoelastic media is reviewed. The pavement dynamics problem as measured by the FWD is shown to be a near-field or intermediate-field problem requiring different integration techniques than far-field problems arising in seismic work. Integration of the formal solution is shown to be best treated by direct numerical integration using a newly developed method of estimating truncation error. The integral must be evaluated numerically to a specified level of accuracy, taking into account the effect of truncation of the infinite upper limit, the oscillations due to the Bessel function, the slowness of the convergence of the integral, and singular behavior of the integrand because of pole and branch points. The integrals are broken up into three terms: the first one includes all the pole and branch singularities. The second term integrates between zero-crossings of the Bessel function up to the truncation point that occurs at a specified number of cycles of oscillation of the integrand. The third term is the truncation error estimate that uses a modified form of Zhongjin's (1987) method. The computed results are for a uniform (unlayered) half-space, although the integration method was designed to be applicable to the multilayered problem which will be treated in a subsequent effort. The program has been verified using the results of three previous independent investigations.

17. Key Words	18. Distribution Statement
Nondestructive Testing of Pavements, Nondestructive Evaluation of Pavements, Pavement Dynamics, Viscoelastic Half-Space Dynamics, Asphaltic Concrete Pavement Performance, Asphaltic Concrete Evaluation	No restrictions. This document is available to the public through the National Technical Information Service 5285 Port Royal Road Springfield, Virginia 22161

19. Security Classif. (of this report)	20. Security Classif. (of this page)	21. No. of Pages	22. Price
Unclassified-Unlimited	Unclassified	92	

COMPUTER ANALYSIS OF FALLING-WEIGHT DEFLECTOMETER DATA, PART I: VERTICAL DISPLACEMENT COMPUTATIONS ON THE SURFACE OF A UNIFORM (ONE-LAYER) HALF-SPACE DUE TO AN OSCILLATING SURFACE PRESSURE DISTRIBUTION

by
Allen H. Magnuson

Research Report 1215-1F
Research Study #2/3-18-88-1175 & 2-10-88/8-1215

Sponsored by:
Texas State Department of Highways and Public Transportation

In
Cooperation with The U.S. Department of Transportation
Federal Highway Administration

Texas Transportation Institute
Texas A&M University
College Station, Texas 77843

August 1988

METRIC (SI*) CONVERSION FACTORS

APPROXIMATE CONVERSIONS TO SI UNITS

Symbol	When You Know	Multiply By	To Find	Symbol
LENGTH				
in	inches	2.54	millimetres	mm
ft	feet	0.3048	metres	m
yd	yards	0.914	metres	m
mi	miles	1.61	kilometres	km
AREA				
in²	square inches	645.2	millimetres squared	mm²
ft²	square feet	0.0929	metres squared	m²
yd²	square yards	0.836	metres squared	m²
mi²	square miles	2.59	kilometres squared	km²
ac	acres	0.395	hectares	ha
MASS (weight)				
oz	ounces	28.35	grams	g
lb	pounds	0.454	kilograms	kg
T	short tons (2000 lb)	0.907	megagrams	Mg
VOLUME				
fl oz	fluid ounces	29.57	millilitres	mL
gal	gallons	3.785	litres	L
ft³	cubic feet	0.0328	metres cubed	m³
yd³	cubic yards	0.0765	metres cubed	m³

NOTE: Volumes greater than 1000 L shall be shown in m³.

TEMPERATURE (exact)

°F	Fahrenheit temperature	5/9 (after subtracting 32)	Celsius temperature	°C

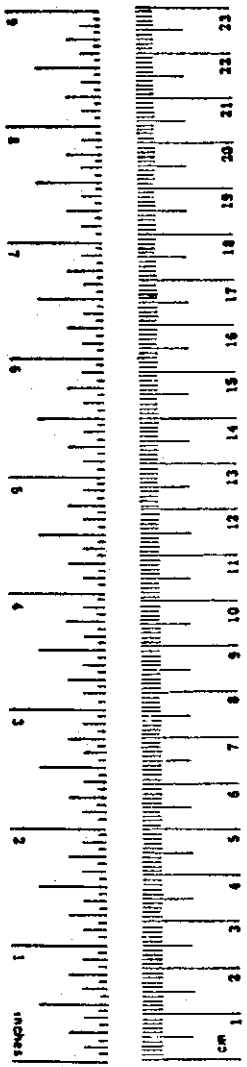

APPROXIMATE CONVERSIONS TO SI UNITS

Symbol	When You Know	Multiply By	To Find	Symbol
LENGTH				
mm	millimetres	0.039	inches	in
m	metres	3.28	feet	ft
m	metres	1.09	yards	yd
km	kilometres	0.621	miles	mi
AREA				
mm²	millimetres squared	0.0016	square inches	in²
m²	metres squared	10.764	square feet	ft²
km²	kilometres squared	0.39	square miles	mi²
ha	hectores (10 000 m²)	2.53	acres	ac
MASS (weight)				
g	grams	0.0353	ounces	oz
kg	kilograms	2.205	pounds	lb
Mg	megagrams (1 000 kg)	1.103	short tons	T
VOLUME				
mL	millilitres	0.034	fluid ounces	fl oz
L	litres	0.264	gallons	gal
m³	metres cubed	35.315	cubic feet	ft³
m³	metres cubed	1.308	cubic yards	yd³

TEMPERATURE (exact)

°C	Celsius temperature	9/5 (then add 32)	Fahrenheit temperature	°F

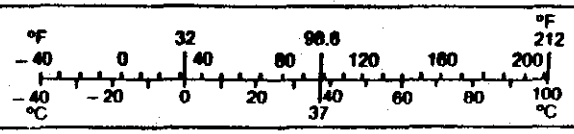

These factors conform to the requirement of FHWA Order 5190.1A.

* SI is the symbol for the International System of Measurements

ABSTRACT

A computer algorithm SCALPOT, consisting of a set of programs and linked files, has been developed that computes responses for physical and geometrical conditions simulating the Dynatest Falling-Weight Deflectometer. Related work on dynamic analysis of layered elastic and viscoelastic media is reviewed. The pavement dynamics problem as measured by the FWD is shown to be a near-field or intermediate-field problem requiring different integration techniques than far-field problems arising in seismic work. Integration of the formal solution is shown to be best treated by direct numerical integration using a newly developed method of estimating truncation error. The integral must be evaluated numerically to a specified level of accuracy, taking into account the effect of truncation of the infinite upper limit, the oscillations due to the Bessel function, the slowness of the convergence of the integral, and singular behavior of the integrand because of pole and branch points. The integrals are broken up into three terms: the first one includes all the pole and branch singularities. The second term integrates between zero-crossings of the Bessel function up to the truncation point that occurs at a specified number of cycles of oscillation of the integrand. The third term is the truncation error estimate that uses a modified form of Zhongjin's (1987) method. The computed results are for a uniform (unlayered) half-space, although the integration method was designed to be applicable to the multilayered problem which will be treated in a subsequent effort. The program has been verified using the results of three previous independent investigations.

ACKNOWLEDGEMENT

The author wishes to thank the project technical coordinators, Mr. Richard Rogers and Mr. Robert Briggs of the Texas State Department of Highways and Public Transportation, for sponsoring this work. The author also wishes to acknowledge Dr. Robert Lytton of the Texas Transportation Institute for his suggestions, guidance, interest, and for his encouragement without which this work could not have been accomplished.

DISCLAIMER

The contents of this report reflect the views of the author who is responsible for the opinions, findings, and conclusions presented herein. The contents do not necessarily reflect the official views or policies of the Federal Highway Administration or the Texas State Department of Highways and Public Transportation. This report does not constitute a standard, specification, or regulation.

Table of Contents

		Page
	Abstract	iii
	List of Tables	vii
	List of Figures	viii
I	Introduction	1
II	Related Work	9
III	Derivation of Integral Expressions For Surface Displacement	16
IV	Method of Integration	29
V	Development of Computer Programs	42
VI	Results	50
VII	Summary and Conclusions	77
	References	80

LIST OF TABLES

Table		Page
1	Convergence of Integral of Bessel Function	32
2	Numerical Integration of J_o Bessel Function Based on Zero Crossings	33
3	Wang's (1975) Computed Dimensionless Vertical Displacement on the Displacement on the Surface of an Elastic Half-Space as a Function of Dimensionless Distance (From Apsel and Luco, 1983)	59

LIST OF FIGURES

Figure		Page
1	Location of Monitored Highway Test Sites Selector for Dynamic Analysis Using Falling-Weight Deflectometer Data . .	4
2	Magnitude of Surface Deflection Versus Frequency for TTI Highway Station 9 for FWD Data and Predicted Values for Two Damping Ratios	6
3	Phase Angle of Surface Deflection Versus Frequency for r = 0 for TTI Highway Station 9 for FWD Data and Predicted Computed Values	7
4	Phase Angle of Surface Deflection Versus Frequency for r = 6 ft. for TTI Highway Section 9 for FWD Data and Computer Predictions	8
5	Layered Viscoelastic Half-Space Showing Geometry and Physical Characteristics of Each Layer.	12
6	Half-Space Problem with Axial Symmetry.	17
7	Superposition Integral Geometry	26
8	Bessel Function of Order Zero and One	30
9	Plot of Non-Oscillatory Part of Integrand as a Function of Frequency and Wavenumber for the Uniform Half-Space and for Two-Length and Three-Layer Half-Spaces.	35
10	Integration Limits and Their Relation to the Oscillatory Integrand	38
11	Graphical Interpretation of Zhongjin's Method Over One Cycle of Oscillation.	40
12	Program Structure for SCR.C File for Computing Response from Uniform Load for r = 0	43
13	Program Structures for DELTA.C File for Computing Responses to Point Load	44
14	Programs Structure for SUP.C File for Computing Responses from Uniform Load for Field Point Outside Load Disk (r>a) . .	45
15	Surface Elements for nn=1, 2, 5, 9.	49

16a In-Phase Dimensionless Normal Displacement for r=0 and Univorm Pressure Distribution Versus Dimensionless Frequency for Poisson's Ratio of 0, 1/4, 1/3, and 1/2 (from Sung, 1954). 52

16b Out-of-Phase Dimensionless Normal Displacement for r=0 and Uniform Pressure Distribution Versus Dimensionless Frequency for Poisson's Ratio of 0, 1/4, 1/3, and 1/2 (from Sung, 1954). 53

17 In-Phase Dimensionless Normal Displacement for r=0 and Uniform Pressure Distribution for Poisson's Ratio of 1/4: Comparison of Theory and Computed Values. 54

18 Out-of-Phase Dimensionless Normal Displacement for r=0 and Uniform Pressure Distribution for Poisson's Ratio of 1/4: Comparison of Theory and Computed Values. 55

19 Dimensionless Magnitude of Normal Displacement for r=0 and Uniform Pressure Distribution for Poisson's Ratio of 1/3: Comparison of Theory and Computed Values. 56

20 Dimensionless Magnitude of Normal Displacement for r = 0 and Uniform Pressure Distribution for Poisson's Ratio of 1/3: Comparison of Theory and Computed Values on Expanded Scale. 57

21 Phase Angle of Normal Displacement for r = 0 and Uniform Pressure Distribution for Poisson's Ratio of 1/3: Comparison of Theory and Computed Values. 58

22 Real and Imaginary Components of Dimensionless Normal Surface Displacement Versus Dimensionless Distance (r_o) for a Point Surface Load on an Elastic Half-Space Poisson's Ratio = 0.33 (From Wang, 1975). 60

23 Magnitude of Dimensionless Normal Surface Displacement Versus Dimensionless Distance (r_o) for a Point Surface Load on an Elastic Half-space; Poisson's Ratio = 0.33 (From Wang, 1975). 61

24 Phase Angle of Dimensionless Normal Surface Displacement Versus Dimensionless Distance (r_o) for a Point Surface Load on an Elastic Half-space; Poissons Ratio = 0.33. . . 62

25 Magnitude of Dimensionless Normal Surface Displacement Versus Dimensionless Distance (r_o) for a Point Surface Load; (Poisson's Ratio - 0.33) Comparison of Theory and Computed Values. 64

26 Phase Angle of Normal Surface Displacement Versus Dimensionless Distance (r_o for a Point Surface Load; (Poisson's Ratio = 0.33); Comparison of Theory and Computed Values. 65

27 Magnitude of Dimensionless Normal Surface Displacement at r=0 Versus Dimensionless Frequency (a_o) for a Uniform Pressure Distribution (Poisson's Ratio = 0.3); Comparison of Computed Values. 67

28 Phase Angle of Normal Surface Displacement at r = 0 Versus Dimensionless Frequency (a_o) for a Uniform Pressure Distribution (Poisson's Ratio = 0.3); Comparison of Computed Values. 68

29 Magnitude of Normal Surface Displacement at r = 6 ft. Versus Dimensionless Frequency (r_o) for a Uniform Pressure Distribution (Poisson's Ratio = 0.3); Comparison of Computed Values. 69

30 Magnitude of Normal Surface Displacement at r = 1 ft. V Versus Dimensionless Frequency (r_o) for a Uniform Pressure Distribution (Poisson's Ratio = 0.3); Comparison of Computed Values. 70

31 Magnitude of Normal Surface Displacement at r = 1 ft. Versus Dimensionless Frequency (r_o) for a Uniform Pressure Distribution (Poisson's Rate = 0.3); Comparison of Computed Values. 71

32 Phase Angle of Normal Surface Displacement at r = 1 ft. Versus Dimensionless frequency (r_o) for a Uniform Pressure Distribution (Poisson's Ratio = 0.3); Comparison of Computed Values. 72

33 Magnitude of Normal Surface Displacement at r = 1 ft. Versus Dimensionless Frequency (r_o) for a Uniform Pressure Distribution (Poisson's Ratio = 0.3); Convergence Study for Superposition. 74

34 Phase Angle of Normal Surface Displacement at r = 1 ft. Versus Dimensionless Frequency (r_o) for a Uniform Pressure Distribution (Poisson's Ratio = 0.3); Convergence Study for Superposition. 75

CHAPTER I

INTRODUCTION

This report describes work funded by two SDHPT projects: 2/3-18-88-1175, "Development of Dynamic Analysis Techniques for Falling-Weight Deflectometer Data," and 2-10-88/8-1215, "Development of Computer Program for Linear Dynamic Analysis of Falling-Weight Deflectometer Data." At the start of the parent 1175 project, the project investigators reviewed existing programs for computing dynamic responses for highway sections. The investigators concluded that it was necessary to develop a fast, efficient computer program designed specifically for pavement dynamics applications. Supplemented funding for developing the program was provided by the 1215 project. This report describes the initial programming effort which was to develop a suitable integration algorithm and apply it to the unlayered case for verification. The same integration technique will be used in the multilayered program to be developed in the second phase of the programming effort sponsored by the 1175 project.

Background

The State of Texas has recently bought and deployed a number of Falling Weight Deflectometers (FWDs) for use in monitoring the structural condition of its highway network. This equipment does an excellent job of applying a simulated moving wheel load to the pavement and measuring the resulting deflections. Most software available to analyze the FWD data is based on static loading conditions such as those measured by the Benklemen beam. These static-based analysis techniques assume the existence of a "deflection basin" under the FWD load. There is evidence, however, that the deflection basin approach does not adequately describe the response of the pavement to a dynamic loading condition such as that imparted by the FWD or a moving wheel load.

The Falling Weight Deflectometer generates a wealth of information about the pavement structure, only a small portion of which is currently used for pavement analysis purposes. Information collected using the FWD has numerous applications in the areas of pavement evaluation, pavement

design, and load rating.

The three principal current uses of the FWD are as listed below:

1. **Structural Index for PES**
   The FWD's were acquired to permit D-18 to incorporate a Structural Index parameter to supplement the visual and ride evaluations in the Network level Pavement Evaluation System.
2. **Load Rating of Thin Pavements**
   D-18 is interested in developing a Non-Destructive Testing procedure for evaluating the current Load Zoning procedures of the Department and for anticipating the consequences of removing load restrictions on thin pavements.
3. **Back Calculating Pavement Layer Moduli for Design Pavements**
   A recent NCHRP Study 10-27, "Determination of Asphaltic Concrete Pavement Structural Properties by Non-Destructive Testing," ranked the FWD as the best device for determining the layer coefficients or moduli for input into the pavement design process.

Potential uses include:

1. More accurate determination of surface layer moduli,
2. Determination of layer thicknesses by data analysis rather than by labor-intensive coring,
3. Development of an improved structural index,
4. Measurement of surface aging,
5. Possible in situ measurement of the creep properties of materials, therefore using the FWD for acceptance testing of in-place mix design.

The FWD nondestructive test data collected for this project includes the complete load impulse and geophone response signals, making available for the first time masses of pavement data that can, if analyzed properly, give useful information on the dynamic response of pavements. This research builds on the extensive past and ongoing work at TTI on pavement technology, design, research, testing, and evaluation (Lytton, Roberts and Stoffels, 1986).

TTI is currently working on several research projects using FWD data.

These are sponsored by the Texas SDHPT, NCHRP, and the FHWA. As a result, considerable data has been acquired on pavement test sections and in-service roads and highways. Transfer functions have been computed for ten pavement test sections in the TTI pavement test facility, and work is being initiated on reducing data from approximately thirty monitored sites throughout Texas. The locations are shown in Figure 1. The monitored sites cover a wide range of pavement thicknesses, base course materials, and subgrade types.

The overall approach or strategy is to extend or build on existing methods of extracting pavement properties from FWD data. Current practice is to use elastic (static) models to extract information on the properties of pavements, e.g., back-calculating elastic moduli for each layer (Uzan, Lytton, and Germann, 1988). Full use is not being made of the data which contains information on the dynamic properties of the pavement layers. The data is affected by elasto-dynamic effects resulting from the pavement's inertia. Elastodynamic effects result in wave behavior whereby the surface disturbances caused by the dropweight propagate outward. This gives rise to a surface wave (Rayleigh wave) and other wave effects.

In addition, the pavement layers have internal damping resulting from viscoelastic effects (Fung, 1965; Pipkin, 1972). In particular, the asphaltic concrete layer exhibits creep or relaxation behavior (Papazian, 1961). The granular base and subbase and the subgrade soil types exhibit damping as well (Das, 1973). Once a frequency-domain elastodynamic model has been developed and implemented, it is relatively simple to include viscoelastic damping effects. This requires development of analytical models of the viscoelastic effects from laboratory test results, as in Papazian (1961). The viscoelastic properties of the pavement materials can in turn be linked analytically to aging, failure, and permanent deformation characteristics.

To illustrate the feasibility of the approach, a procedure for computing damping (i.e., viscoelastic) effects is described as follows: FWD time pulses from TTI Pavement Test Facility Section 9 were transformed using a Fast Fourier Transform (FFT) algorithm. Then, transfer functions (displacement per unit force) were computed at each position on the deflection basin. The transfer functions are complex numbers having a

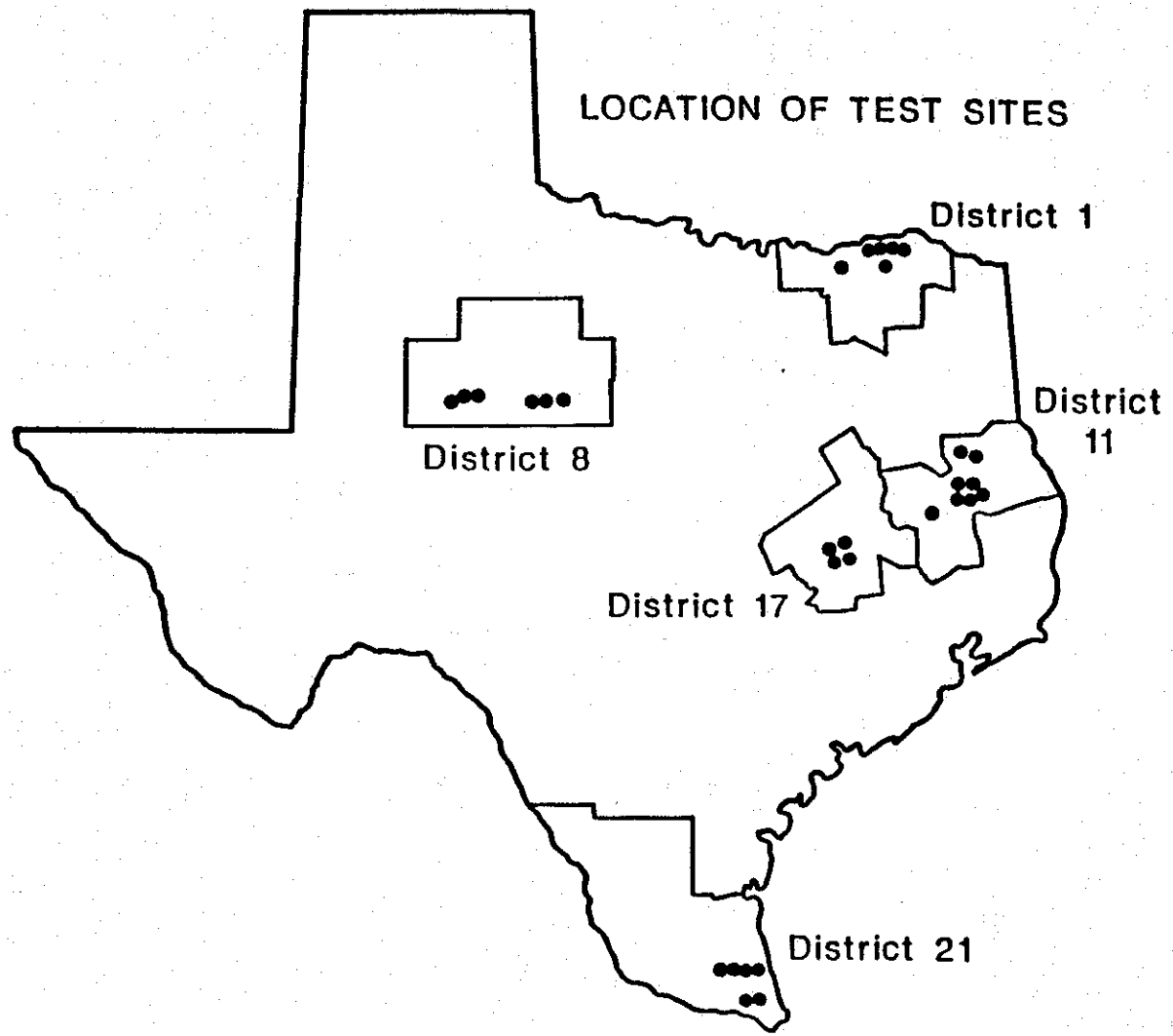

Figure 1. Location of Monitored Highway Sites Selected for Dynamic Analysis Using Falling-Weight Deflectometer Data.

magnitude and phase angle and are functions of the frequency. The transfer functions for r = 0 and r = 6 feet are shown in Figures 2, 3, and 4.

Next, the elastic moduli for each layer are computed from the same data set as the dynamic data. The elastic backcalculation procedure uses only the peaks of the pulses (Uzan, Lytton, and Germann, 1988).

These elastic moduli were used in the UTFWIBM computer program that computes surface displacements for layered media. This program is discussed in Chapter II. The computed results for zero damping are shown in Figures 2, 3, and 4, along with the FWD data. Note that the phase angles do not match very well, although the magnitudes match quite well. The damping was varied in the UTFWIBM program until the phases matched up better. The 14 percent damping curves in the figures are a best fit to the data obtained by iteration.

These results indicate that the elastic backcalculation procedure is only a first approximation to the actual pavement response. Including damping improves the correlation between the predicted or computed values and the FFT transfer function data. This indicates that damping or viscoelastic effects are large enough to detect using FWD data. Later in the project, more realistic damping models will be introduced and the dynamic backcalculation procedure will be formalized or automated by using systems identification techniques.

Objectives of the Study

The objectives of the study are to:

1. Develop an efficient computer model of linear dynamic pavement response tailored for this application by using scalar potentials and numerical integration.
2. Perform computer program checkout, comparison and validation study.

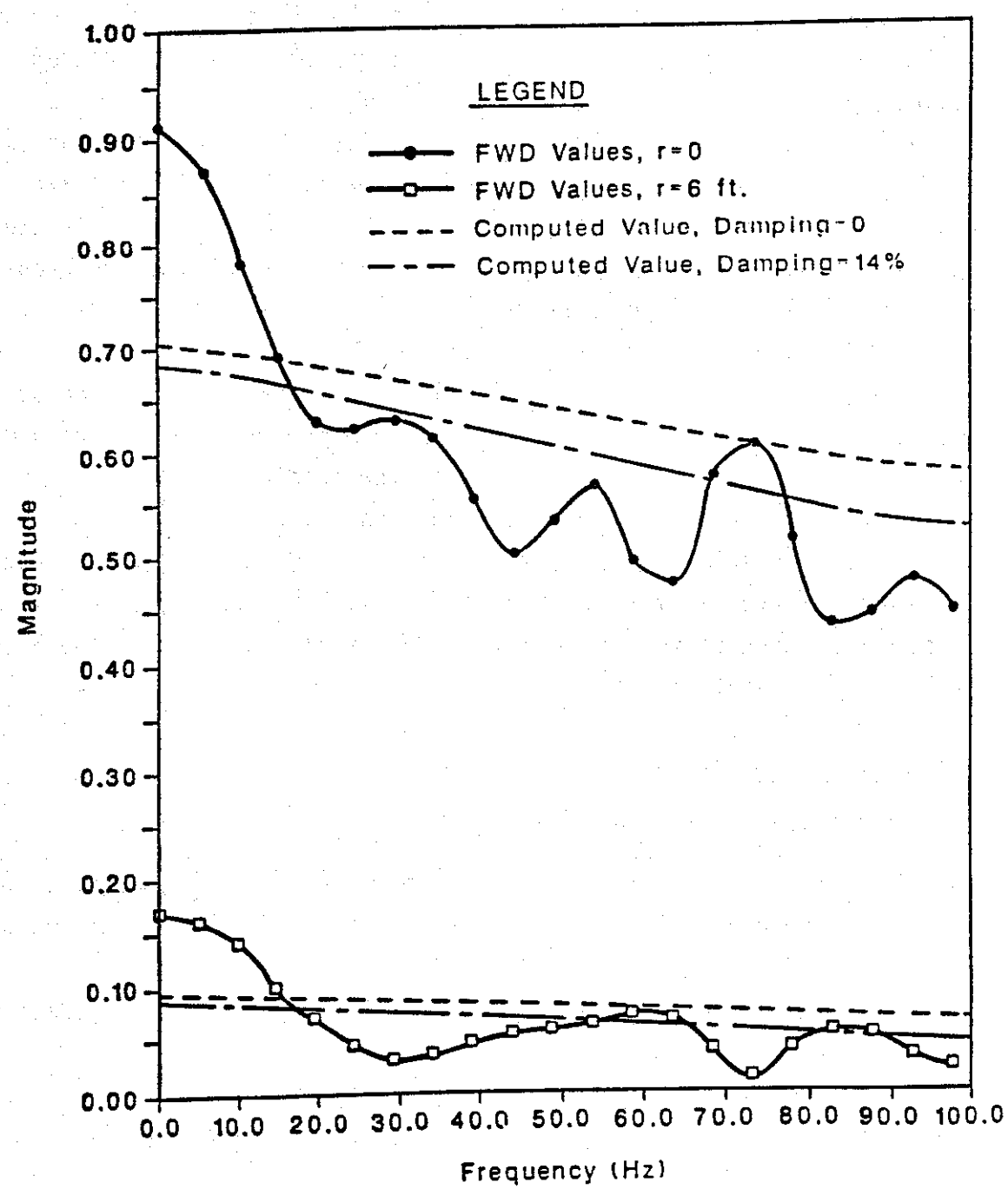

Figure 2. Magnitude of Surface Deflection Versus Frequency for TTI Highway Station 9 for FWD Data and Predicted Values for Two Damping Ratios.

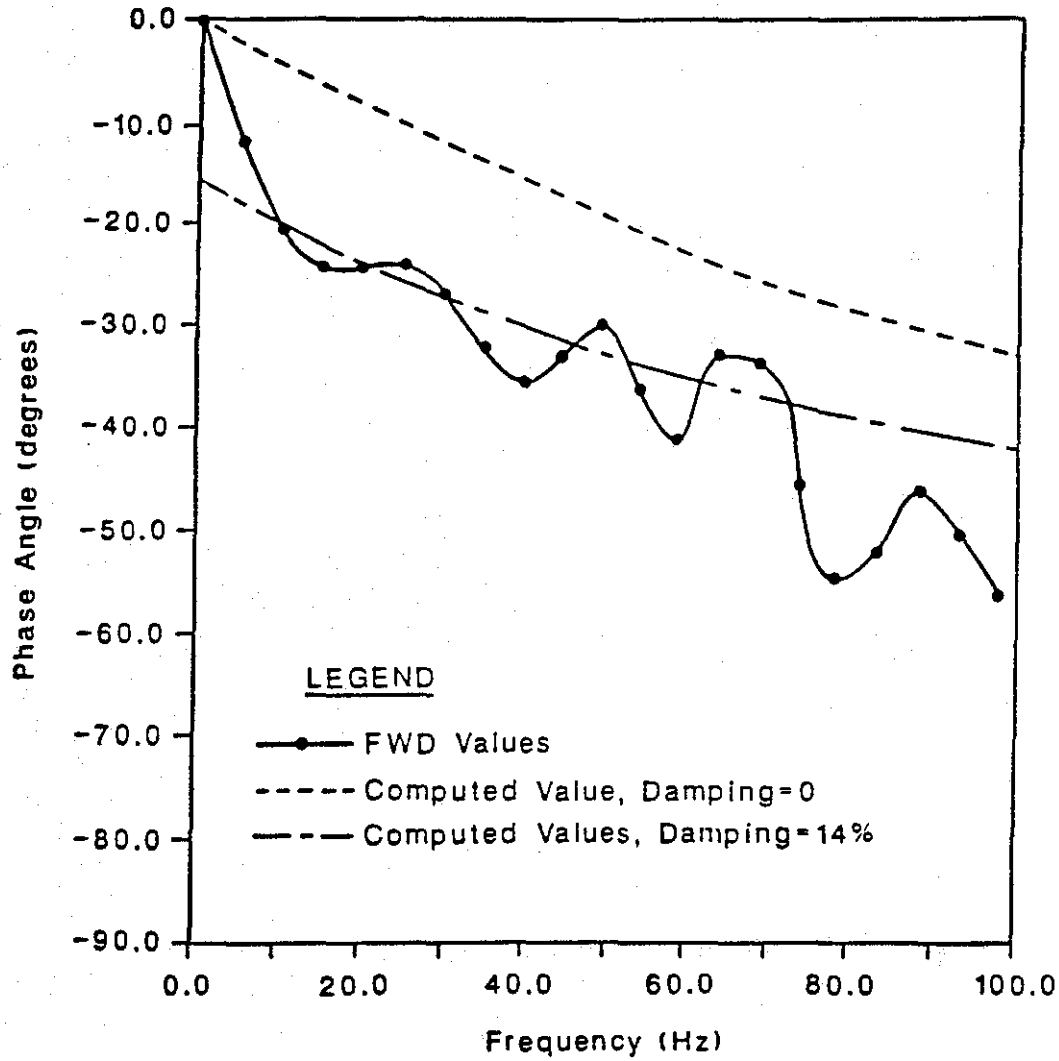

Figure 3. Phase Angle of Surface Deflection Versus Frequency for r = o for TTI Highway Station 9 for FWD Data and Predicted Computed Values.

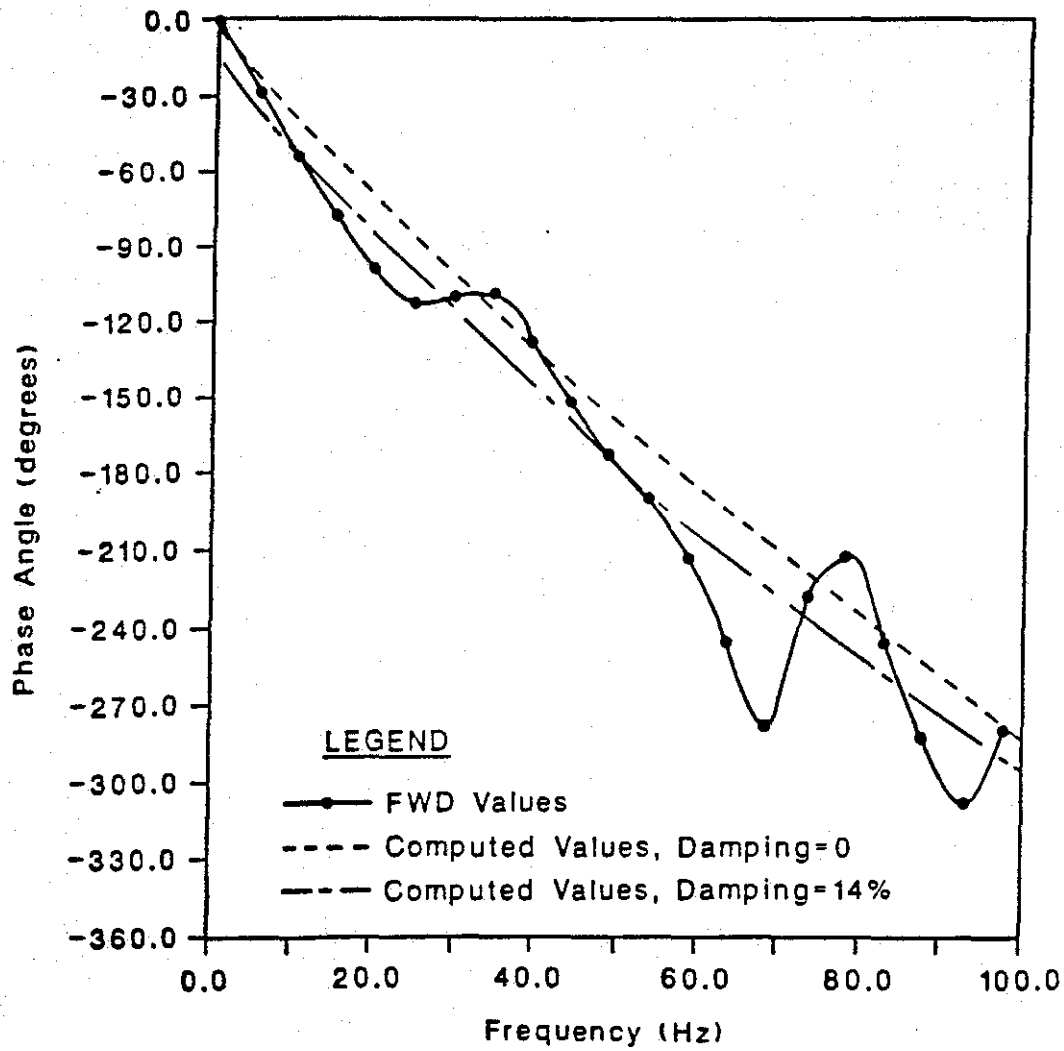

Figure 4. Phase Angle of Surface Deflection Versus Frequency for r = 6 ft. for TTI Highway Section 9 for FWD Data and Computer Predictions.

CHAPTER II

RELATED WORK

In this chapter, the related works of previous investigators will be discussed. This discussion is not intended to be a comprehensive survey or bibliography on the subject. Instead it is meant to introduce various methods of analysis and solutions of closely related problems and to cite representative publications for each approach.

The present study is restricted to analysis of surface deflection caused by a surface disturbance (a force) on a uniform half-space, in particular, the disturbance created by the dropweights of the Dynatest Falling-Weight Deflectometer apparatus. Since this study is the initial phase of the analysis of a multilayered half-space, the literature on layered viscoelastic and elastic media will be discussed as well.

The FWD apparatus measures pavement disturbances in the near-field or in a transition region between the near-field and the far-field or fully-developed wave region. For this reason many of the techniques used for earthquake engineering and seismic studies are not applicable as they are intended for far-field applications. The differences in approach for near-field and far-field studies are mostly in the methods of integration, as will be discussed later.

Analysis of layered media wave problems can be divided into two major parts:

1) Setup of the formal solution in a wavenumber integral form with infinite or semi-infinite limits of integration and

2) Integration of the formal solution to obtain either nonquantitative information on the nature of the solution or quantitative information on specific responses. Various approaches for both of these steps will be discussed below, particularly as they affect the problem under study.

To clarify what is meant by near-field and far-field, it is necessary to define some physical quantities and work out a specific example. Consider a uniform homogeneous isotropic elastic half-space consisting of a nominal plastic clay with physical parameters as follows:

Young's modulus $E = 30$ ksi

Poisson's ratio $\mu = 0.30$

Weight density $\gamma = 120$ lbs/ft^3

Two internal waves are supported by the solid medium: the compressional or longitudinal wave and the shear or transverse wave. For the plastic clay example, the respective wave speeds are:

$$C_L = 1249 \text{ ft/sec}$$

$$C_L = 667.7 \text{ ft/sec}$$

The surface wave or Raleigh wave propagates at a speed slightly slower than the transverse wave. Lamb (1904) showed that the surface wave dominates the response in the far field.

The useful frequency (f) range for transformed data from the Dynatest FWD is from 0 to about 100 Hz. The characteristic wavelength in the half-space is related to the frequency as follows:

$$\lambda_T = C_T/f$$

Therefore, the minimum wavelength corresponding to 100 Hz is

$$\lambda_{min} = 6.7 \text{ ft.}$$

This wavelength is close to the maximum sensor distance of 6 ft. on the FWD apparatus. This indicates that, <u>at most</u>, one cycle of oscillation can occur between the dropweight and the outermost sensor. Far-field measurements are made <u>many</u> wavelengths from the energy source (10, 100, or more wavelengths).

The distinction between far-field and near-field is also determined more precisely by the product of the wavenumber (k) and a characteristic distance. If this product is much larger than one (ten or larger) the problem can be considered to be a far-field one. If it is much smaller than one, the problem is in the near-field and the solution will be quasi-static with no dynamic or wavelike behavior. If the product is around unity, it is in an intermediate region that is neither entirely wavelike nor quasi-static.

For the FWD, the source-receiver distance is a maximum of 6 ft. The maximum product is then, for 100 Hz:

$$(k_T r)_{max} = 2\pi fr/C_T = 5.6$$

For the r = 0 response, the load disk radius a = 0.4925 ft. is used for the characteristic distance, giving:

$$(k_T\ a)_{max} = 2\pi fr/C_T = 0.463$$

These results indicate that the FWD response is in an intermediate range between the quasi-static and the wave zone. For this reason, many of the far-field approaches, such as ray theory, are inapplicable to the present problem, and in fact, no recently developed techniques appear to have been specifically tailored for this intermediate wavenumber range.

Formal solutions to the layered or nonlayered problems can be constructed readily using standard methods of analysis of vector field problems. The formal solution, developed in Chapter III using scalar potential functions, is based on treatments much as Sommerfield (1964a), Landau and Lifschitz (1970), and Fung (1965). The scalar potential solution for axisymmetric vector field problems in a polar cylindrical coordinate system can be traced to Hansen and Beckerley (1937). This approach is used for elastic-dynamic multilayered problems in Ewing, Press, and Jardetzki (1957). See Figure (5) for a sketch of the multilayer geometry.

Most of the formal solutions to the multilayered problem are based on the Thomson (1950), Haskell (1953), and Jardetzki (1953) matrix approach. They used this approach for homogeneous problems (wave dispersion and transmission).

The matrix approach has been applied to a number of homogeneous and inhomogeneous (forced) problems for multilayered media using a plane-strain approximation in each layer or sublayer to construct a three-dimensional solution. This technique was introduced by Biot (1963, 1965). Later Kausel, Roesset and Waas (1974), Kausel and Roesset (1981), Tassoulas and Kausel (1983), and Kausel (1986) used a one-dimensional finite element approach in the direction of stratification to reduce the solution to an algebraic eigenvalue problem (Waas, 1972). This approach has been used in the UTFWIBM program developed at the University of Texas by Professor Roesset and his associates. The UTFWIBM program was used in one of the comparison studies in Chapter VI.

Magnuson (1975) applied the matrix approach and scalar potentials to develop a formal frequency-domain solution to the three-dimensional Navier equation for a layered viscoelastic medium for a forced (inhomogeneous) axisymmetric problem in cylindrical coordinates. Magnuson's result was

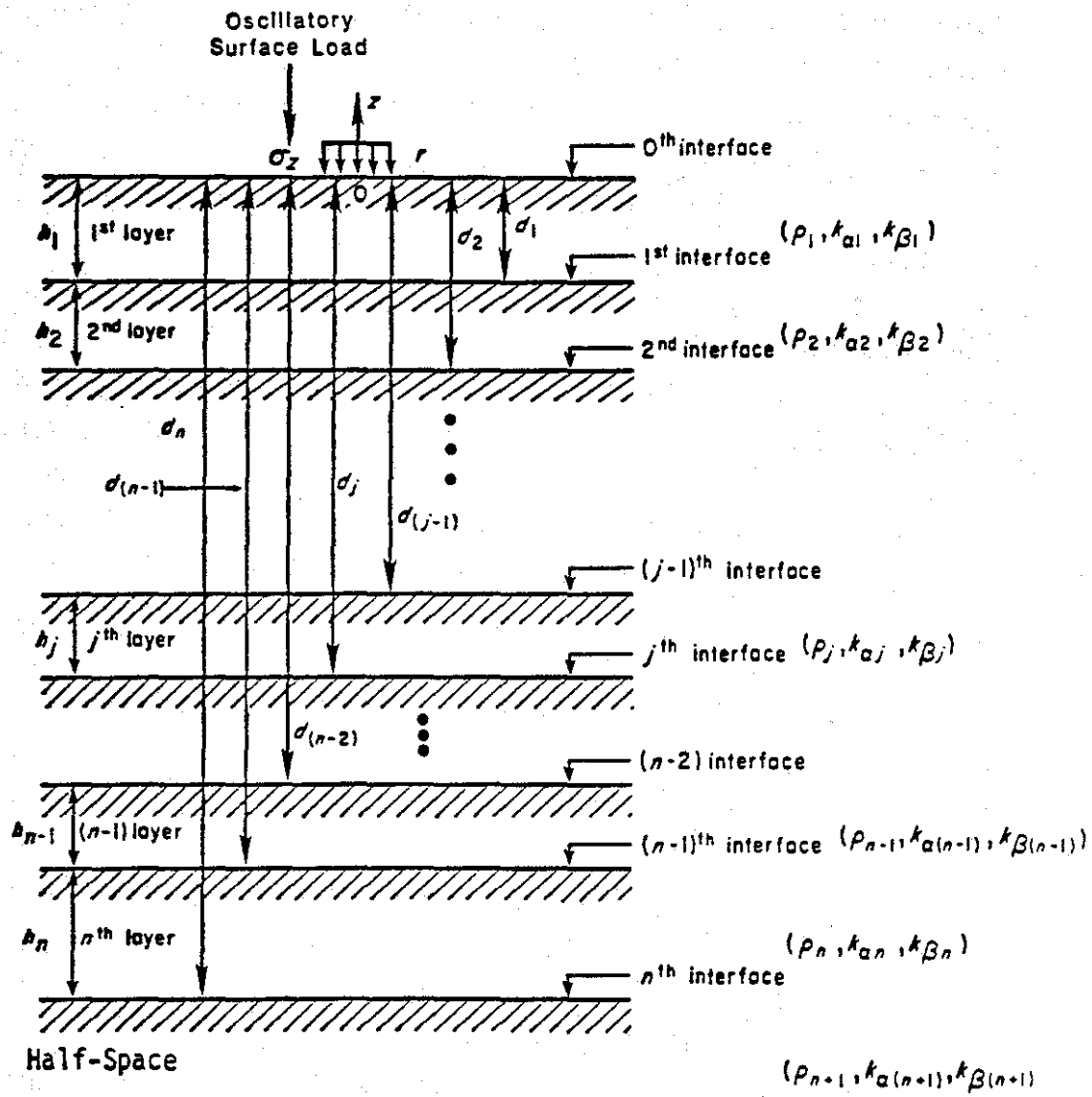

Figure 5. Layered Viscoelastic Half-Space Showing Geometry and Physical Parameters for Each Layer.

presented in the form of a recurrence relation that reduced all computation to 4x4 matrix operations for any number of layers. This approach is to be used for the second phase of this study which will apply the integration algorithm described in the following chapters to the multilayered problem.

All of the solutions using the Thomson-Haskell-Jardetzki matrix approach exploit the banded matrix form for evaluating the unknown wavenumber functions in each layer. The banded form results from application of continuity of displacements and stresses at each layer interface. The banded matrix form is then reduced to a recurrence relation between adjoining layers involving only the unknowns in the two adjoining layers.

Kundu and Mal (1985) indicate that seismologists have essentially abandoned the matrix method in favor of other approximate or iterative schemes that are numerically stable. These methods are described in a book by Kennett (1983). The seismologists' approach is applicable only to far-field work and therefore is not pursued further here.

Numerous methods exist for evaluating the wavenumber integral forms. These can be classed as:

1. Direct numerical integration,
2. Contour integration using complex variables,
3. Approximate methods,
4. Finite elements, and
5. Combinations of the above.

Each technique is discussed as follows:

Numerical Integration: Direct numerical integration is difficult because of the slow convergence of the integrals, especially for cases where the source and receiver are on the surface, and by singularities and the oscillatory nature of the integrand. These complications dictate the choice of integration method for a particular application.

Techniques for numerically integrating oscillatory functions have been developed by Filon (1928), Longman (1956), and most recently, by Zhongjin (1987). The older methods are described in Davis and Rabinowitz (1975). Zhongjin's approach was used in this study.

Contour Integration: Contour integration of the integral forms is

discussed in the books of Ewing, Press, and Jardetzki (1957) and Brekhovskikh (1980). Magnuson (1975a) used the saddle-point method to solve a layered problem with a viscoelastic half-space. The classical complex variable techniques are described in detail in Sommerfeld (1964b) and Brekhovskikh (1980). Most of the complex variable approaches must use far-field approximations or asymptotic expansions to obtain numerical results, so they are inapplicable to the present problem.

Approximate Methods: All of the methods listed above apply approximations at some point. However, this category is used here to classify methods where the basic formulation of the formal solution involves approximations. The work of Biot, Kausel, Roesset, Waas, and Tassoulas referred to above falls into this category because of the use of the plane strain assumption in the formulation. This assumption requires extensive sublayering for the pavement dynamics problem because the subgrade must be suitably subdivided into layers down to a depth where there is no wave penetration. This requires a frequency-dependent grid because the wave penetration is frequency-dependent. The artificial sublayering makes the method inefficient computationally for problems where the number of natural layers is small, i.e. for the pavement dynamics problem.

Finite Elements: Finite element techniques are useful for dynamic analysis of nonlinear pavement behavior, but the technique is expensive and requires large amounts of computer time. Finite element analysis is useful for fundamental investigation of specific phenomena, but simpler, faster techniques must be developed for analyzing large amounts of field data for pavement evaluation.

Hybrid Methods: One hybrid, numerical-complex, variable integration approach has been developed whereby the pole singularity is split off as a separate term and then the remainder of the integrand is integrated numerically as a principal-value integral. Reissner (1936), Sung (1954), and Arnold, Bycroft and Warburton (1955) used this approach to investigate the effect of soil dynamics on machinery vibration. They modeled the soil using a uniform elastic half-space and the machinery as an oscillatory surface pressure distribution. Kundu (1983) and Kundu and Mal (1985) applied the pole removal method to the elastic multilayered solid problem. This approach could be used for the viscoelastic multilayered

problem if a reliable and efficient complex pole-search algorithm was available.

Apsel (1979), Luco and Apsel (1983), and Apsel and Luco (1983) used a modified Filon-type integration with fourth-order polynomials and an adaptive technique to determine subinterval spacing. They also split off the static solution which was evaluated by other methods to improve convergence of the wavenumber integration. This approach was versatile and effective as was demonstrated by their comparison of the results with various published results in both the time and frequency domain.

Dravinski and Mossessian (1988) compared various numerical approaches for evaluating the wavenumber integrals for two-dimensional, inhomogeneous problems. They compared the efficiency of the various integration techniques on the basis of the number of times the wavenumber integrand was evaluated. This criterion has merit especially for multilayered problems because evaluation of the integrand requires time-consuming matrix manipulations. While their results are not directly applicable here, the method of evaluation provides valuable guidance in the development of integration algorithms. That is (other things being equal), the integration scheme that requires the least number of evaluations of the integrand will probably be the most efficient (or fastest) computationally. This was the basis for using a modified version of Zhongjin's (1987) integration approach for this study.

CHAPTER III

DERIVATION OF INTEGRAL EXPRESSION FOR SURFACE DISPLACEMENT

We wish to compute vertical surface displacements for test co simulating those on the Dynatest Falling-Weight Deflectometer. Th load impulse is applied by circular weights after they are dropped impact the pavement surface. The seven displacement sensors are p the center of the weight (the weights have holes in the centers), distances of 1, 2, 3, 4, 5, and 6 ft from the center.

The analysis will be done in the frequency domain using linea theory. Frequency domain analysis corresponds to a steady-state r to a time-harmonic (i.e. sinusoidal) oscillation. The assumption linearity means that the responses are assumed to be proportional magnitude of the applied load. Linearity also implies small defor The geometry of the problem is shown in Figure 6. The surface loa assumed to be uniform in distribution under the load disk which ha radius of 0.4925 ft. The pavement is assumed (for this initial ef be a uniform, homogeneous, isotropic, viscoelastic half-space occu the semi-infinite domain along the negative z-axis. The surface r are at various radial distances "r" from the center of the disk so problem is axisymmetric about the z-axis. That is, there is no va in the azimuthal (θ) direction.

For small deformations, the equation of motion in Cartesian t notation is (Fung, 1965; Landau and Lifschitz, 1970):

$$\rho \frac{\partial^2 u_i}{\partial t^2} = \frac{\partial}{\partial x_i} \sigma_{ij}$$

where: ρ = mass density,

u_j = displacement vector ($j = 1,2,3$),

σ_{ij} = stress tensor,

$\frac{\partial}{\partial t}$ = time derivative, and

$\frac{\partial}{\partial x_i}$ = gradient operator ($i = 1,2,3$).

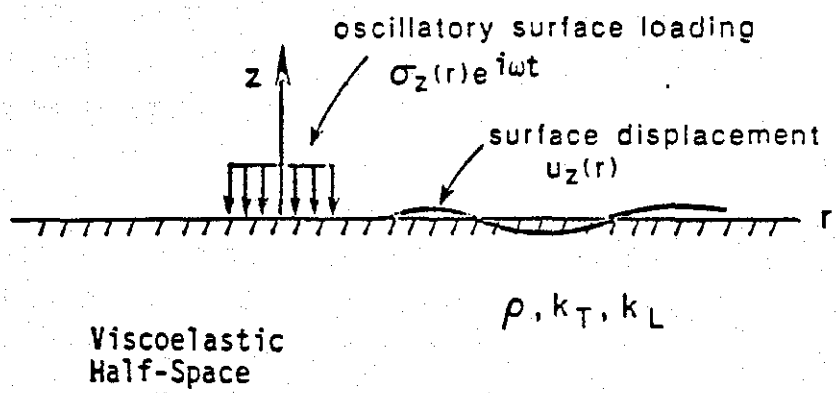

Figure 6. Half-Space Problem with Axial Symmetry.

It is most convenient to work in the frequency domain when dealing with a viscoelastic medium. This is because the superposition integrals in the time domain stress-strain relations reduce to multiplications in the frequency domain so the algebra is similar in form to the elastic solid case (Fung, 1965). To convert to the frequency domain, a Fourier transform pair in time may be introduced as follows:

$$F(\omega) = \int_{-\infty}^{\infty} f(t)e^{-i\omega t}\, dt \tag{2}$$

$$f(t) = \frac{1}{2\pi}\int_{-\infty}^{\infty} F(\omega)e^{i\omega t}\, d\omega, \tag{3}$$

Note from (3) that time differentiation corresponds to multiplication by $i\omega$ in the transform (frequency) domain.

The equation of motion (1) becomes in the frequency domain:

$$\rho\omega^2 u_j + \frac{\partial}{\partial x_i}\sigma_{ij} = 0 \tag{4}$$

where: ω = the radian frequency, and

u_j, σ_{ij} = functions of frequency.

Since the medium has been assumed to be isotropic and homogeneous and undergoing small deformations, Hooke's law may be applied for the stress-strain relationship:

$$\sigma_{ij} = \lambda\epsilon_{\ell\ell}\delta_{ij} + G\epsilon_{ij} \tag{5}$$

where: λ = complex lamé parameter varying with frequency,

G = complex rigidity modulus varying with frequency,

ϵ_{ij} = strain tensor (defined below), and

δ_{ij} = Kronecker delta ($\delta_{ij} = 1$, $i = j$; $\delta_{ij} = 0$, $i \neq j$)

The viscoelastic parameters, λ and G, reduce to constants for the elastic solid. The strain tensor is written in Cartesian form as:

$$\epsilon_{ij} = \tfrac{1}{2}\left(\frac{\partial u_i}{\partial x_j} + \frac{\partial u_j}{\partial x_i}\right) \tag{6}$$

Substituting (6) into (5) and the result into (4) gives the frequency domain Navier equation for the viscoelastic medium:

$$\rho\omega^2\vec{u} - G\,\nabla^2\vec{u} - (\lambda + G)\,\nabla\,(\nabla\cdot\vec{u}) = 0 \qquad (7)$$

where: ∇ = the gradient vector, and

$\vec{u}$ = the vector displacement.

This result (7) is written in vector form because polar cylindrical coordinates are to be used below (Figure 6).

One may introduce complex velocities at this point as follows:

$$C_T^2 = G/\rho \qquad (8a)$$

$$C_L^2 = \frac{(\lambda + 2G)}{\rho} \qquad (8b)$$

where: C_L, C_T = longitudinal wave and transverse wave velocities, respectively.

To simulate viscoelastic effects, a simplified form of damping was introduced. This is constant or frequency-independent damping specified by a damping fraction (usually expressed as a percent). Damping was assumed to be the same for longitudinal and transverse waves. The complex velocities for this type of damping may be written:

$$C_L^2 = C_L^{*2}\,(1 + 2i\zeta) \qquad (8c)$$

$$C_T^2 = C_T^{*2}\,(1 + 2i\zeta) \qquad (8d)$$

where: C_L^*, C_T^* = the respective undamped velocities, and

ζ = damping fraction ($0 \leq \zeta \leq 1$).

This type of damping (8c, 8d) represents the effect of dry (coulomb) friction in cyclic loading of a granular material. The damping represents the equivalent linear energy loss caused by traversing a hysteresis loop resulting from the nonlinear behavior of the material (Das, 1983). This damping model is being used as an interim measure until a more physically realistic model is developed. The final viscoelastic model will characterize relaxation and/or creep, and it will differentiate between compressional (bulk) and shear damping.

Complex wave numbers corresponding to the respective velocities are usually introduced for convenience as follows:

$$k_T = \omega/C_T \tag{9a}$$

$$k_L = \omega/C_L \tag{9b}$$

Expressions (8) and (9) may be applied to Navier's equation (7) to obtain a more compact form:

$$(\nabla^2 + k_T^2)\vec{u} - (1 - \frac{k_T^2}{k_L^2}) \nabla\nabla.\vec{u} = 0 \tag{10}$$

The vector displacement field may be decomposed into longitudinal and transverse components by using Helmholtz' vector decomposition theorem:

$$\vec{u} = \vec{u}_L + \vec{u}_T \tag{11}$$

where:

$$\nabla \cdot \vec{u}_T = 0$$

$$\nabla \times \vec{u}_L = 0$$

The vector field equation (10) may be simplified to two scalar equations by introducing scalar potential functions following Hansen and Beckerley (1937). Each component in (11) is expressed as follows:

$$\vec{u}_L = \text{grad } \phi \tag{12a}$$

$$(\vec{u}_T)_{HS} = \nabla \times \vec{A} \tag{12b}$$

$$(\vec{u}_T)_{VS} = \nabla \times \nabla \times \vec{A} \tag{12c}$$

where each expression above represents a separate polarization. There are two transverse polarizations, the horizontal shear (HS) and the vertical shear (VS). Equation (12) introduced two potentials, ϕ, a scalar Potential associated with the compressional wave, and $\vec{A}$, a vector potential satisfying $\nabla \cdot \vec{A} = 0$. The form of the vector potential is dependent on the coordinate system. For the cylindrical polar coordinate system appropriate to this problem, the following expression for the vector potential is used (see Hansen and Beckerley, 1937):

$$\vec{A} = \vec{\epsilon}_z \psi \tag{13}$$

where: $\vec{e}_z$ = the unit vector in the z-direction, and

ψ = a scalar potential associated with the transverse wave.

Because the surface excitation is vertical and axisymmetric, only the longitudinal and VS (vertical shear) polarizations are excited. The HS or horizontal shear polarization must be excited by an axisymmetric surface torque.

Applying Equations (11), (12), and (13) to the vector field equation (1) gives the two separate scalar Helmholtz equations in the two scalar potentials:

$$(\nabla^2 + k_L)^2 \phi = 0 \tag{14a}$$

$$(\nabla^2 + k_T)^2 \psi = 0 \tag{14b}$$

The decomposition of the field into polarizations was introduced because it results in two scalar equations (14a and 14b) which are easier to solve than the vector field equations (10).

Now using Equations (11), (12), and (13), the displacements, strains, and stresses can be written in cylindrical, polar coordinates using the scalar potentials as:

$$u_r = \frac{\partial(\phi + \partial\psi/\partial z)}{\partial r} \tag{15a}$$

$$u_z = \frac{\partial \phi}{\partial z} + \left[\frac{\partial^2}{\partial z^2} + k_T^2\right] \psi \tag{15b}$$

$$u_{\theta z} = 0 \tag{15c}$$

The only nonzero elements of the strain and stress field of interest are those acting on the horizontal surfaces of the layers, i.e., ϵ_{zz}, ϵ_{rz}, σ_{zz}, σ_{rz}.

The strains are:

$$\epsilon_{zz} = \frac{\partial u_z}{\partial z} \tag{16a}$$

$$2\epsilon_{rz} = \frac{\partial u_r}{\partial z} + \frac{\partial u_z}{\partial r} \tag{15b}$$

$$\epsilon_{\theta z} = 0 \tag{15c}$$

The stresses are, on applying Hooke's law (5):

$$\sigma_{zz} = \left(-\lambda k_L^2 + 2\frac{\partial^2}{\partial z^2}\right)\phi + 2\frac{\partial}{\partial z}\left[\left(k_T^2 + \frac{\partial^2}{\partial z^2}\right)\psi\right] \tag{17a}$$

$$\sigma_{rz} = \frac{\partial}{\partial r}\left[2\frac{\partial \phi}{\partial z} + \left(k_T^2 + 2\frac{\partial}{\partial z^2}\right)\psi\right] \tag{17b}$$

$$\sigma_{\theta z} = 0 \tag{17c}$$

One must now find solutions to the Helmholtz equations (14) suitable to the cylindrical coordinate system and the axisymmetric nature of the problem. This is done by using separation of variables and by taking an appropriate integral transform solution that represents a continuous distribution (spectrum) of eigenfunctions, following Sommerfeld (1964b). Introducing a Fourier-Bessel transform, the potentials may be written in the forms:

$$\phi_L(r,z) = \int_0^\infty J_0(kr)\,\bar{\phi}(k,z)\,k\,dk \tag{18a}$$

$$\psi_T(r,z) = \int_0^\infty J_0(kr)\,\bar{\psi}(k,z)\,k\,dk \tag{18b}$$

where: $\bar{\phi}$, $\bar{\psi}$ J are the transformed potentials, and

J_0 = the zeroth order Bessel Function.

To satisfy the Helmholtz equations (14), one writes the expressions for $\bar{\phi}$ and $\bar{\psi}$ as follows:

$$\bar{\phi} = A(k)e^{\nu z} \tag{19a}$$

$$\bar{\psi} = B(k)e^{-\nu' z} \tag{19b}$$

where: $\nu = (k^2 - k_L^2)^{\frac{1}{2}}$ and

$\nu' = (k \stackrel{?}{=} k)_T^{2\ \frac{1}{2}}$

Here, the square root for ν and ν' is taken so that the real part is

positive. This is to ensure convergence of the integrals (18) for negative z (in the half-space interior).

Now, the spectral or wavenumber-dependent factors A(k) and B(k) in (19) must be evaluated from the boundary conditions for the problem. Since the boundary conditions on the surface involve stresses, transformed expressions for them are needed. Substituting the transformed expressions for the potential (18a, 18b) using (19a, 19b) into the expressions for the stresses (17) gives:

$$\sigma_{rz} = G \int_0^\infty \left[2\nu A(k) e^{\nu z} + (2k^2 - k_T^2)\, B(k) e^{\nu' z} \right] \frac{d}{dr} [J_0(kr)]\, k\, dk \qquad (20a)$$

$$\sigma_{zz} = G \int_0^\infty \left[(2k^2 - k_T^2) A(k) e^{\nu z} + 2\nu' k^2 B(k) e^{\nu' z} \right] J_0(kr) k\, dk \qquad (20b)$$

The boundary conditions on the surface are that the normal stress is specified by the FWD load and the shear stress is zero, or:

$$\sigma_{zz}\Big|_{z=0} = \sigma_0(r) = \int_0^\infty \underline{\sigma}_0(k)\, J_0(kr)\, kdk \qquad (21a)$$

$$\sigma_{rz}\Big|_{z=0} = 0 \qquad (21b)$$

where: $\underline{\sigma}_0(k)$ = the transformed normal stress distribution given as the Fourier-Bessel transform:

$$\underline{\sigma}_0(k) = \int_0^\infty \sigma_0(r) J_0(kr)\, rdr \qquad (22)$$

Two pressure distributions are of interest at present. These are the uniform distribution and the point (delta function) distribution. The uniform distribution is written:

$$\sigma_0(r) = \begin{cases} \sigma_0 & r \le a \\ 0 & r > a \end{cases} \qquad (23)$$

where: a = the radius of the load disk.

From (22) the transformed form of the uniform load is:

$$\sigma_0(k) = \frac{P}{\pi a k} J_1(ka) \qquad (24)$$

where the load $P = \sigma_0 \pi a^2$.

The point load distribution is:

$$\sigma_o(r) = \frac{P\delta(r)}{(2\pi r)} \tag{25}$$

where $\delta(r)$ is the Dirac delta function. The transformed form of (25) is:

$$\underline{\sigma}_o(k) = \frac{P}{2\pi} \tag{25a}$$

Applying (21a) and (21b) to (20c) and (20d) gives for the unknown functions A and B:

$$A(k) = \frac{(2k^2 - k_T^2)\ \underline{\sigma}_o(k)}{G\ F(k)} \tag{26a}$$

$$B(k) = \frac{-2\nu \underline{\sigma}_o(k)}{G\ F(k)} \tag{26b}$$

where:

$$F(k) = (2k^2 - k_T^2)^2 - 4\nu\nu' k^2 \tag{26c}$$

We wish to solve for the surface displacements, which can be expressed in integral form by using (18) and (19) in (15), giving:

$$u_r = \int_0^\infty \left[A(k)e^{\nu z} + \nu' B(k)e^{\nu' z}) \right] \frac{d}{dr}\left[J_o(kr)\right] kdk \tag{27a}$$

$$u_z = \int_0^\infty \left[\nu A(k)e^{\nu z} + k^2 B(k)e^{\nu' z}\right] \left[J_o(kr)\right] kdk \tag{27b}$$

The vertical (u_z) response is required for FWD analysis, so the results (26) are applied to (27b) giving:

$$u_z = \frac{-Pk_T^2}{\pi Ga} \int_0^\infty \frac{\nu J_0(kr)J_1(ka)}{F(k)}\, dk \tag{28}$$

This relatively inocuous looking expression is extremely difficult to evaluate accurately for a number of reasons which will be discussed in the next chapter. The result (28) is consistent with the uniform pressure distribution result in Arnold, Bycroft, and Warburton (1955) and Sung (1953).

The double oscillation of the integrand in (28) resulting from the two Bessel functions, J_o and J_1, causes problems in integration. Single

oscillations can be treated using existing methods described in the literature. (See the next chapter.) The FWD response problem was solved in two parts to avoid the numerical problems associated with the double oscillation.

The response at r = 0 for the uniform load, is a special case of the result (28) because the J_o Bessel function disappears ($J_o(0) = 1$), leaving the following simplified expression:

Uniform load, r = 0

$$u_z = \frac{-Pk_1^2}{\pi Ga} \int_0^\infty \frac{\nu\, J_1(ka)}{F(k)}\, dk \tag{29}$$

To compute u_z for general r outside the load disk (r > a) for the uniform distribution one may use superposition of the point load response. Applying the point load expression (25a) to (26 and 27b) gives:

Point Load Response

$$g(\omega, r) = \frac{Pk_1^2}{2\pi G} \int_0^\infty \frac{\nu J_o(kr)kdk}{F(k)} \tag{30}$$

Here the vertical displacement is denoted as a frequency domain Green's function $g(\omega,r)$, varying only with the frequency and the distance (r) between the surface disturbance and surface field point.

The superposition integral is a two-dimensional (surface) convolution integral written most conveniently in a Cartesian system as follows:

$$u_z(x,y) = \iint_A g(\omega, x-x', y-y')\sigma_z(x',y')dx'dy' \tag{31}$$

where $g(\omega,x-x',y-y')$ is the Green's function after being shifted and folded over; $\sigma_z(x', y')$ is the pressure distribution over the area A; x', y' are the dummy coordinates of the area A; and x, y are the field point coordinates. The geometry is shown in Figure 7. In polar (r,θ) coordinates, the superposition integral becomes:

$$u_z(r,\theta) = \iint_A g(\omega, r-r', \theta-\theta')\sigma_z(r',\theta)\, r'dr'd\theta' \tag{31a}$$

For the axisymmetric problem, the θ - dependence in the field point is suppressed, giving for (31a):

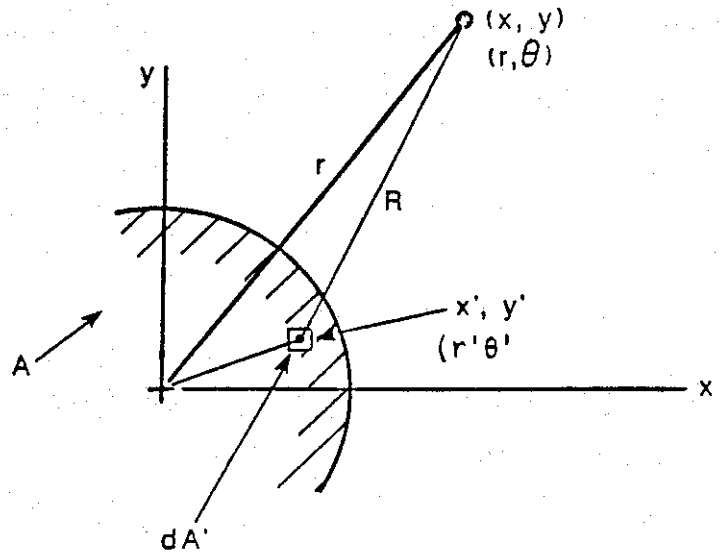

a) General

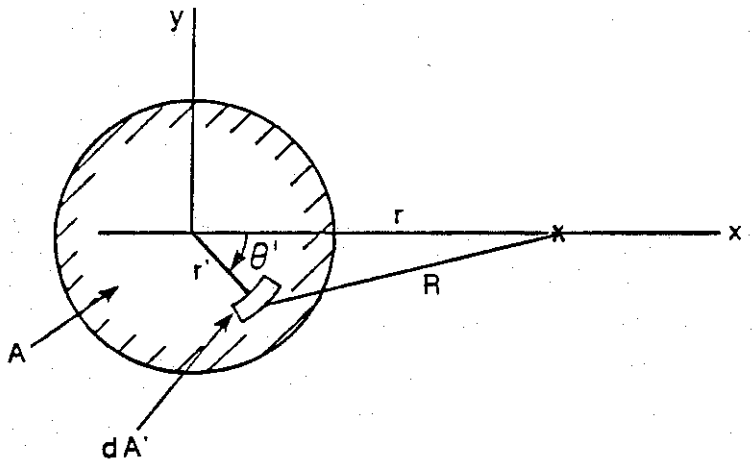

b) Axisymmetric

Figure 7. Superposition Integral Geometry.

$$u_z(r) = \iint_A g(\omega,R)\sigma_z(r')r'\,dr'\,d\theta' \tag{31b}$$

where:

$$R = R(r,r',\theta') = (r'^2+r^2-2r'r\cos\theta')^{\frac{1}{2}}$$

For a uniform circular pressure distribution of radius a, (31b) further simplifies to:

$$u_z(r) = P/A\int_0^{2\pi} d\theta' \int_0^a g(\omega,R)r'\,dr'\,d\theta' \tag{31c}$$

where $P = \sigma_z A$.

The superposition integral (31c) was approximated or discretized by assuming that Green's function was constant over each area element and by summing as follows:

$$u_z(r) \cong P/A \sum_{j=1}^{N} \Delta A_j\ g(\omega,R_j) \tag{31d}$$

where:

$$R_j = (\bar{r}_j^2 + r^2 - 2\bar{r}_j r\cos(\bar{\theta}_j))^{\frac{1}{2}}$$

and $\bar{r}_j$ = mean radius of jth element
$\bar{\theta}_j$ = mean angle of jth element
ΔA_j = area of jth element.

The results of the comparison studies in Chapter VI are presented in dimensionless form. Reissner's (1936) dimensionless form is used for the r = 0 responses, while a similar form used by Luco and Apsel (1983) is used for the Green's function comparison and the uniform load results for arbitrary r.

Reissner's dimensionless displacement is represented as a complex function $f = f_1+if_2$, which varies with dimensionless frequency a_0, both being defined as follows:

$$f = f_1+if_2 = G^*a\,u_z/P \tag{32}$$
$$a_0 = \omega a/C_T^*$$

where G* and C_T* are the elastic (zero damping) rigidity and shear wave speed, respectively. The two are related as follows:

$$C_T^{*2} = G^*/\rho$$

The complex function f can be represented in magnitude and phase form as follows:

$$f = |f|\, e^{i\phi_f} \tag{32a}$$

where:

$$|f| = (f_1^2 + f_2^2)^{\frac{1}{2}}$$

and

$$\phi_f = \tan^{-1}(f_2/f_1)$$

Solving for u_z in (32) gives:

$$u_z = \frac{P}{G^* a}\,(f_1 + if_2) \tag{32c}$$

For an elastic solid, f is dependent only on a_0 and Poisson's ratio. Therefore the displacement form (32c) is proportional to the force P and inversely proportional to the material stiffness G^*. The dimensionless frequency a_0 is seen from (32) to be inversely proportional to the square root of the stiffness.

The nondimensional representation used by Luco and Apsel (1983) for their Green's function computations is similar to Reissner's (36), except the field distance r was used for a length reference scale instead of the disk radius a. Their dimensionless displacement and dimensionless frequency are respectively:

$$f_r = G^* r\, u_z/P \tag{33}$$

$$r_0 = \omega r/C_T^*$$

where $f_r = f_{r1} + if_{r2}$.

CHAPTER IV

METHOD OF INTEGRATION

Ideally, the expression for the surface displacement resulting from the uniform load, Equation (28) of Chapter III should be evaluated directly. Unfortunately, this is not possible to do at present with any control over accuracy because of the slow convergence and the double oscillation of the integral resulting from the two Bessel functions J_o and J_1. However, methods have been developed for numerically integrating slowly convergent expressions with single oscillations of the integrand (see Davis and Rabinowitz (1975) and Zhongjin (1987)). Therefore, the integration must be simplified by breaking it into two separate cases. The r = 0 response to a uniform load is computed from a special case of the general integral, Equation (29). For general r (r>a) the response is computed by superimposing Green's functions (point load responses) using the superposition integral (31c), or its discretized version (31d). The Green's function is given in integral form in (30). Therefore, two integrations must be performed to compute responses for the FWD. These are rewritten as follows from (29) and (30) after suppressing the constant factor outside the integral:

$$I_u = \int_0^\infty \frac{\nu}{F(k)} J_1(ka)dk \qquad (34a)$$

$$I_p = \int_0^\infty \frac{\nu k}{F(k)} J_o(kr)dk \qquad (34b)$$

where: I_u = the integral for uniform loading, and r = 0,

I_p = the point load response at a distance r from the disturbance, and

$F(k)$ = Rayleigh's denominator given in (26c).

Notice that these integrals are similar in appearance, the main difference being the different order of the Bessel function. The J_o and J_1 Bessel functions are plotted in Figure 8 showing their oscillatory nature.

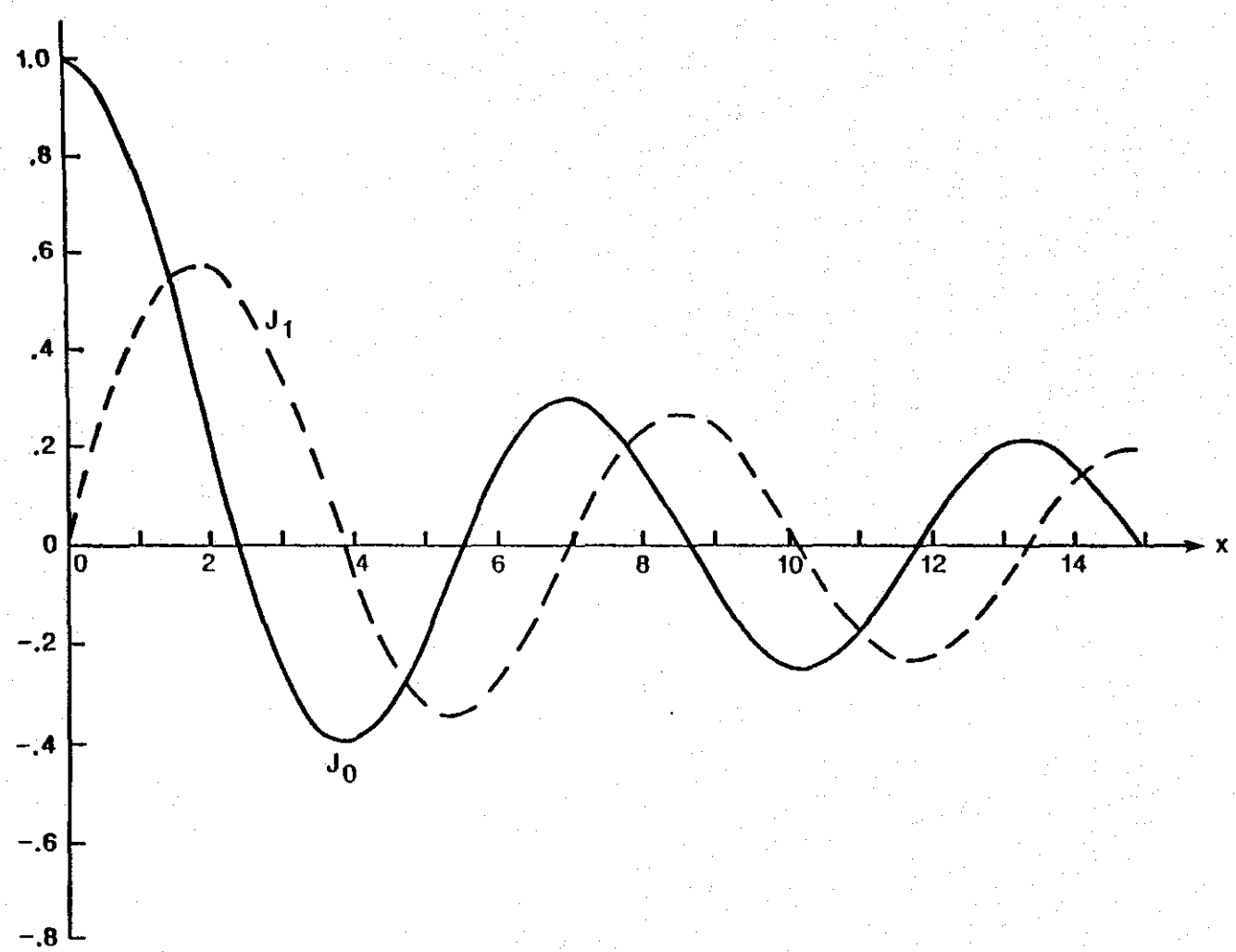

Figure 8. Bessel Functions of Order Zero and One ($J_o(x)$, $J_1(x)$).

For this reason, only the integration strategy for I_p (34b) will be described in detail. The other integration used the same approach or strategy with minor differences in algebra.

Integration of the improper integrals (34a and 34b) is particularly difficult because of their slow convergence with respect to the upper limit. The slow convergence is a consequence of the lack of any exponential attenuation in the integrand that occurs when the disturbance and source occur at different depths. The infinite upper limit must be approximated by a finite number: that is, the integral must be truncated. Because of the nature of the integrand, the convergence is very slow, meaning that the upper limit must be taken as very large to obtain adequate accuracy. The convergence is further complicated by the oscillatory nature of the integrand: the scatter in the truncated answer results from where on the oscillation cycle the truncation occurs. This is illustrated in Table 1 where the zero-order Bessel function $J_o(x)$ was integrated for a range of upper limits as follows:

$$I(y) = \int_0^y J_o(x)dx \qquad (35)$$

In the limit as y approaches infinity, the value of the integral in (35) approaches one (1.0). In Table 1, the upper limit y was varied from 500 to 5,000. The integrated values were obtained using the trapezoidal rule with about 100 ordinates per cycle of the Bessel function. The results show that the error varies between plus or minus one percent or more, with very little improvement as y increases.

The scatter seen in Table 1 can be removed by truncating at the end of each cycle of oscillation of the Bessel function. When this is done, the result is always low (less than 1.0 in this case), as shown in Table 2 where the computer program JINT.C was used to evaluate (35) at every other zero-crossing of the J_o integrand. The number (N) of cycles of the Bessel function at truncation is shown in column 1. Column 2 shows the value of the argument of the integrand at truncation (y), column 3 shows the incremental area over the preceding cycle, and column 4 shows the truncated integral I(y). The rate of convergence is given by the third column. This is seen to be very small: 4.6×10^{-4} at N = 50. The convergence is indicated in the fourth column; at N = 50 cycles the answer

Table 1.

Convergence of Integral of Bessel Function

Upper Limit y	Approximate Integral I(y)
500	1.010531
1,000	1.004699
1,500	0.987145
2,000	1.016352
2,500	0.984103
3,000	1.012299
3,500	0.993306
4,000	1.000415
4,500	1.005209
5,000	0.990891

Table 2. Numerical Integration of J_0 Bessel Function Based on Zero Crossings.

Number of Cycles	Integrand Argument at Truncation	Incremental Area	Truncated Integral	Estimated Integral
1	5.52	0.668846	0.668846	1.00913337
2	11.79	0.100273	0.769119	1.00157935
3	18.07	0.043713	0.812831	1.00056016
4	24.35	0.025736	0.838567	1.00026867
5	30.63	0.017419	0.855986	1.00015215
6	36.92	0.012785	0.868771	1.00009569
7	43.20	0.009895	0.878666	1.00006470
8	49.48	0.007951	0.886617	1.00004611
9	55.77	0.006569	0.893186	1.00003421
10	62.05	0.005546	0.898733	1.00002620
11	68.33	0.004764	0.903497	1.00002059
12	74.61	0.004149	0.907646	1.00001652
13	80.90	0.003657	0.911303	1.00001349
14	87.18	0.003254	0.914557	1.00001118
15	93.46	0.002921	0.917478	1.00000939
16	99.75	0.002640	0.920118	1.00000797
17	106.03	0.002402	0.922520	1.00000684
18	112.31	0.002198	0.924718	1.00000592
19	118.60	0.002021	0.926738	1.00000516
20	124.88	0.001866	0.928605	1.00000453
21	131.16	0.001731	0.930335	1.00000400
22	137.45	0.001611	0.931946	1.00000355
23	143.73	0.001504	0.933450	1.00000317
24	150.01	0.001408	0.934858	1.00000285
25	156.30	0.001323	0.936181	1.00000256
26	162.58	0.001245	0.937426	1.00000232
27	168.86	0.001175	0.938601	1.00000210
28	175.14	0.001111	0.939712	1.00000192
29	181.43	0.001053	0.940765	1.00000175
30	187.71	0.001000	0.941765	1.00000160
31	193.99	0.000951	0.942716	1.00000147
32	200.28	0.000906	0.943621	1.00000136
33	206.56	0.000864	0.944485	1.00000125
34	212.84	0.000825	0.945311	1.00000116
35	219.13	0.000790	0.946101	1.00000107
36	225.41	0.000756	0.946857	1.00000100
37	231.69	0.000725	0.947582	1.00000093
38	237.98	0.000697	0.948279	1.00000086
39	244.26	0.000670	0.948949	1.00000081
40	250.54	0.000644	0.949593	1.00000075
41	256.83	0.000620	0.950213	1.00000071
42	263.11	0.000598	0.950811	1.00000066
43	269.39	0.000577	0.951388	1.00000062
44	275.68	0.000557	0.951945	1.00000058
45	281.96	0.000538	0.952484	1.00000055
46	288.24	0.000521	0.953004	1.00000052
47	294.52	0.000504	0.953508	1.00000049
48	300.81	0.000488	0.953996	1.00000046
49	307.09	0.000473	0.954469	1.00000043
50	313.37	0.000459	0.954928	1.00000041

is low by about 4.5 percent. The last column shows the computed value of the integral including the truncation error estimation to be described later in this chapter.

Integrating (34a and 34b) is further complicated by the presence of pole and branch point singularities in the nonoscillatory or frequency-dependent part of the integrand; i.e. the $\nu/F(k)$ factor. The integrand has a simple complex pole singularity associated with the Rayleigh wave. The pole corresponds to the zero of the Rayleigh demoninator:

$$F(k) = (2k_T^2-k^2)^2 - 4\nu\nu' k^2 = 0 \qquad (36)$$

The pole produces a peak or spike in the integrand, the severity varying inversely with the damping. This is because the complex pole approaches the real axis (along which the integration is being performed) as the damping is reduced. In the elastic case, the pole lies on the real axis causing a singularity and the integral must be evaluated by splitting off the pole singularity as a half-residue term, and then performing a principal value evaluation of the remainder of the integral (Reissner [1936], Sung [1953] and Arnold, et al. [1954]).

The square root factors ν and ν' have branch points at $k=k_L$ and $k=k_T$ which result in discontinuities in the integrand in the absence of damping. As damping is introduced, the discontinuities become "rounded off."

A three-dimensional plot of the nonoscillatory part of the integrand as a function of dimensionless wavenumber and frequency is shown in Figure 9 taken from Apsel and Luco (1983). The top plot shows the damped Rayleigh wave singularity and the branch point discontinuity for the uniform half-space. Also shown are plots for two- and three-layered strata showing frequency-dependent multiple singularities due to the layering. These peaks represent damped normal modes.

Integration of improper integrals with oscillatory integrands is discussed in Davis and Rabinowitz (1975). They discribe evaluation of slowly convergent integrals with oscillatory integrands using an Euler expansion which exploits the convergence preperties of an alternating series. Davis and Rabinowitz cite Longman (1956) who applied Euler's method to an integral similar to (34), except that his example had exponential convergence in the integrand, which is much more rapidly

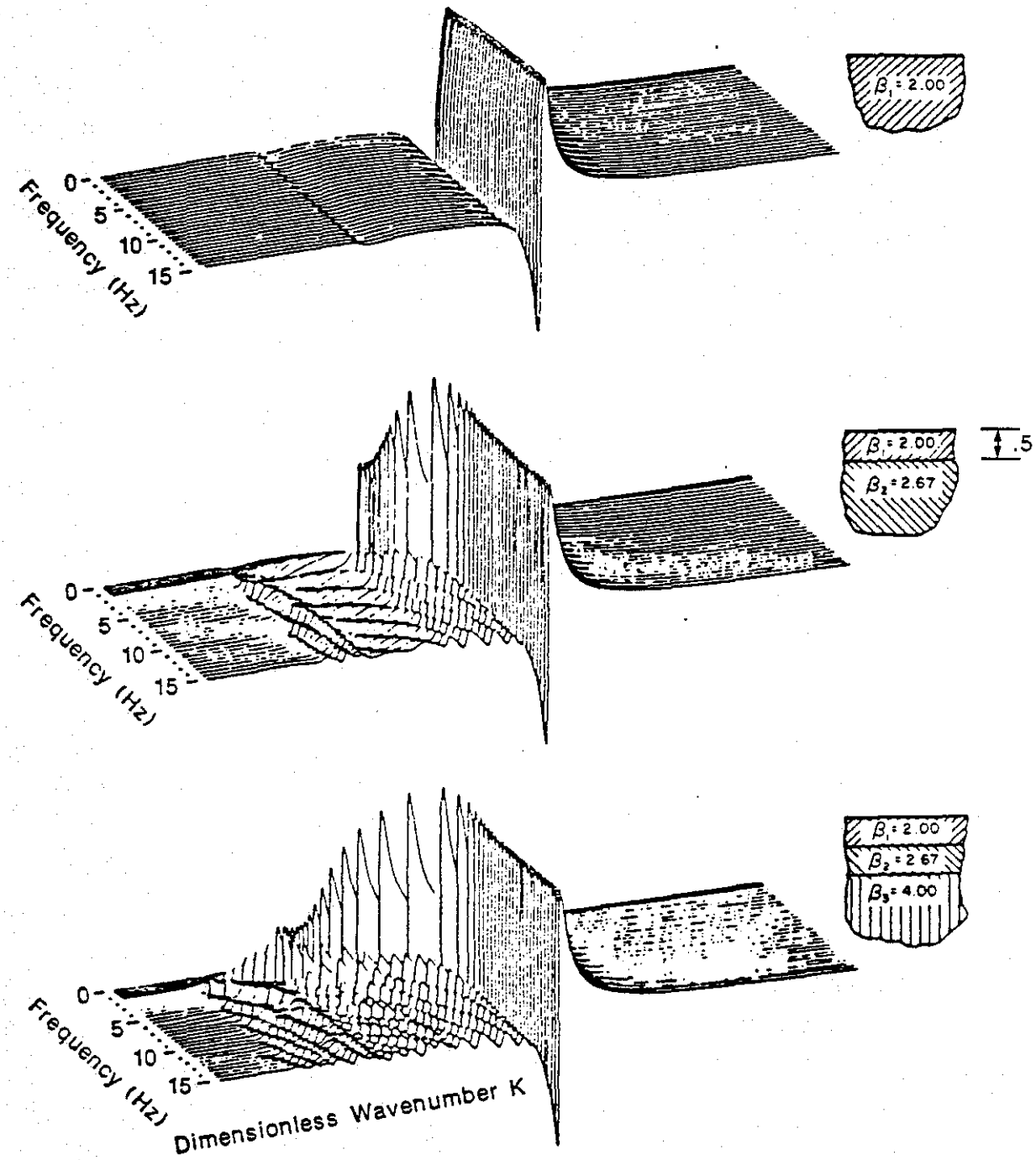

Figure 9. Non-Oscillatory Part of Integrand as a Function of Frequency and Wavenumber for the Uniform Half-Space and for Two-Layer and Three-Layer Half-Space.

convergent than (34a and b or 35).

A more recent approach was presented by Zhongjin (1987) who developed a very simple method of computing an upper bound to the truncation error. This approach was adopted and modified in this study to produce an accurate estimate of the error due to truncation. The integration strategy is described below.

The integral (34b) was broken into three terms as follows:

$$I_p = I_{p1} + I_{p2} + \text{error term} \tag{37}$$

where:

$$I_{p1} = \int_0^{k_1} \frac{\nu k}{F(k)} J_o(kr)dk$$

$$I_{p2} = \int_{k1}^{k_N} \frac{\nu k}{F(k)} J_o(kr)dk$$

$$\text{error term} \quad \approx \quad \int_{k_N}^{\infty} \frac{\nu k}{F(k)} J_o(kr)dk$$

The first term integrates over the Rayleigh wave pole and the branch singularities. The upper limit k_1 is given as:

$$k_1 = c_1 k_T^* \tag{38}$$

where c_1 is a constant (usually varying from 3 to 5), and k_T^* is the undamped shear wavenumber. This upper limit is used so that the I_1 term encompasses the pole and branch singularities and extends out far enough that the nonoscillatory integrand "settles down" to an hyperbolic shape. The I_I term integrates over the damped Rayleigh wave pole and branch point shown in Figure 9. Simpson's (1-4-1) rule was used for the integral. The spacing of the I_1 subintervals was determined as a function of the damping. The lower the damping, the more intervals are required for a given level of accuracy. This is because the sharpness of the spike due to the pole singularity and the severity of the discontinunities due to the branch point are inversely related to the damping. The I_1 interval converged to six figures with 500 intervals for a damping of one percent. The comparison studies used as many as 3000 intervals for 1/4 percent damping.

For this application, it was found that the upper limit k_1 usually

occurred before the first two or three zero crossings of the Bessel function. Therefore the singularity problem is confined to lower values of the wavenumber (k). This simplified the treatment of the Bessel function oscillation and slow convergence because the integrand is well-behaved for larger wavenumbers.

This approach is applicable to the multilayered problem as well because the higher-order modes shown in Figure 9 all occur at lower wavenumbers than the Rayleigh pole. The higher-order modes resulting from the layering behave similarly to the Rayleigh surface wave mode; i.e., they become less sharp as damping is increased. Therefore, the same spacing and upper limit (k_1) can be used for evaluating I_1 for the multi-layer problem. This approach eliminates the need for adaptive integration schemes. Adaptive integration algorithms vary subinterval widths depending on convergence of subintervals with varying orders of approximating polynomials, as in Apsel and Luco (1983). These adaptive schemes, while being very versatile and accurate, require a lot of computational overhead since convergence decisions must be made at every step of the integration.

The integrand can be expanded for large wavenumber k ($k>>k_T^*$) in a descending power series as follows:

$$\frac{\nu}{F(k)} = a_o/k + a_1/k^3 + a_2/k^5 + \ldots \tag{39}$$

where the a_o, a_1, a_2... are frequency-dependent complex coefficients. The first term a_o can be readily evaluated from (26c) as follows:

$$a_o = \frac{-1}{2(k_T^2 - k_L^2)} \tag{39a}$$

The c_1 constant in (38) is determined by the convergence of the integrand to the asymptotic form (39). A convergence ratio is defined as follows:

$$\frac{\nu/F(k)}{a_o/k} \tag{40}$$

The c_1 constant in (38) is determined by substituting $c_1 k_T^*$ into (40). When the real part of the ratio is sufficiently close to unity (usually = 1.03), that c_1 value is used. Figure 10 shows the oscillatory part of the integral and typical limits of the I_1 integration.

The second term (I_{p2}) is used to extend the integration out far

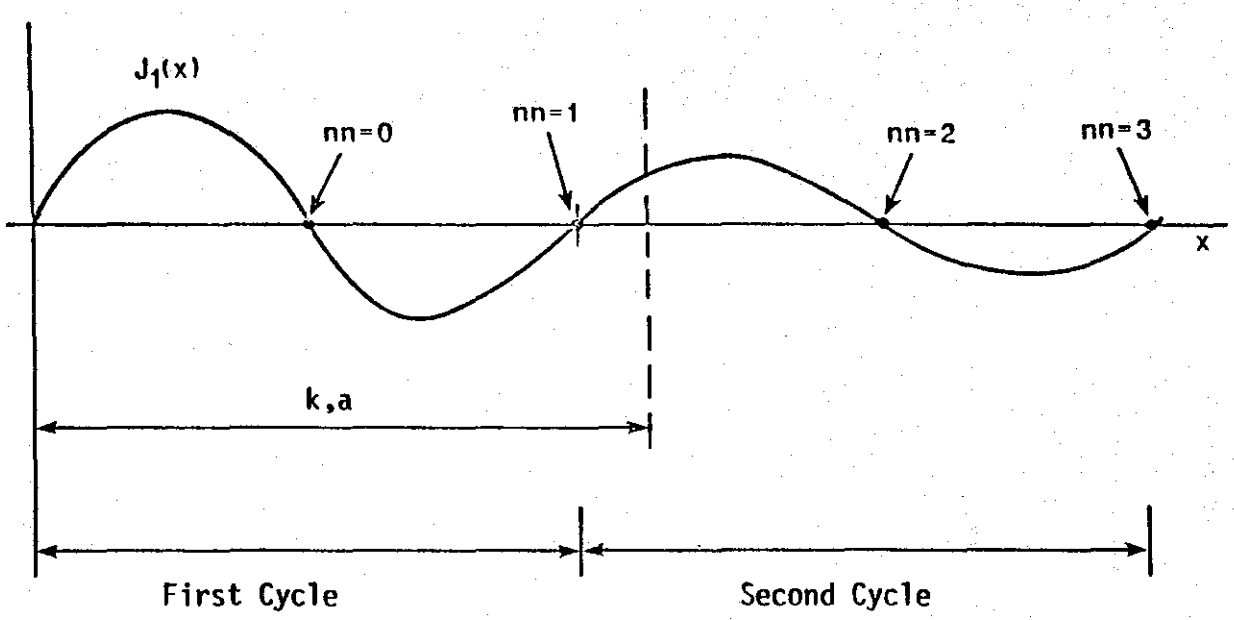

Figure 10. Integration Limits and Their Relation to the Oscillatory Integrand.

enough for the error term estimate to reach the desired level of accuracy. The k_N upper limit corresponds to truncation of the integration at the N^{th} cycle of oscillation of the Bessel function (See Figure 10). The integration for I_{p2} is performed in steps by breaking it into subintervals between each zero crossing of the Bessel function. Simpson's rule with 100 subintervals was used for each interval between zero crossings. Usually the upper limit is taken as N=20 to 40 cycles.

The error term is obtained by estimating the truncation error based on Zhongjin's (1987) method. The error is taken as the integral:

$$\text{err} = \int_{k_N}^{\infty} \frac{\nu}{F(k)} J_1(ka)dk \tag{41}$$

The lower limit (k_N) is set so that the following asymptotic expression for the Bessel function can be used to sufficient accuracy:

$$J_1(x) \approx [\ 2/(\pi x)\ ]^{\frac{1}{2}} \sin\ (x-\pi/4) \tag{42}$$

The details of the method are worked out in Zhongjin (1987) for several examples. The procedure is summarized in words as follows: The infinite integration in (41) is replaced by an infinite sum of integrals over each cycle of the sine curve in (42). Each cycle has two parts: the first positive part and the second negative part. The integrals are evaluated over the first and second part by taking a constant upper bound to the nonoscillatory part of the integrand for the first part and a constant lower bound for the second part. Then since from (39) the nonoscillatory part of the integral is a decreasing monotonic hyperbola, an upper bound estimate of the contribution to each cycle can be obtained explicitly. This can be seen from Figure 11 where the nonoscillatory and oscillatory parts of the integrand are shown for one cycle. Because of term cancellation between cycles, the infinite sum reduces to a single term: the positive part of the first term. The upper bound on the error for I_p is then given as:

$$\text{err} \leq (2/a)\ [2/(\pi a)]^{\frac{1}{2}}\ \frac{\nu(k_N)}{F(k_n)}\ \frac{1}{\sqrt{k_N}} \tag{43}$$

This result is very efficient computationally as the integrand is evaluated only once at the truncation point k_N.

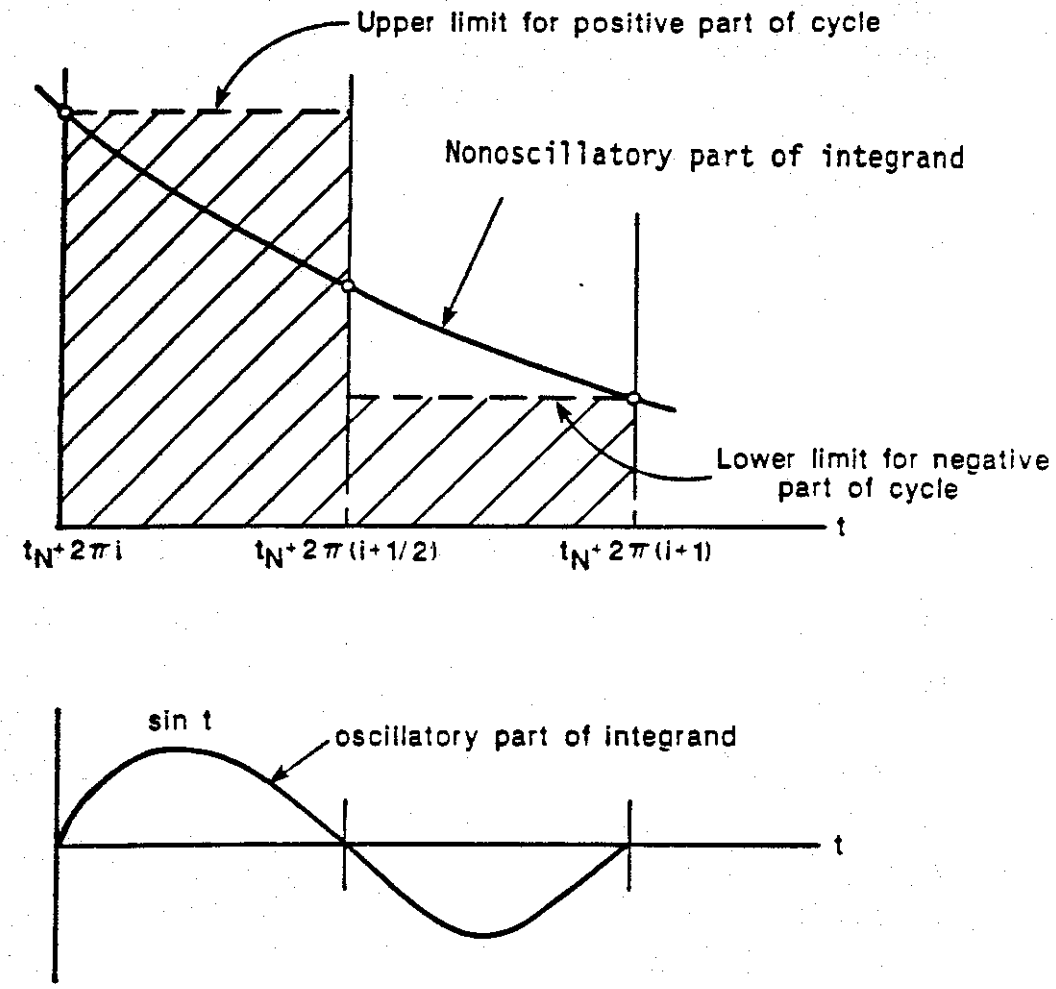

Figure 11. Graphical Interpretation of Zhongjin's Method Over One Cycle of Oscillation.

The modification in Zhongjin's approach used in this study was in using the result (43) to obtain a quantitative value of the truncation term instead of just an estimate of the error. This was done by observing from Figure 11 that a lower limit to the infinite sum form of the truncation error can be constructed to the same order of accuracy as the upper sum (43). One takes a constant lower limit to the first part of the cycle and a constant upper limit to the second part of the cycle. Since these are the same, the difference in areas is then zero. Therefore, the estimate of the error term in (37) is taken as the average of the upper and lower bound limits. This is just one-half the upper bound estimate in (43) or:

$$\text{error term} \cong \text{err}/2 \tag{44}$$

While this approach may not be rigorous mathematically, it gives very good results for known integrals with very slow convergence. Results using the method for integrating the Bessel function in Equation (35) were shown in the last column of Table 2. The error term used is the same as (43) with a = 1 and $\nu/F = 1$. The table shows six-figure accuracy after about 20 cycles of the integrand. The truncated integral at the same point is low by about seven percent. This means that for a given accuracy, the method reduces drastically the point of the truncation, reducing computer time considerably. The error estimation method was used on other known integrals: $\sin x/x$ and $\sin x/\sqrt{x}$ with similar results.

The accuracy of the method for more general integrals such as (34b) cannot be determined directly because a closed-form solution is not available for comparison. However, the method was applied where the integrand approaches the hyperbolic shape given by (39) and (39a), so the error should behave similarly to the Bessel function integral (35). Indirect comparisons of results with elastic (zero damping) solutions are shown in Chapter VI.

CHAPTER V

DEVELOPMENT OF COMPUTER PROGRAMS

The computer program development was done on the TAMU Engineering Computer Services VAX 8650 SIGMA node. The computations for surface displacement were performed on three programs written in C language (Kernighan and Ritchie, 1978). The programs are referred to by their filenames as SCR.C (for $r = 0$, uniform load), DELTA.C (point load), and SUP.C (uniform load, $r \neq 0$). All three programs use the same two "header" files: header.c (for complex algebra functions) and bessel-functions.h (for Bessel function computations). The header files are "included" in the program by preprocessor commands at the beginning of the program listings. The three programs are shown in block diagram form in Figures 12, 13, and 14. The block diagrams indicate the sequence and hierarchy of each of the function "calls." Each block indicates a separate module called a function in c language. The group of programs and files is referred to as the SCALPOT program, an acronym for "scalar potential."

The C language was used (instead of, e.g., FORTRAN or BASIC) because "C" language is closer to assembly language, so it can result in faster, more efficient code. In addition, "C" language is portable, supports structured programming, and is able to pass values instead of references to addresses.

The programming effort was intended to yield a specified, controlled level of accuracy for the final results. All floating-point computations were done in double-precision arithmetic. Each module was designed to give six significant figure accuracy by setting specific constants or parameters. Computation time can be reduced by relaxing the six-figure accuracy. No attempt was made to optimize running time, and no tradeoff studies between accuracy and running time were attempted at this stage of the effort.

Since "C" language does not support complex albegra computations (as does FORTRAN), it was necessary to construct functions to perform the basic complex algebra operations such as addition, multiplication, division, and square root. The complex algebra was handled by making each

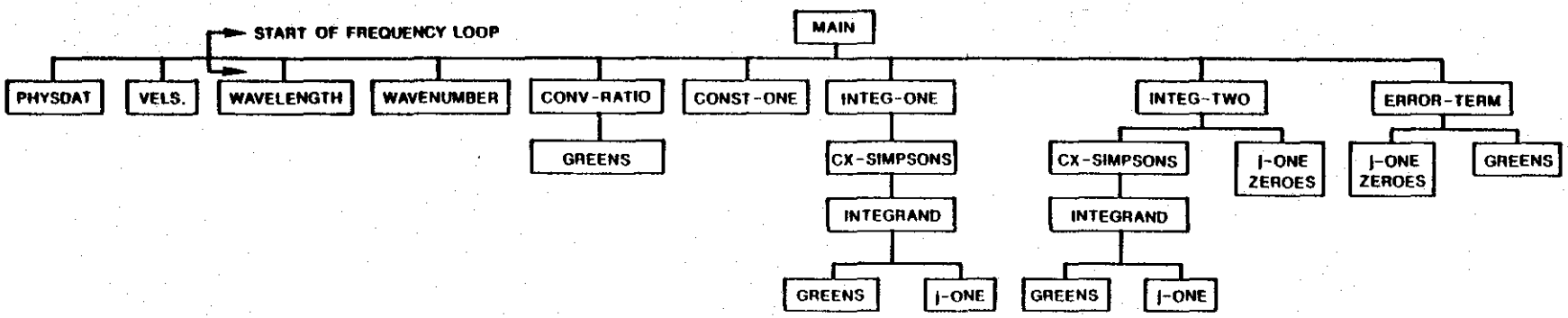

Figure 12. Program Structure for SCR.C File for Computing Response from Uniform Load for r = 0.

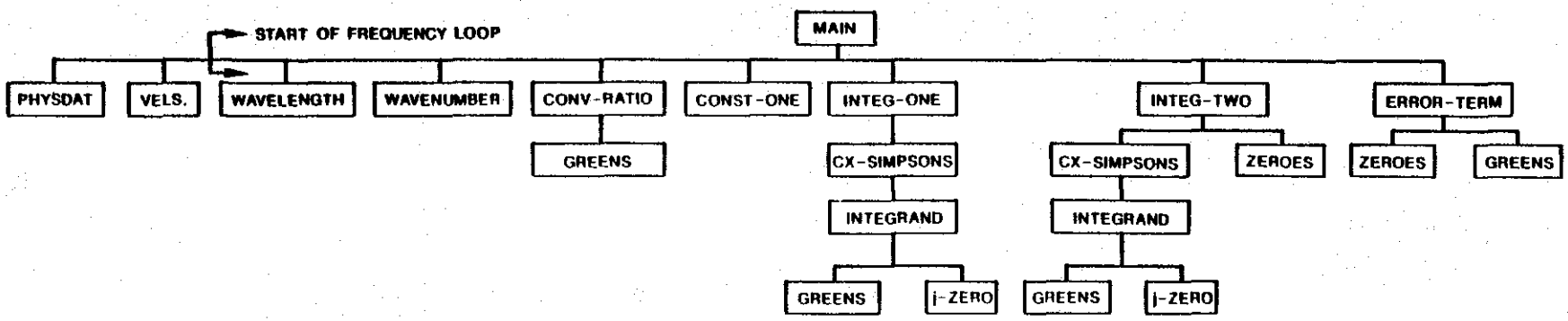

Figure 13. Program Structures for DELTA.C File for Computing Responses to Point Load.

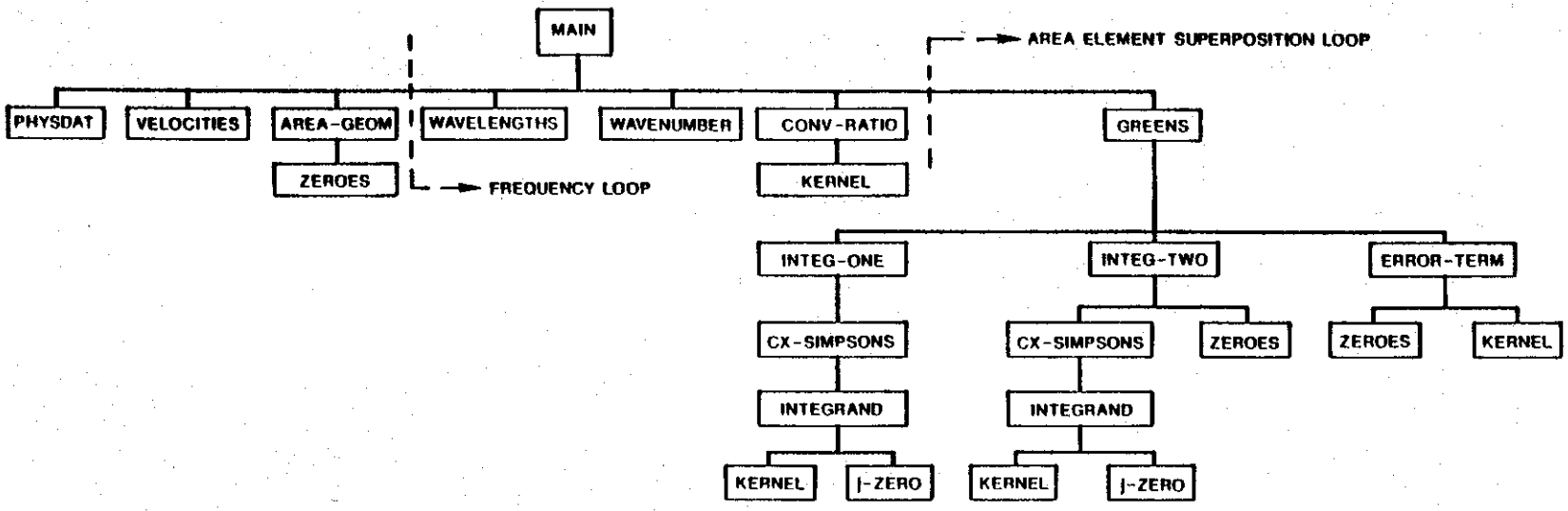

Figure 14. Programs Structure for SUP.C File for Computing Responses from Uniform Load for Field Point Outside Load Disk (r > a).

complex number or variable a two-element array: the first element being the real part and the second the imaginary part. The strategy used for the complex algebra function works like this:

cx-operation (operand-1, operand-2, result)

where cx-operation is the function name or "call" for a binary operation on complex operands, operand-1 and operand-2. The result of the computation is "passed" as the third parameter result. All three parameters represent addresses for the respective variables as they are complex number arrays.

A unary operation on a complex number resulting in a scalar value can be written as follows:

double cx-mod (operand)

where "double" refers to the function returning a double precision value, cx-mod designates the operation (complex modulus) and operand is the address of the complex number to be operated on. A "return" statement in the function returns the scalar value wherever the function cx-mod appears (is called) in the program, according to the values of the operand's elements.

The Bessel functions $J_o(x)$ and $J_1(x)$ for real arguments must be computed. The respective zeroes of the Bessel functions are required as well; x_k must be computed where:

$$\left.\begin{aligned} J_o(x_k) &= 0 \\ J_1(x_k) &= 0 \end{aligned}\right\} \quad k = 0, 1, 2, \ldots$$

The header file for the Bessel function contains four functions: jzero, zeroes, j-one and j-one-zero. Each function uses the polynomial approximations in Chapter 9.4 of Abramowitz and Stegun (1972). The J_o function uses the expressions 9.4.1 and 9.4.3, and the J_1 computation uses 9.4.4 and 9.4.6. The J_o and J_1 zeros are computed from McMahon's expansion for large zeroes in Equations (9.5.12) and from Table 9.5, which gives the first 20 zeroes for J_1 and J_o to 10b decimal places. Each computation is for a polymonial of the form:

$$f(x) = a_o + a_1x + a_2x^2 + \ldots a_nx^n, \; n = \text{integer}$$

The polynomials were expressed in recursive from using nesting as follows:

$$f(x) = [\ldots([(a_n x+a_{n-1})x+a_{n-2}]x+a_{n-3}) \ldots+a_o]$$

The nested form is more efficient computationally, requiring only one multiplication and one addition for each increase in order, while the normal polymonial form requires an exponentiation, a multiplication, and an addition for each term.

The only numerical integration function used was Simpson's rule, or the 1-4-1 rule which corresponds to a cubic "fit" or interpolation between equally spaced ordinates. This was used for expedience, and a higher-order, more efficient routine (such as Gaussian integration) can be readily substituted at a later date.

All three programs are structured similarly, so only the most complicated, SUP.C, which uses superposition to obtain the response, will be described in detail. The SUP.C program contains the superposition loop (Equation 31d) which is not needed in the other two. The main purpose of the program is to compute and print out the dimensionless magnitude and phase of the vertical displacement at a specified distance r from the center of the uniform pressure distribution. This is done for a predetermined number and spacing of dimensionless frequencies. The displacements are computed by superimposing a weighted addition of responses from point pressure distributions, as in (31d).

The point responses are computed by the module greens, which in turn, calls other modules for each of the three components of the integral as described in Equation 37 of Chapter IV. The module greens is essentially the same as the stand-alone program DELTA.C in Figure 13. The main module for SUP.C "calls" the functions on the second row in Figure 14 in left to right order, performs minor computations, and prints out most of the results. The module physdat reads in the physical data on the half-space from a separate data file. The function velocities computes the compressional and shear wave velocities for zero damping using the data from physdat. The function area-geom computes parameters for the area elements required for the superposition computation. It also prints out information on the geometry of each element. Everything to the right of area-geom is included in the frequency loop. The wavelengths module

computes and prints out the wavelengths for the compressional and shear waves, assuming no damping. The wavenumber module computes the complex wavenumbers including damping. The conv-ratio function computes the upper limit (k_1) of the first integral and checks on the convergence of the integrand to its asymptotic value for large k. Everything to the right of this module is inside the element superposition loop. The superposition loop performs the following weighted addition:

$$u_z = \frac{1}{A} \sum_{j=1}^{nn} \Delta A_j \; g(R_j) \qquad (31d)$$

where u_z is the displacement, A is the load disk area, ΔA_j is the element area and $g(R_j)$ is the point load response for the j^{th} element whose centroid is a distance R_j from the field point (r), as in Figure 7. The surface elements used in the discretization are shown in Figure 15. The summation is a numerical approximation to the superposition integral in Equation 31c of Chapter III. The function greens computes the point load response for each element. Greens in turn calls three functions: integ-one, integ-two, and error-term. Integ-one computes the first integral component I_1, integ-two computes the second integral I_2, while the truncation error estimate is computed in error-term, as in Equation 37 of Chapter IV. Both integ-one and integ-two call the complex Simpson's rule integration function cx-simpsons. Integ-two also calls zeroes because it integrates in intervals between respective zeroes of the Bessel function. The integrand is computed in function integrand by multiplying the complex frequency-dependent part called in kernel by the real oscillatory Bessel function part in jzero. The error-term function calls zeroes and kernel just once to evaluate the zero at the point of truncation of the integral.

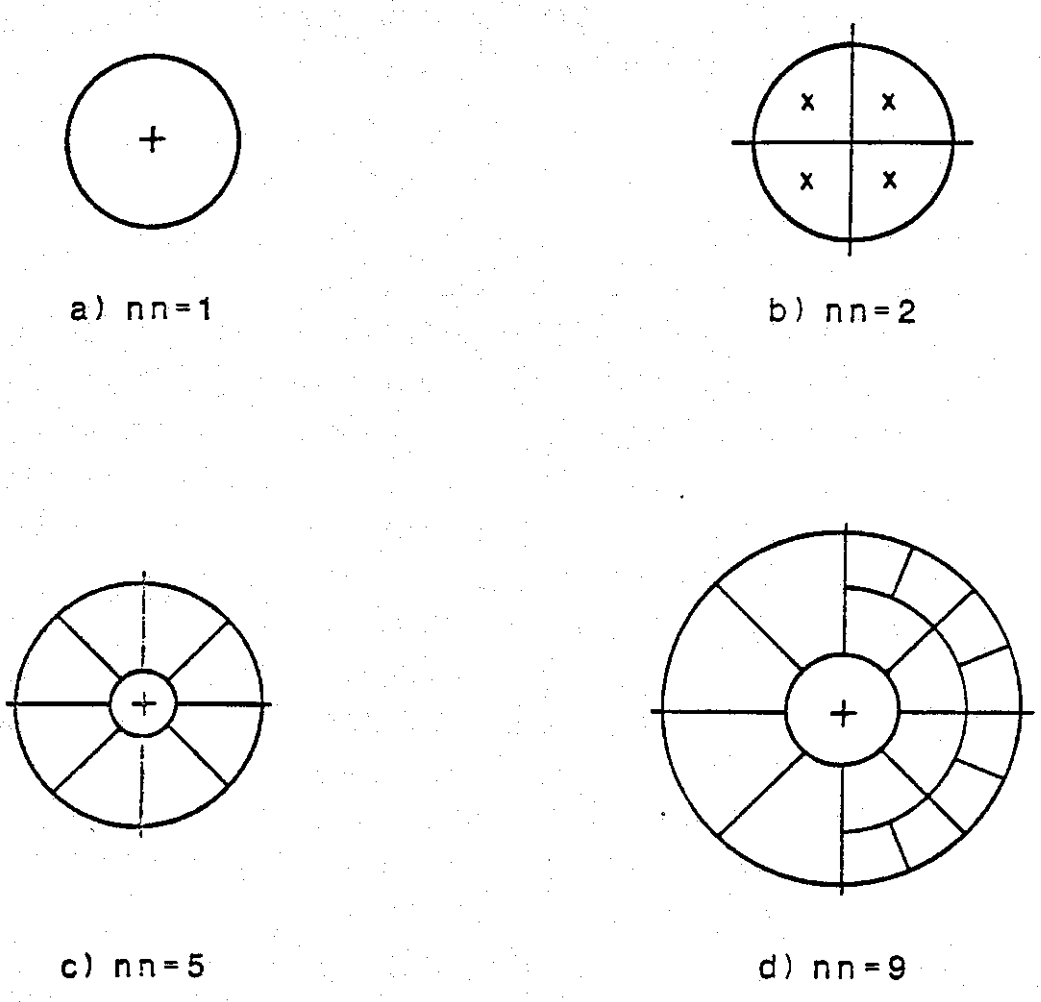

Figure 15. Surface Elements for nn = 1, 2, 5 and 9.

CHAPTER VI

RESULTS

Results of computation of surface displacements are presented in this chapter. The computations were verified by comparison with results of related investigations. The purpose of the surface displacement computations was to compute the displacements at r = 0, 1, 2, 3, 4, 5 and 6 ft. for a uniform circular pressure distribution of radius a = 0.4295 ft. in order to duplicate the geometrical test conditions of the Dynatest Falling-Weight Deflectometer apparatus. The r = 0 case is treated separately, as it can be integrated directly from Equation (34a). This was done in program SCR.C, which was compared with the Reissner-Sung Theory discussed in Chapter II. The r = 1, 2, 3, 4, 5 and 6 ft. cases are done using the SUP.C program that uses superposition of the point pressure distribution, Equation (31d). Verification of the superposition program was done in two steps: the point load response computation in program DELTA.C (that integrates Equation [30]) was compared with the elastic half-space computations of Wong (1975). Then the superposition program SUP.C was verified with the approximate solutions of the UTFWIBM program discussed in Chapter II. Therefore, the overall verification study was done in three phases using data from three independent sources.

A direct comparison with the Reissner-Sung and Wong's results was not possible because their computations were for an elastic half-space (zero damping). Because of the method of integration described in Chapter IV, the computed results in this study must have some damping. Therefore, the comparisons were made by computing responses for several damping ratios and looking for convergence of the responses to the elastic limit as damping approaches zero.

Reissner-Sung Comparison: r = 0 Response for Uniform Load

Computed results were compared to the Reissner-Sung elastic half-space solution discussed in Chapter II. The elastic half-space solution, when presented in dimensionless form using f_1, f_2, and a_o as defined in Equation (32), is only a function of the Poisson's ratio. Comparison

curves were computed using Sung's (1953) polynomal forms presented in his Tables II and III for Poisson's ratio of 0, 1/4, 1/3 and 1/2. The results are presented in Figures 16a and 16b for the f_1 (in-phase) versus a_o (dimensionless frequency), and the f_2 (out-of-phase) versus a_o plots, respectively. The elastostatic solution corresponds to the zero frequency point, where the f_1 is a constant decreasing with Poisson's ratio, and f_2 is zero. The dynamic effects are seen in the variation of the response functions with frequency. The f_1 curves fall off or decrease gradually with frequency (at least in the range of a_o from 0 to 1.5). The f_2 curves start at zero and are approximately linear with frequency, curving downward slightly at higher frequencies.

The dynamic response is better represented by taking the magnitude and phase angle representation as in Equation (32a). This representation is used for most of the comparisons below.

Two comparison studies were performed: one for a Poisson's ratio of 1/4 using the f_1, f_2 format, and another using Poisson's ratio of 1/3 (which is closer to highway materials) and the $|f|$, ϕ_f (magnitude, phase angle) representation.

The results of the first study are shown in Figures 17 and 18 where f_1 and f_2, respectively, are plotted against a_o. Computed values are shown for damping of one percent and two percent. The in-phase results are close to the elastic solution with the solution apparently converging uniformly to the elastic (zero-damping) solution as the damping is decreased. The one percent damping result is accurate to better than two significant figures. The out-of-phase f_2 results in Figure 18 show the same uniform convergence to the elastic solution as damping is decreased.

The second comparison was performed for lower damping ratios: 1/2 percent and 1/4 percent for Poisson's ratio of 1/3. The comparison of magnitude $|f|$ is shown in Figure 19 where the computed results are very close to the elastic solution. The magnitude response is seen to be quite flat, falling off slightly with increasing frequency. The same results are replotted in Figure 20 on an expanded scale. The 1/4 percent damping curve compares within two or three significant figures to the elastic solution. Figure 21 shows phase angle versus frequency. The phase angle is nearly linear with frequency, and this characteristic was seen through-

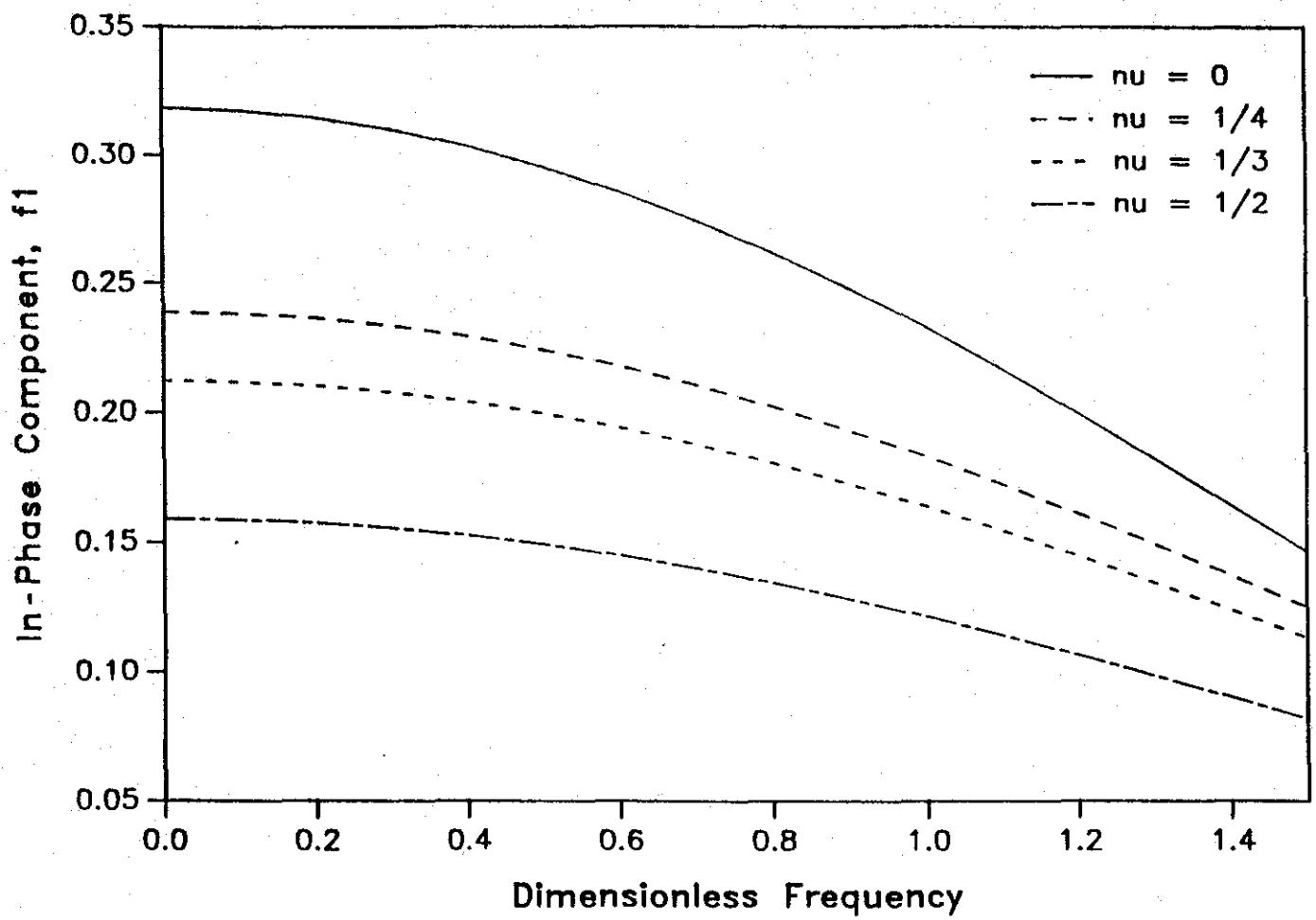

Figure 16a. In-Phase Dimensionless Normal Displacement for r=0 and Uniform Pressure Distribution Versus Dimensionless Frequency for Poisson's Ratio of 0, 1/4, 1/3 and 1/2 (from Sung, 1954).

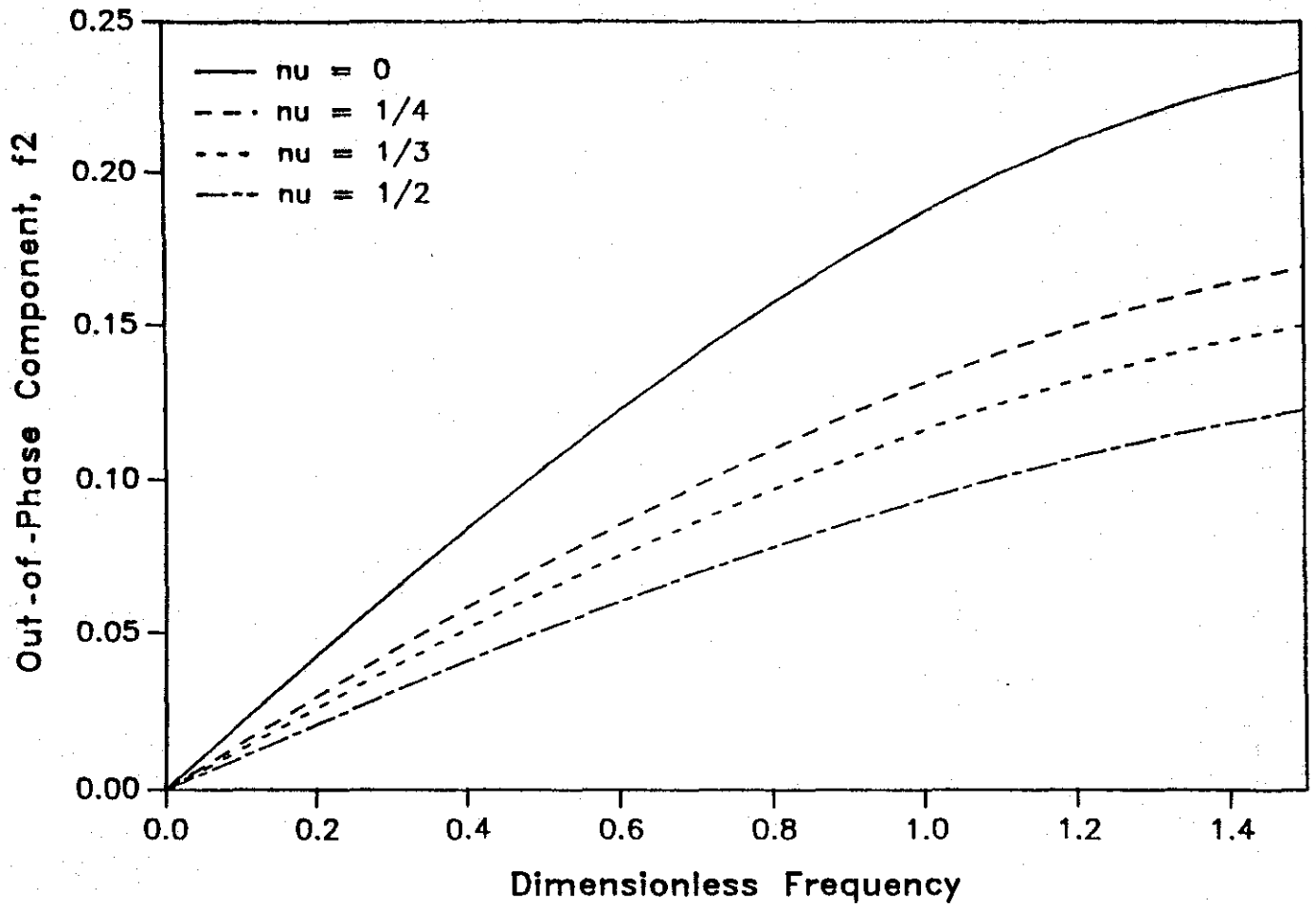

Figure 16b. Out-of-Phase Dimensionless Normal Displacement for r=0 and Uniform Pressure Distribution Versus Dimensionless Frequency for Poisson's Ratio of 0, 1/4, 1/3 and 1/2 (from Sung, 1954).

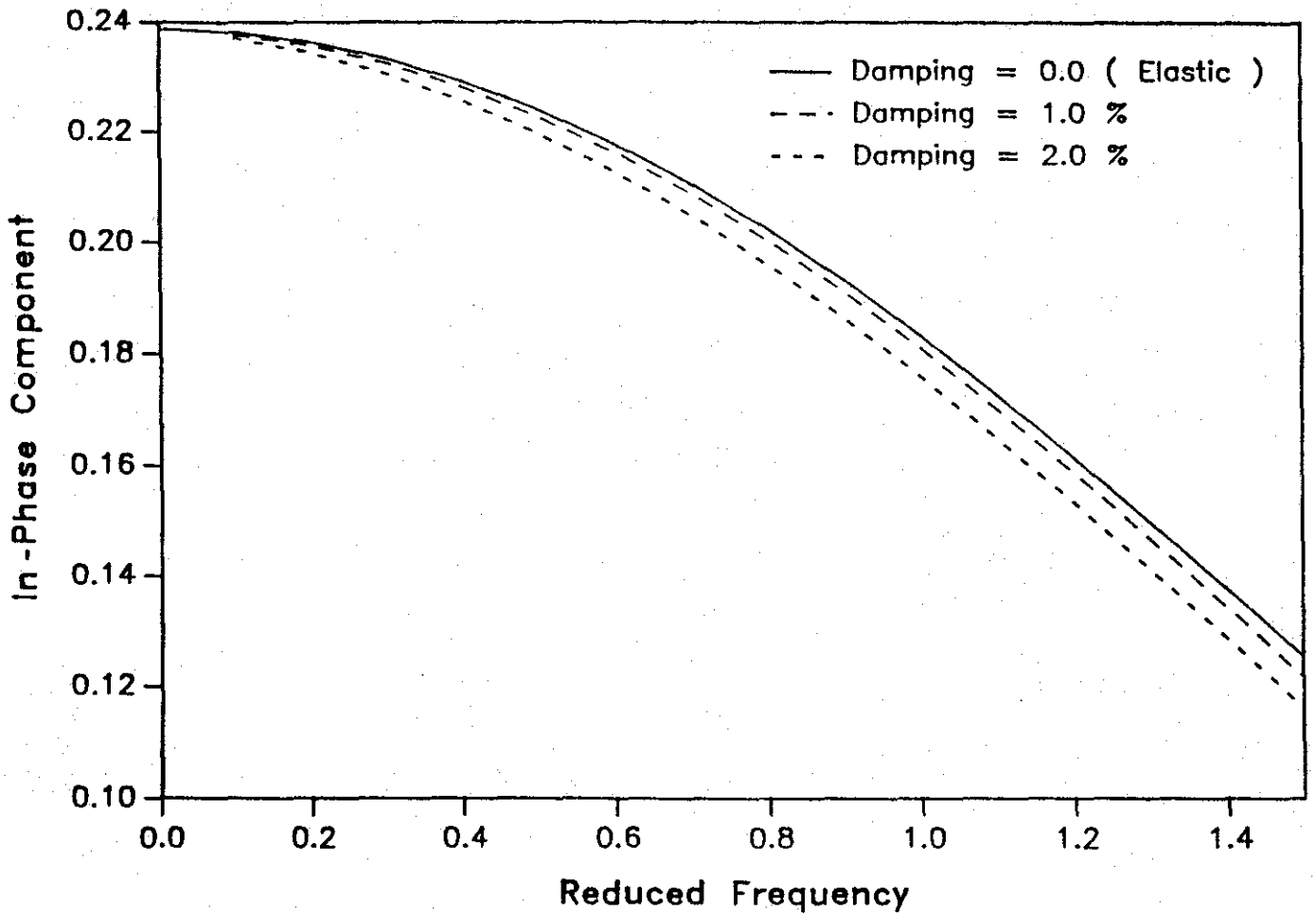

Figure 17. In-Phase Dimensionless Normal Displacement for r=0 and Uniform Pressure Distribution for Poisson's Ratio of 1/4: Comparison of Theory and Computed Values.

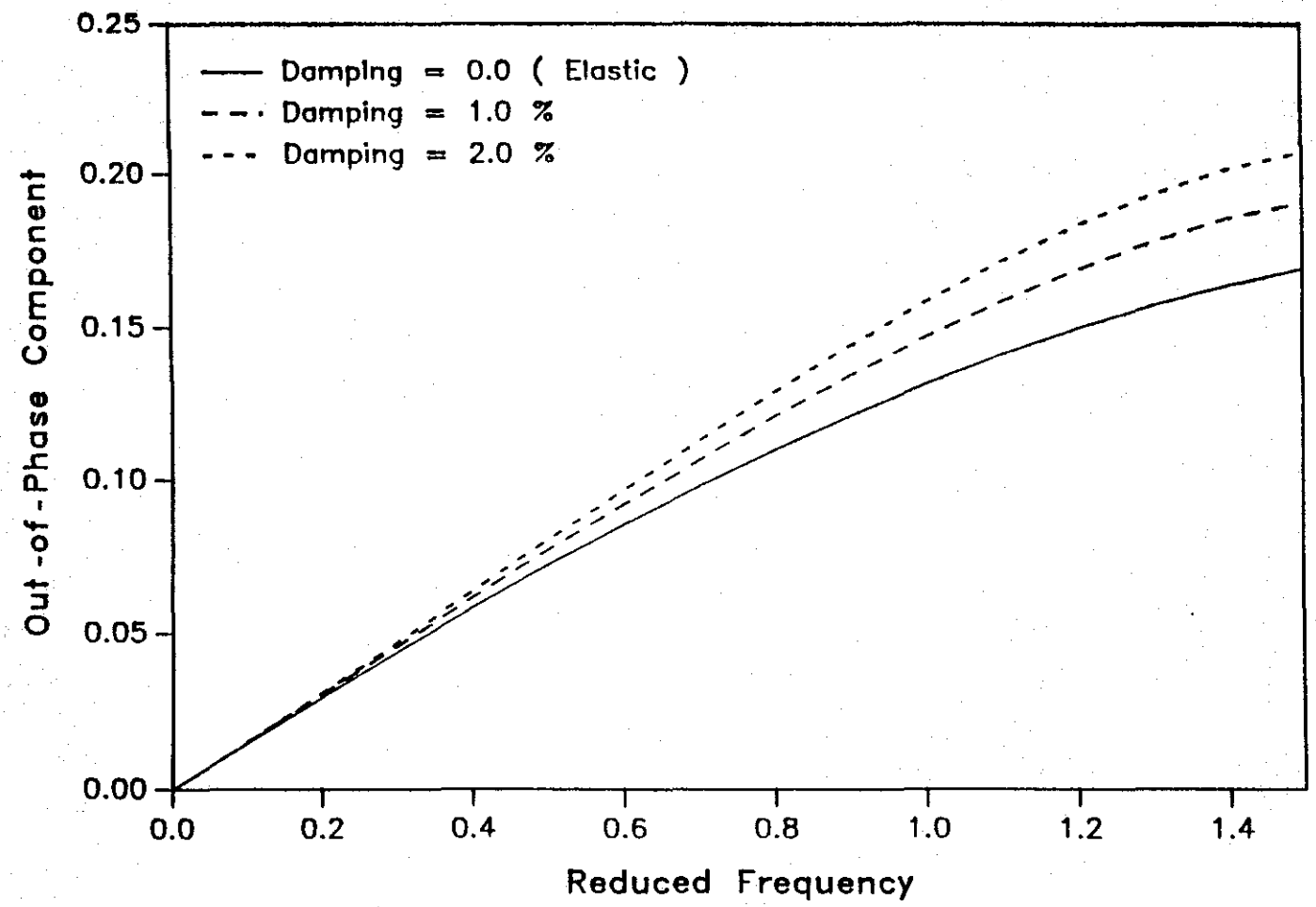

Figure 18. Out-of-Phase Dimensionless Normal Displacement for r=0 and Uniform Pressure Distribution for Poisson's Ratio of 1/4: Comparison of Theory and Computed Values.

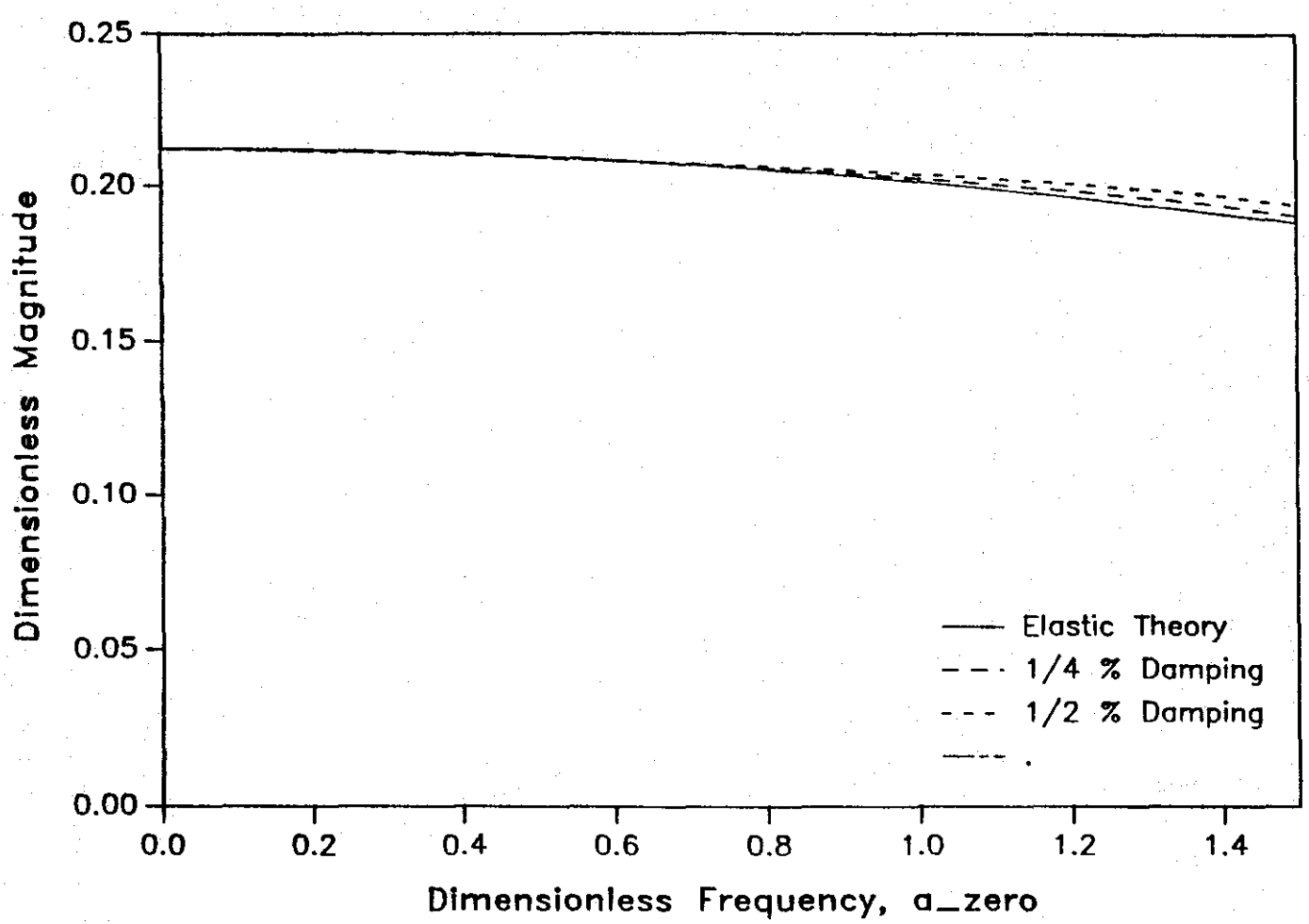

Figure 19. Dimensionless Magnitude of Normal Displacement for r=0 and Uniform Pressure Distribution for Poisson's Ratio of 1/3: Comparison of Theory and Computed Values.

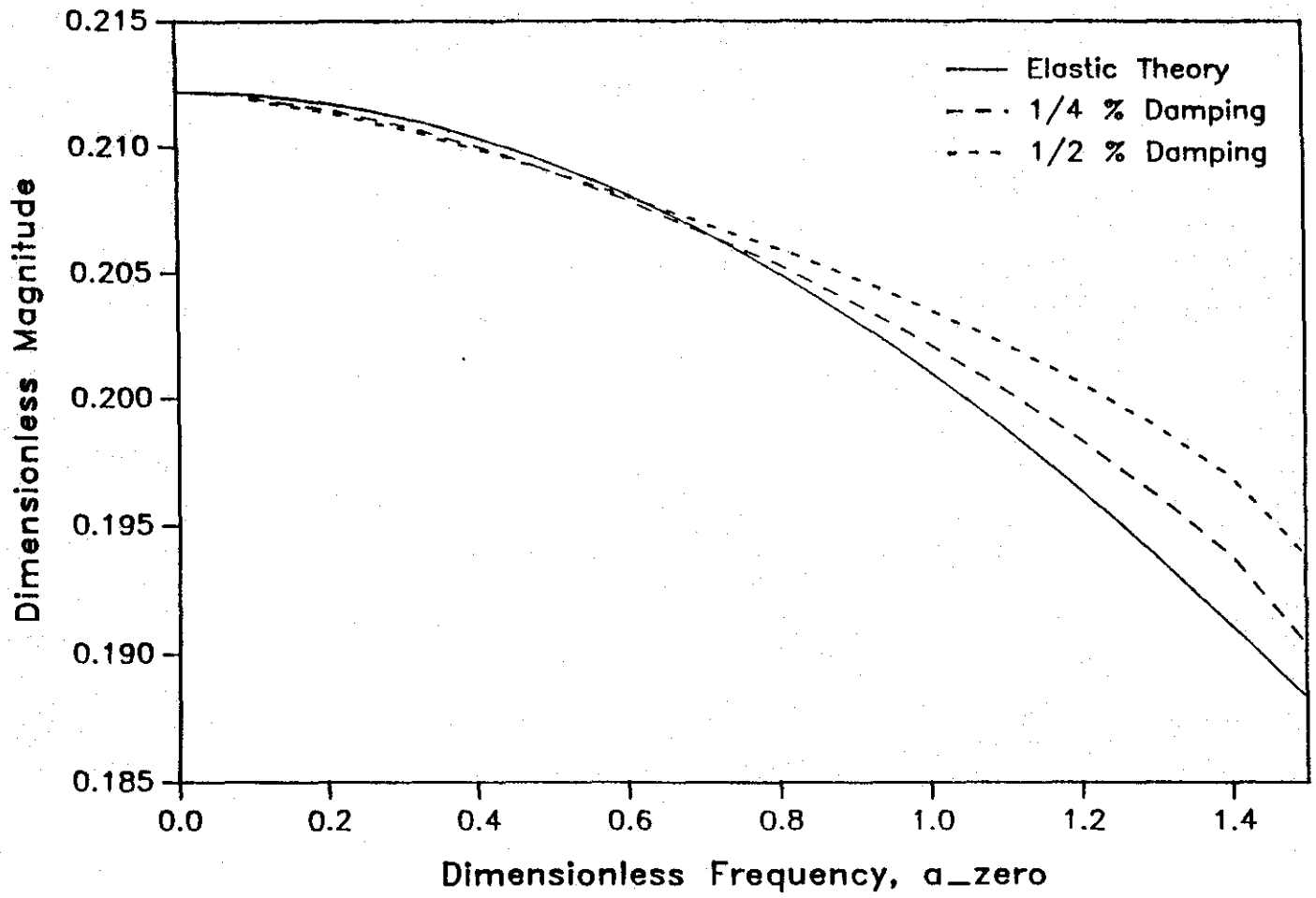

Figure 20. Dimensionless Magnitude of Normal Displacement for r=0 and Uniform Pressure Distribution for Poisson's Ratio of 1/3: Comparison of Theory and Computed Values on Expanded Scale.

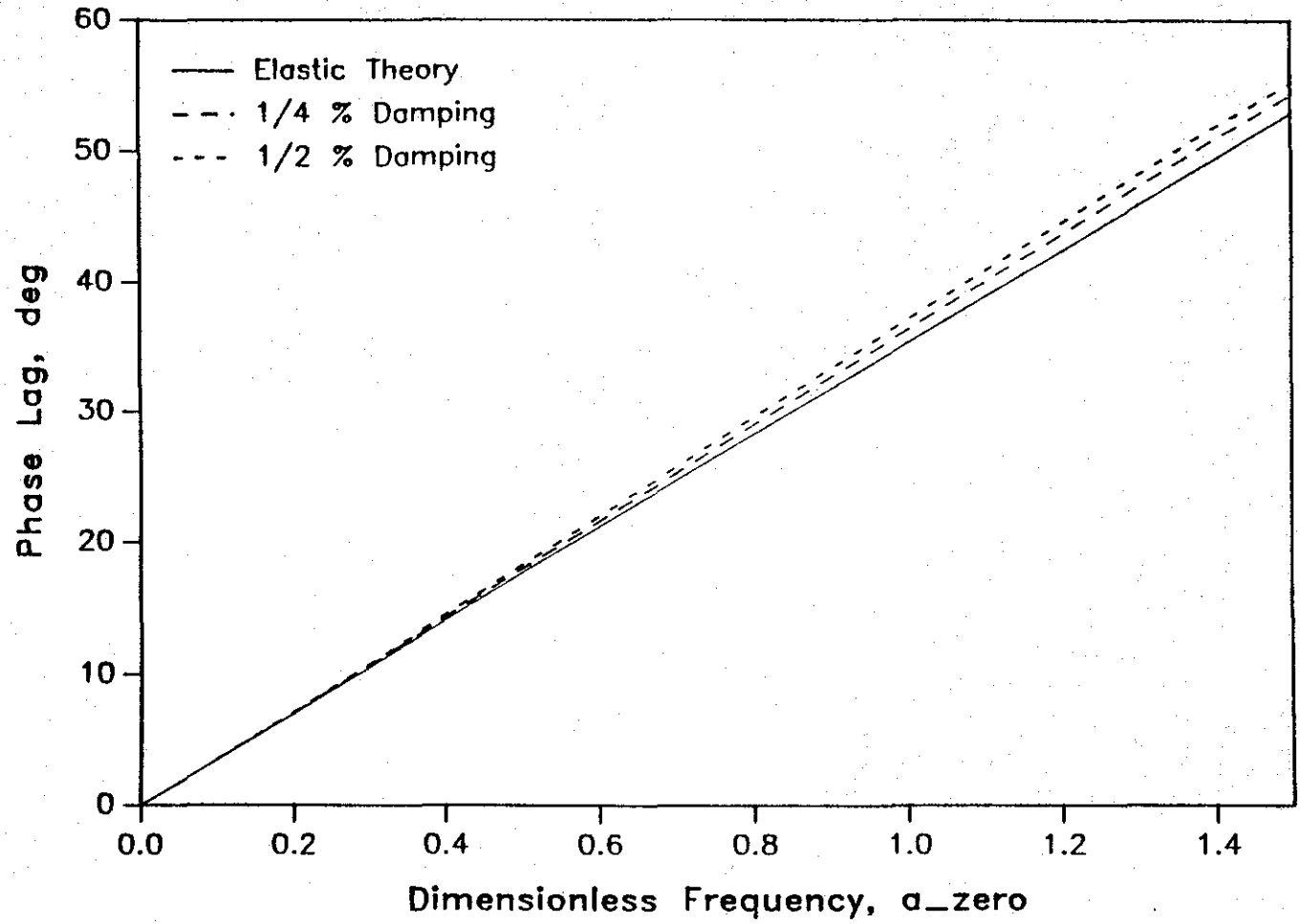

Figure 21. Phase Angle of Normal Displacement of r=0 and Uniform Pressure Distribution for Poisson's Ratio of 1/3: Comparison of Theory and Computed Values.

out the comparison studies. The curves exhibited the same uniform convergence to the elastic results as damping decreases. The phase angle is overestimated by about 2 percent for the 1/4 percent damping. In this case, the phase angle is more sensitive to damping than the magnitude.

Point Load Comparison

This comparison study was performed to verify the Green's function or point load response used in the superposition solution. Wong's (1975) results, cited in Apsel and Luco (1983) on the response from an elastic half-space with a Poisson's ratio of 0.33, were used. The results are shown in Table 3 and Figures 22, 23, and 24. Wong's results are presented in the f_{r1}, f_{r2} versus r_o form (see Equation 33). The real and imaginary components (f_{r1} and f_{r2}, respectively) are seen to be oscillatory, covering approximately one cycle in the indicated range of r_o from 0 to 5.5. The magnitude ($|f_r|$) and phase (ϕ_{fr}) representation of the same data are shown in Figures 23 and 24, respectively. This representation eliminates the oscillation, giving a more regular appearance to the response. The magnitude is seen to increase slightly with frequency,

Table 3

Wong's (1975) Computed Dimensionless Vertical Displacement on the Surface of an Elastic Half-space as a Function of Dimensionless Distance (From Apsel and Luco, 1983).

$r_o = \omega r/c^*$	f_{1r}	f_{2r}
0.0	0.106	0.000
0.5	0.087	-0.062
1.0	0.037	-0.102
1.5	-0.029	-0.108
2.0	-0.087	-0.077
2.5	-0.120	-0.017
3.0	-0.114	0.053
3.5	-0.070	0.110
4.0	-0.001	0.134
4.5	0.072	0.118
5.0	0.127	0.064
5.5	0.144	-0.013

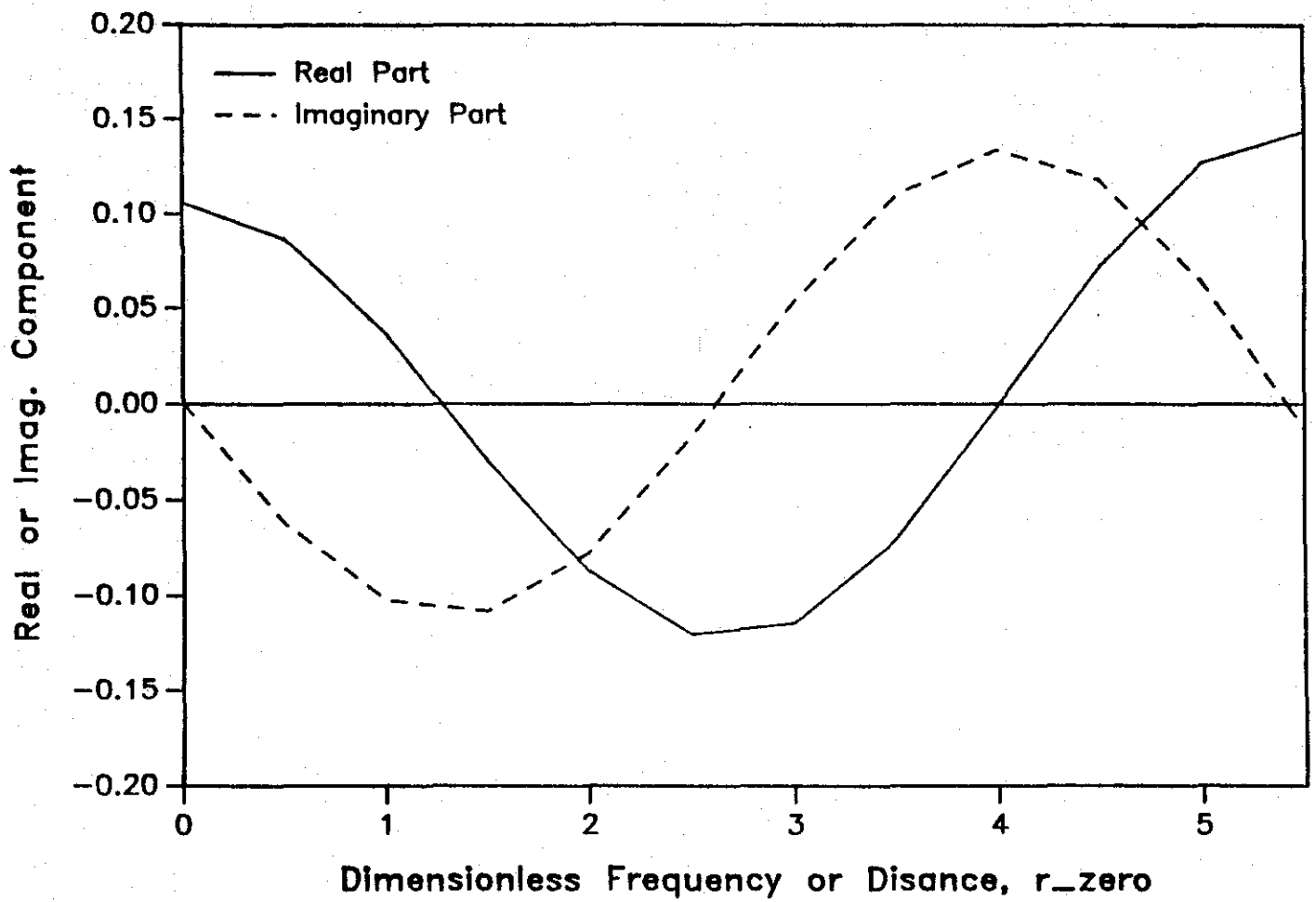

Figure 22. Real and Imaginary Components of Dimensionless Normal Surface Displacement Versus Dimensionless Distance (r_o) for a Point Surface Load on an Elastic Half-Space: Poisson's Ratio = 0.33 (From Wong, 1975).

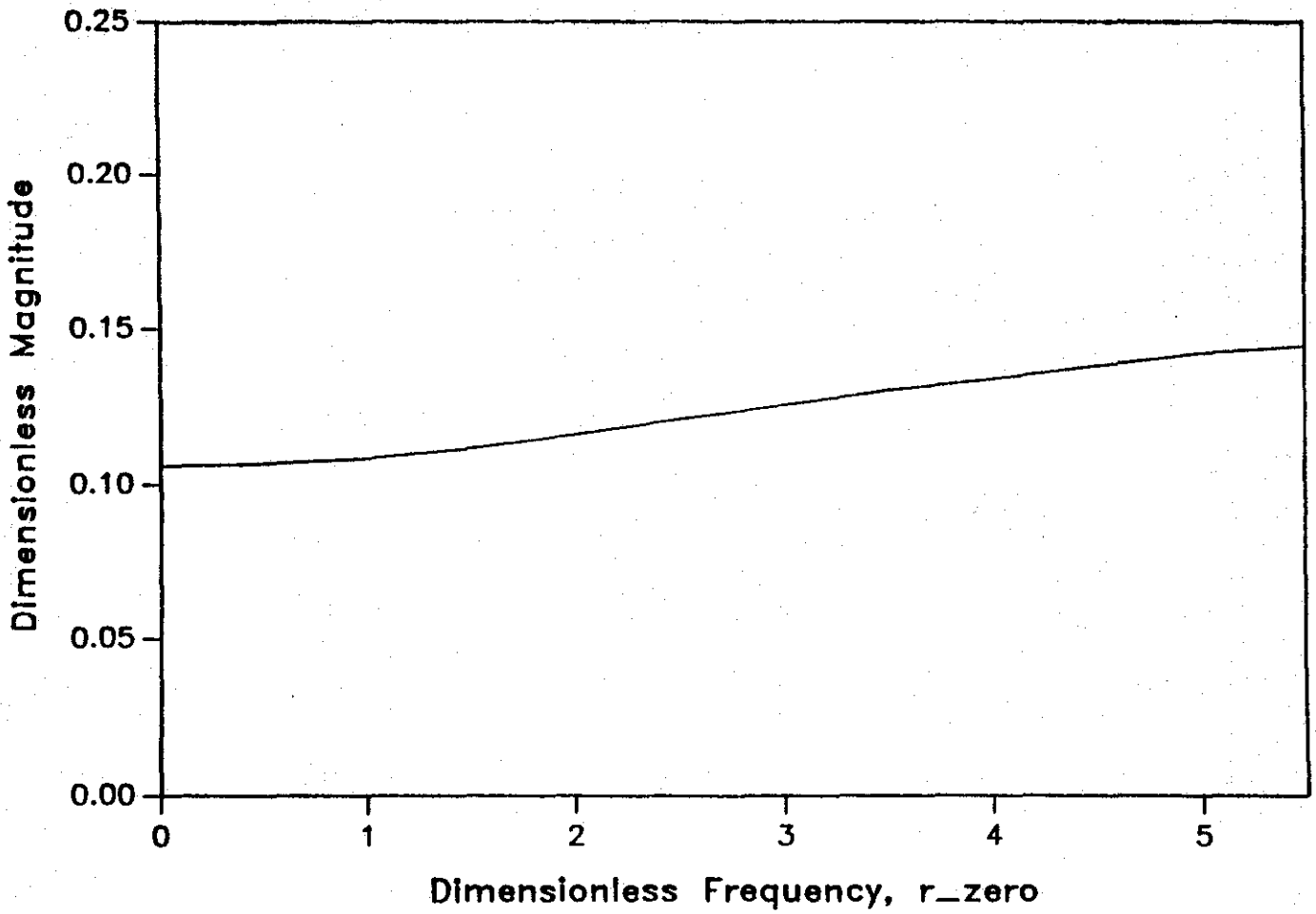

Figure 23. Magnitude of Dimensionless Normal Surface Displacement Versus Dimensionless Distance (r_0) for a Point Surface Load on an Elastic Half-Space: Poisson's Ratio = 0.33.

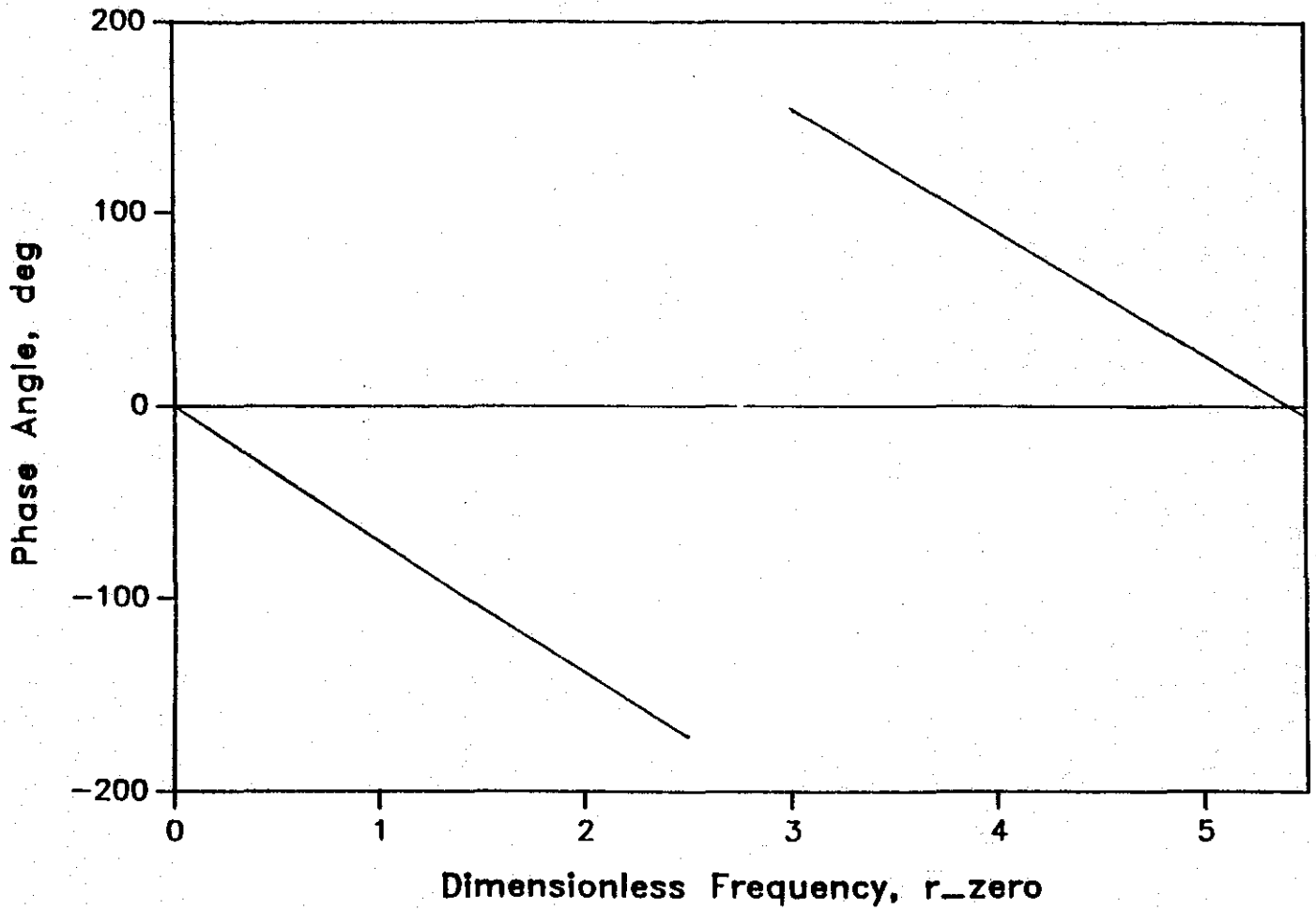

Figure 24. Phase Angle of Dimensionless Normal Surface Displacement Versus Dimensionless Distance (r_o) for a Point Surface Load on an Elastic Half-Space: Poisson's Ratio = 0.33.

and the phase angle is nearly linear in dimensionless frequency, as was the case with the Reissner-Sung comparison. The phase angle plot "jumps" near r_o of 2.5, where the phase angle goes from -180° to +180° because the arctangent is restricted to the principal "branch." That is, the phase angle computed from an arctangent is a lag angle or negative angle where, for instance, a 180° lag angle is the same as a 180° lead angle because of the cyclic nature of angles.

The comparison data was generated using the DELTA.C program for 1, 1/2, and 1/4 percent damping for the same Poisson's ratio of 0.33. The comparison is shown in Figures 25 and 26, where magnitude and phase angle are shown, respectively. One sees in Figure 25, apparent uniform convergence of the computed results to the elastic case as damping is decreased. The accuracy is within three significant figures for the 1/4 percent damping case. The irregularity in the elastic curve is probably due to roundoff error, as the data was given in Table 3 to only three figures. The computed phase angle results overlaid the elastic response for all values of damping to within the thickness of the pen line as can be seen in Figure 26. The branch jump (-180° to +180°), seen in Figure 24, is seen here as well.

Comparison Study for Uniform Load on Plastic Clay Half-space

This comparison was intended to simulate as closely as possible the physical and geometrical conditions for Falling-Weight Deflectometer testing, given that a uniform half-space (unlayered) model was used. The physical constants used for the half-space are intended to represent a plastic clay and are listed as follows:

Young's modulus $E = 30ksi$
Poisson's ratio $\mu = 0.30$
Weight density $r = 120\ lbs/ft^3$

This comparison study is based on results of the UTFWIBM program which uses approximations discussed in Chapter II. The results of UTFWIBM runs for r = 0, r = 6 ft, and r = 1 ft. were reduced to dimensionless form for frequencies ranging from 4 to 97.7 Hz. The computed results for r = 0 were generated from the SCR.C program, while the results for r = 1 and

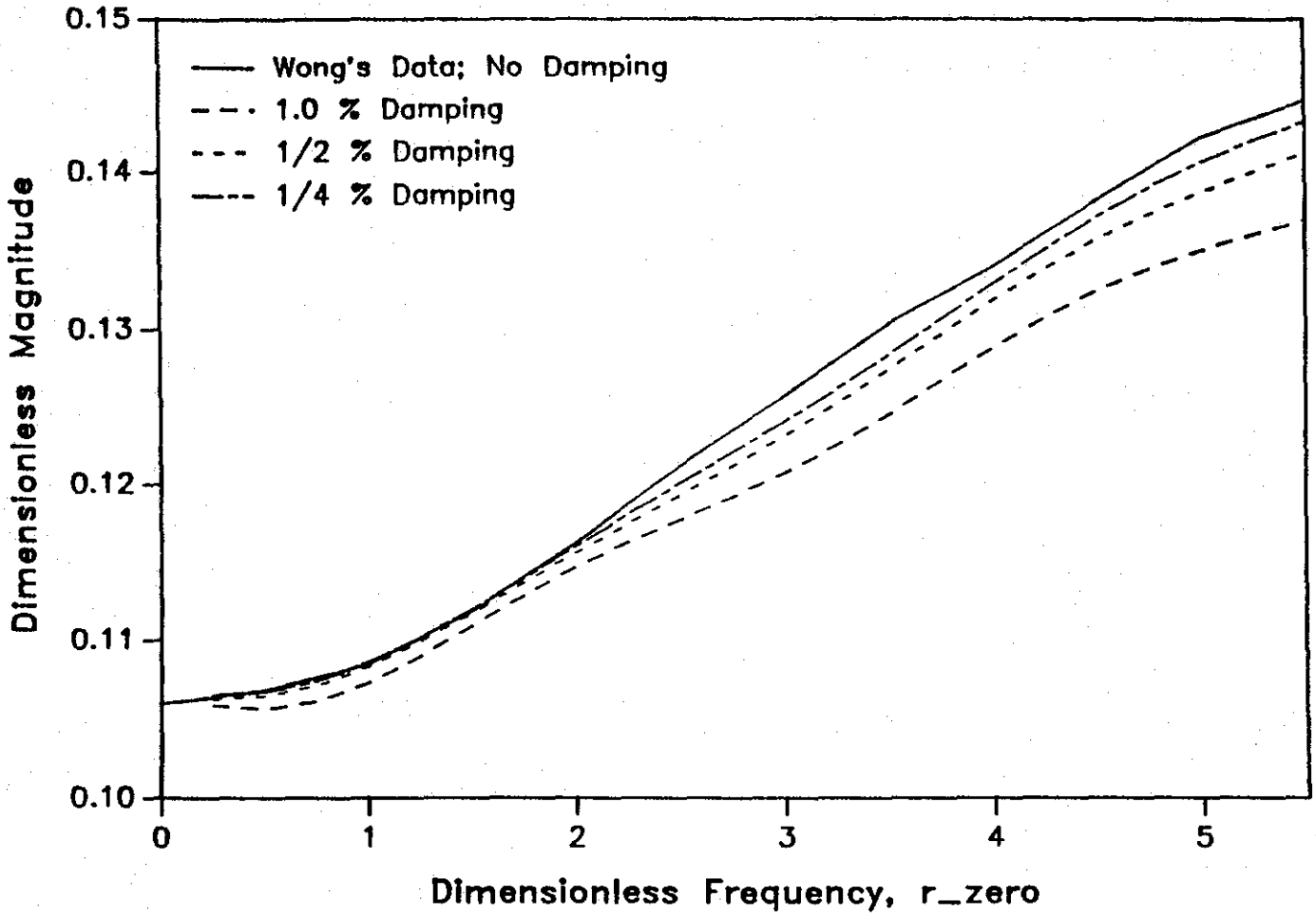

Figure 25. Magnitude of Dimensionless Normal Surface Displacement Versus Dimensionless Distance (r_0) for a Point Surface Load: Poisson's Ratio = 0.33, Comparison of Theory and Computed Values.

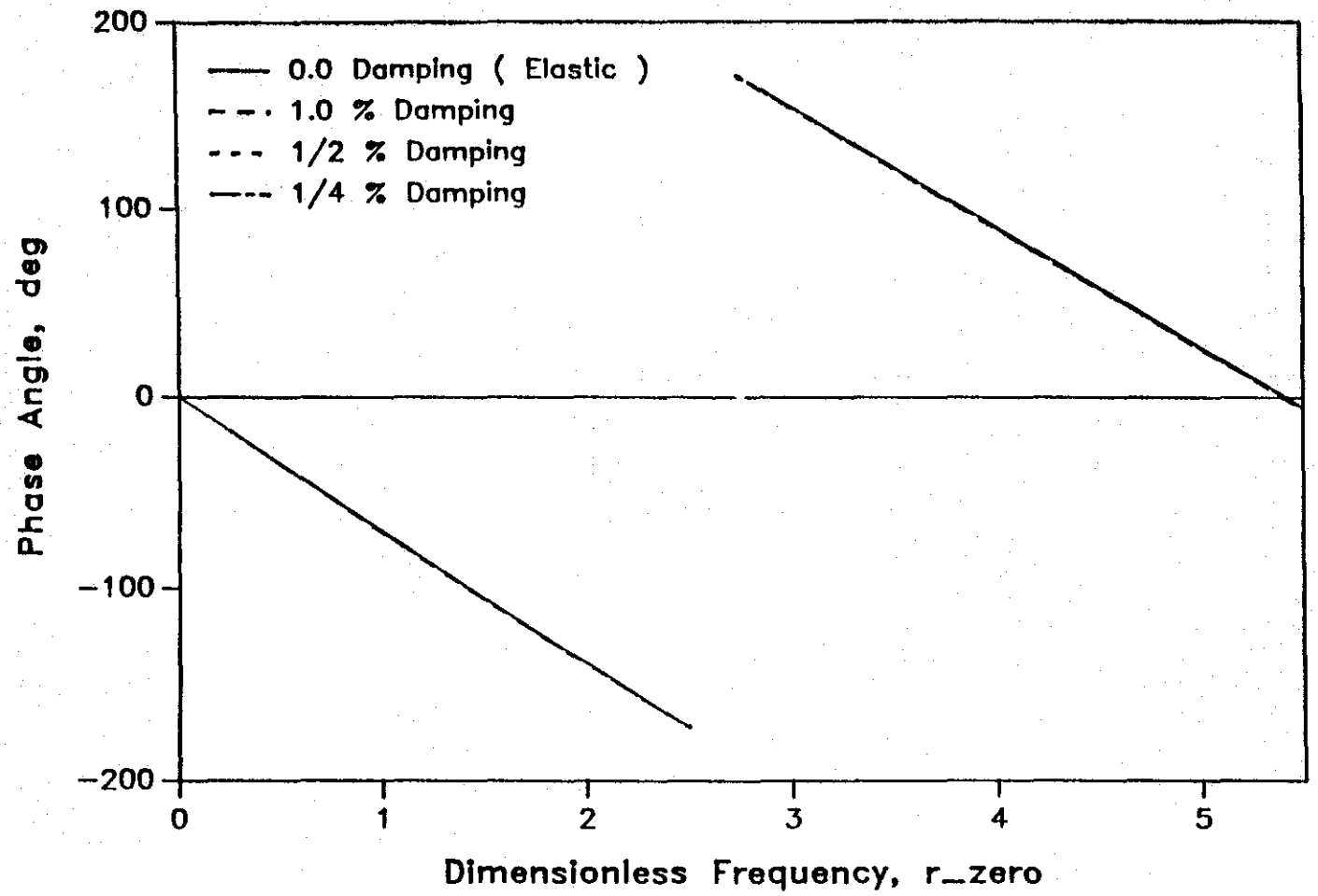

Figure 26. Phase Angle of Normal Surface Displacement Versus Dimensionless Distance (r_0) for a Point Surface Load: Poisson's Ratio = 0.33, Comparison of Theory and Computed Values.

ft. were generated from the SUP.C program. The computed results used a damping of 1/4 percent throughout.

The r = 0 results presented in magnitude |f| and phase ϕ_f versus a_o form are shown in Figures 27 and 28. The dimensionless frequency range (a_o) was from 0 to 0.5. This frequency range is less than the Reissner-Sung results discussed above. From Figure 27, one sees that the magnitude agrees within three significant figures. The phase angle in Figure 28 shows the same linear characteristic with the two results agreeing within about one-half of one percent.

The r = 6 ft. comparison computations shown in Figures 29 and 30 were done using the superposition integral for two cases: nn = 1 (point load) and nn = 5 (eleven elements) (Figure 15). Here the data is presented in $|f_r|$, ϕ_{fr} versus r_o format, used in the point load comparison. Figure 29 shows the magnitude plotted on an expanded scale. The magnitude increases somewhat with frequency similar to the point load response in Figure 23. The dimensionless frequency range was from r_o = 0 to 5.5. The magnitude response for nn = 5 shows uniform convergence to within about three significant figures. The nn = 1 or point load response showed fairly good agreement, considering the crudeness of the approximation of the loading distribution. The phase angle data in Figure 30 showed the nearly linear characteristic and the "jump" at the branch interchange seen in the point load response in Figure 24. The agreement for both nn = 1 and nn = 5 was so close that both the curves overlaid the UTFWIBM data to within the thickness of the pen line.

The r = 1 ft. comparison is shown on Figures 31 and 32, where the UTFWIBM data is compared to computed data for nn = 1 and nn = 2 (point load and four elements, respectively). The magnitude data in Figure 31 for nn = 2 agrees within three significant figures, and the agreement for the point load is suprisingly good, considering the closeness of the field point to the pressure disk. The magnitude response is quite flat for the indicated dimensionless frequency range of r_o from 0 to 0.9. The frequency range is lower than the r = 1 ft. comparison because the r is smaller (Equation [33]). The phase angle results show good agreement (within 1 percent) for the nn = 2 results.

A further study of the r = 1 ft. responses was conducted to test the

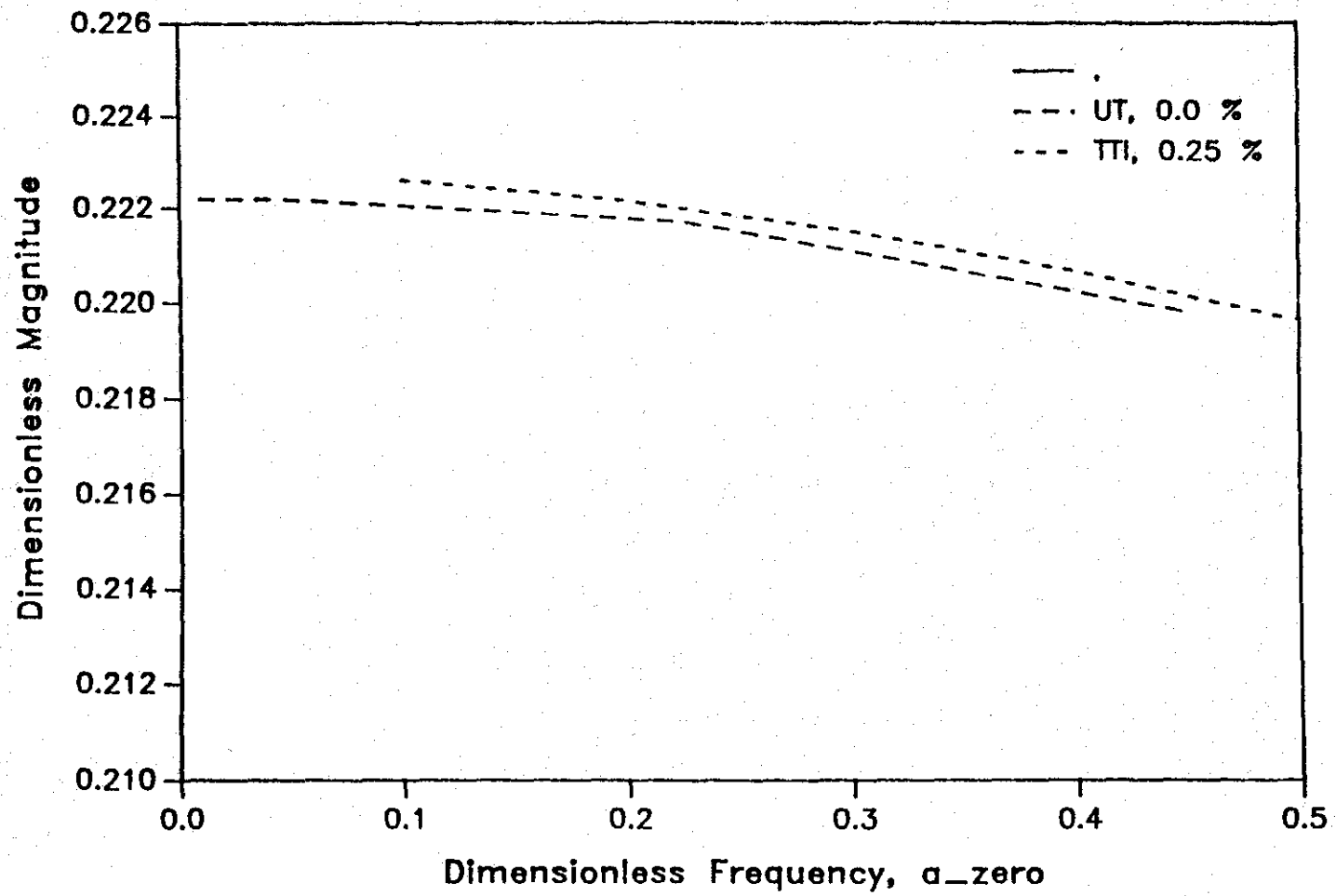

Figure 27. Magnitude of Dimensionless Normal Surface Displacement at r=0 Versus Dimensionless Frequency (a_0) for a Uniform Pressure Distribution (Poisson's Ratio = 0.3); Comparison of Computed Values.

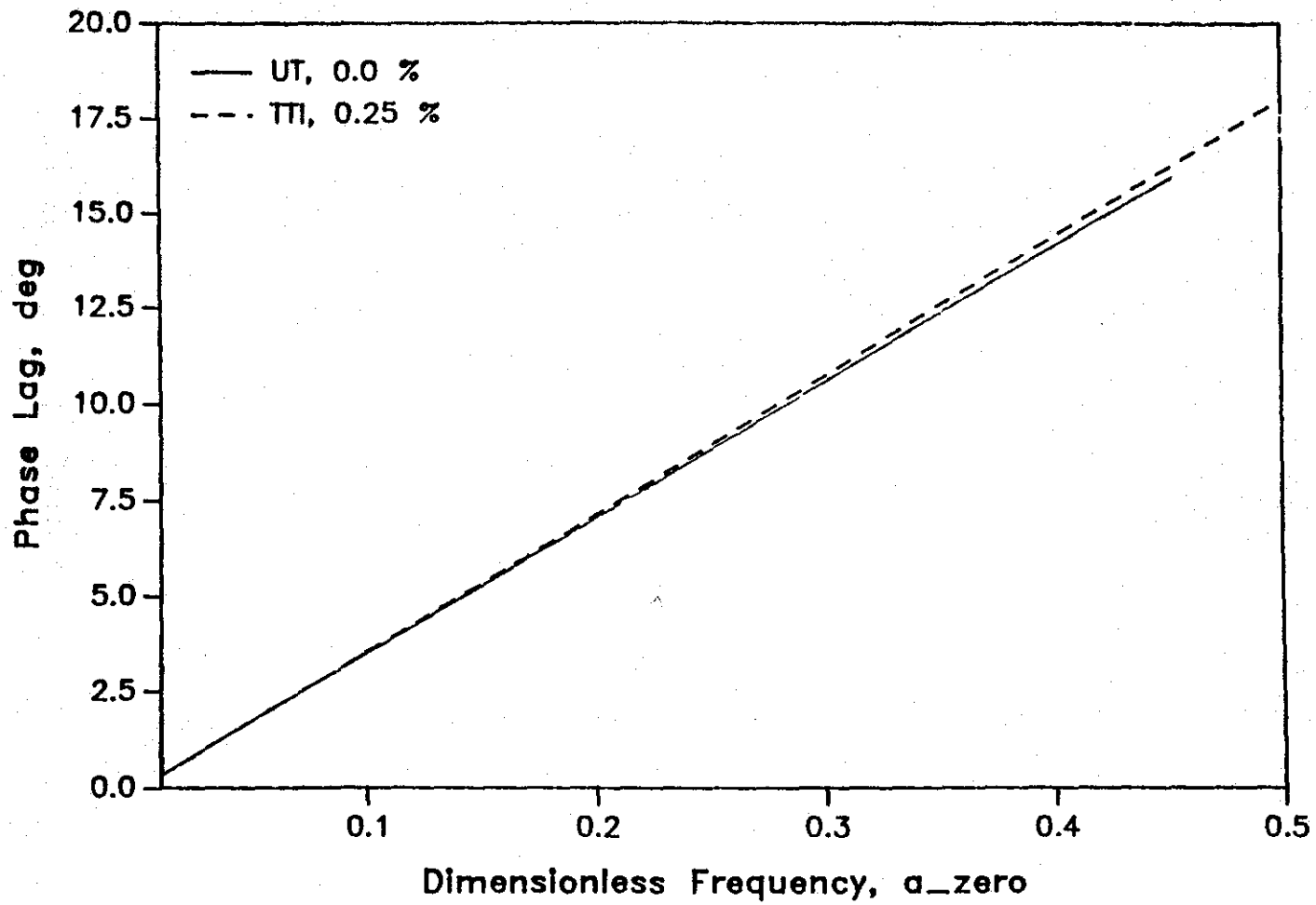

Figure 28. Phase Angle of Normal Surface Displacement at r=0 Versus Dimensionless Frequency (2_0) for a Uniform Pressure Distribution (Poisson's Ratio = 0.3); Comparison of Computed Values.

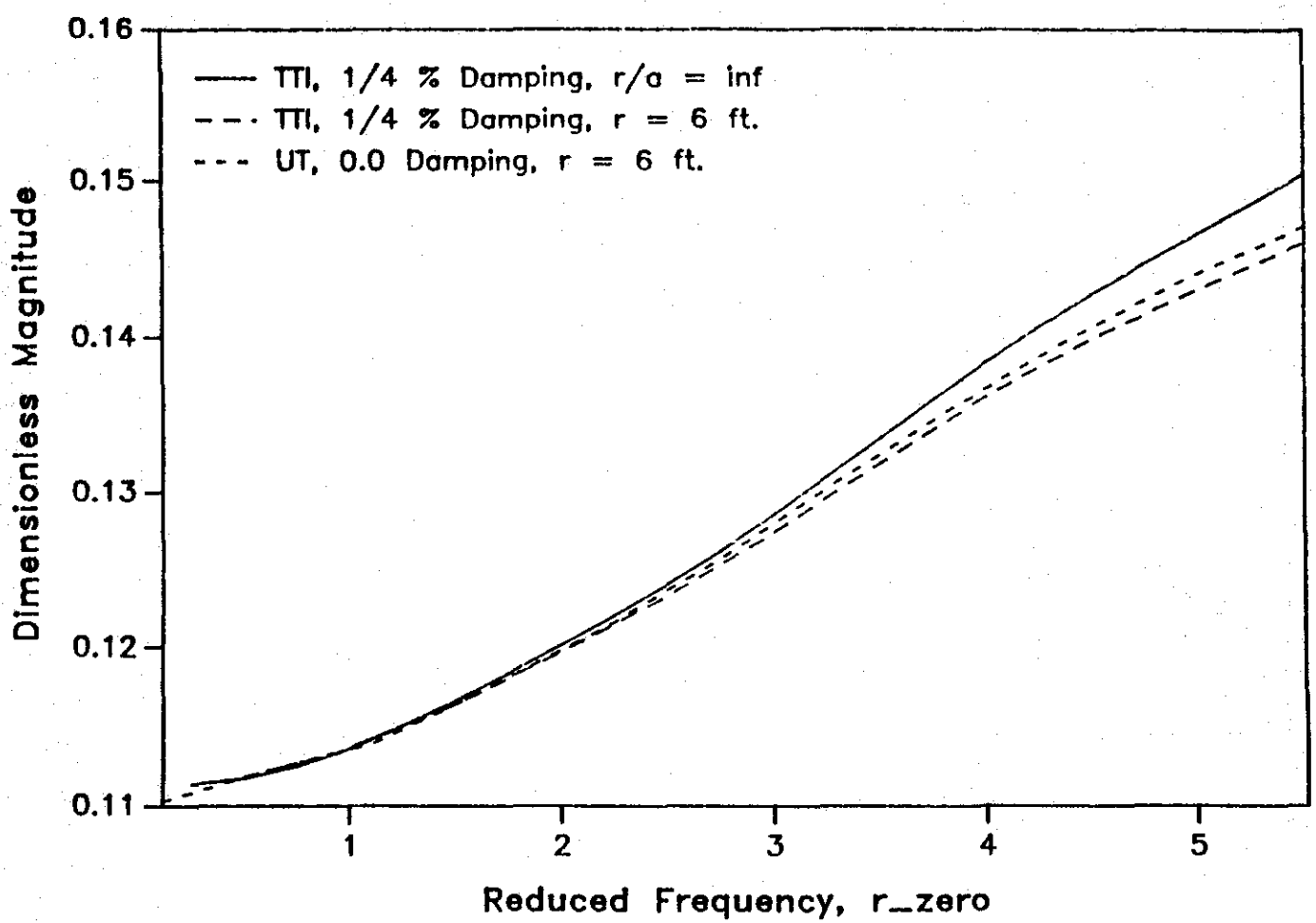

Figure 29. Magnitude of Normal Surface Displacement at r=6 ft. Versus Dimensionless Frequency (r_0) for a Uniform Pressure Distribution (Poisson's Ratio = 0.3); Comparison of Computed Values.

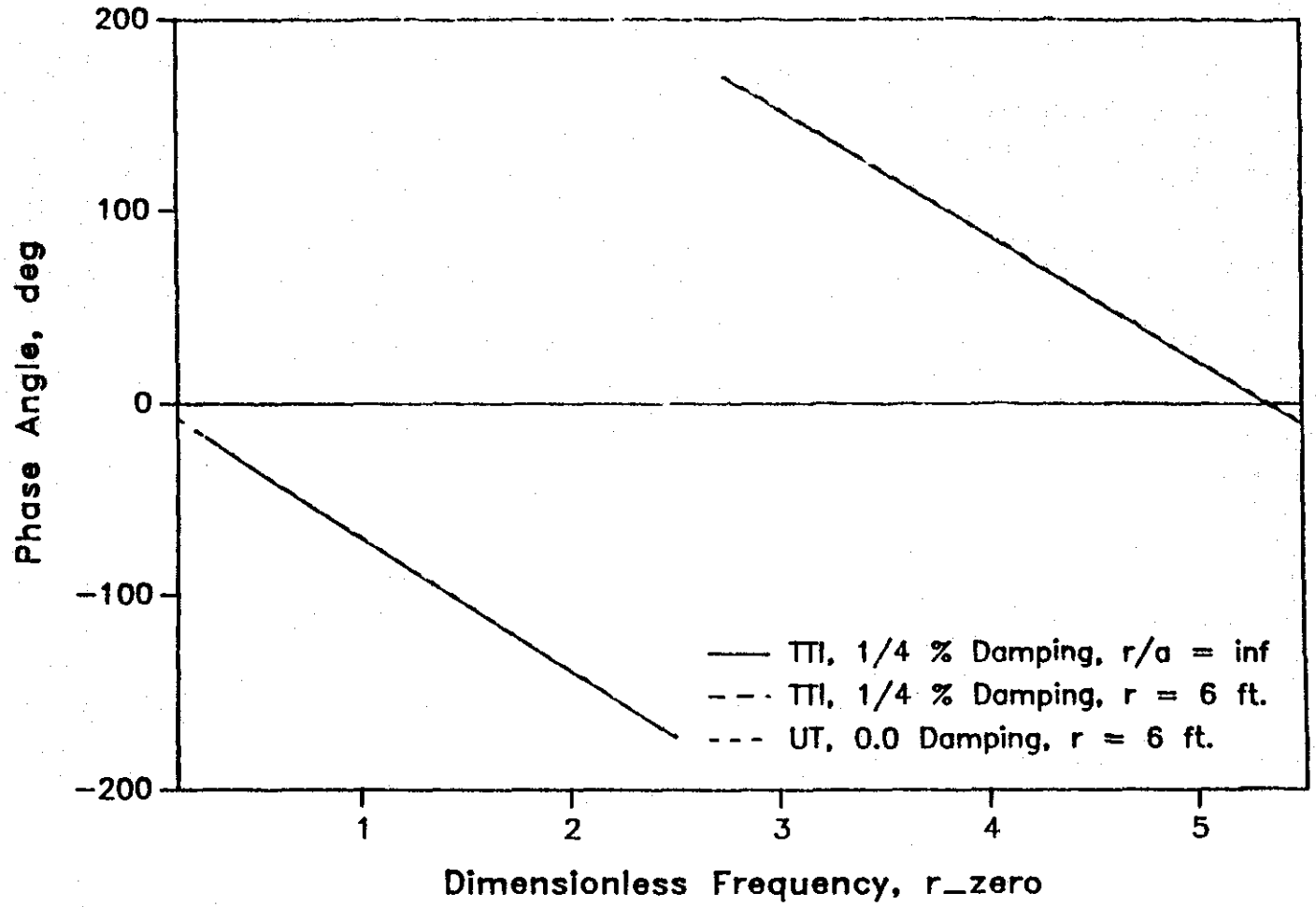

Figure 30. Phase Angle of Normal Surface Displacement at r=1 ft. Versus Dimensionless Frequency (r_o) for a Uniform Pressure Distribution (Poisson's = 0.3); Comparison of Computed Values.

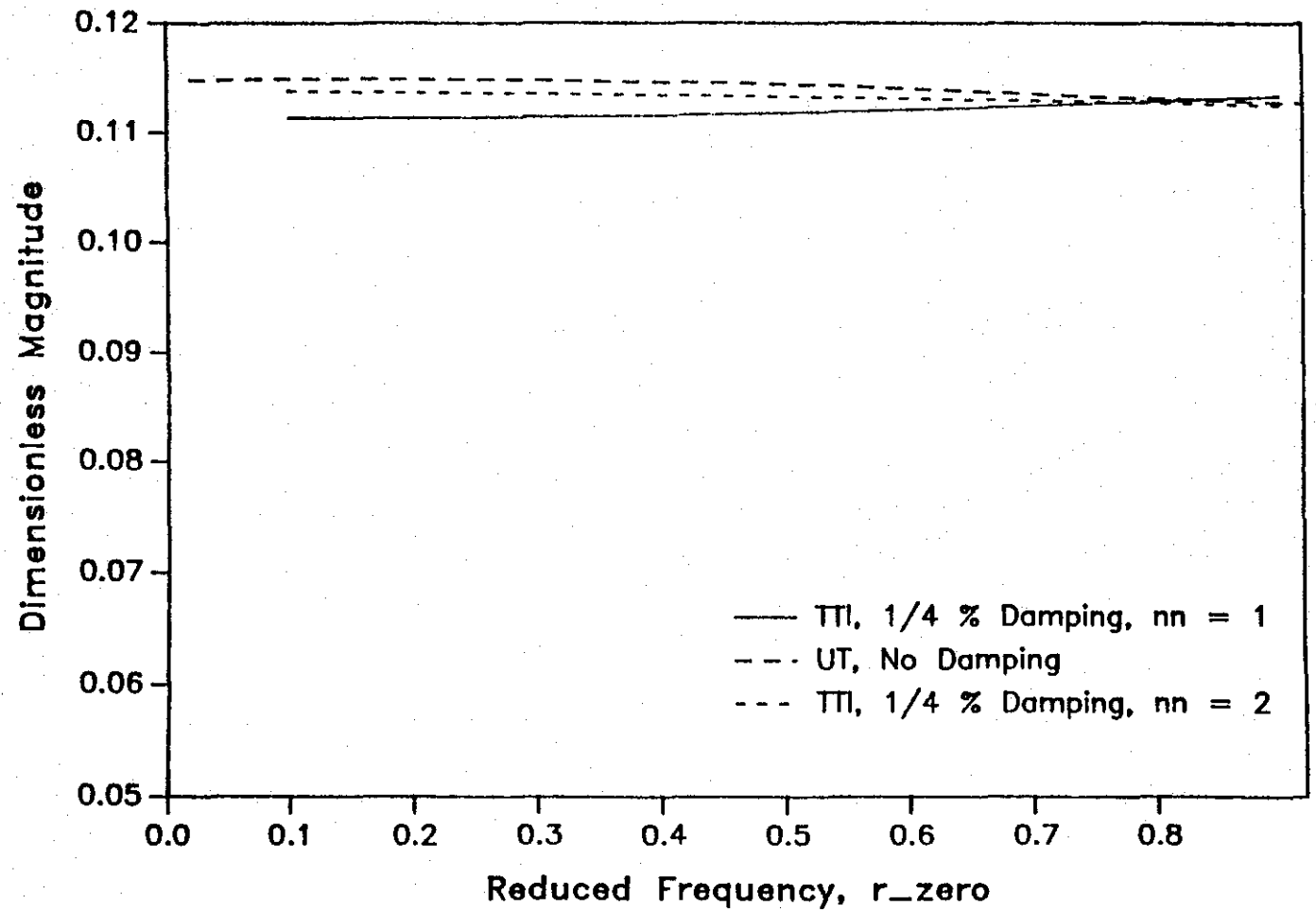

Figure 31. Magnitude of Normal Surface Displacement at r=1 ft. Versus Dimensionless Frequency (r_o) for a Uniform Pressure Distribution (Poisson's Ratio = 0.3). Comparison of Computed Values.

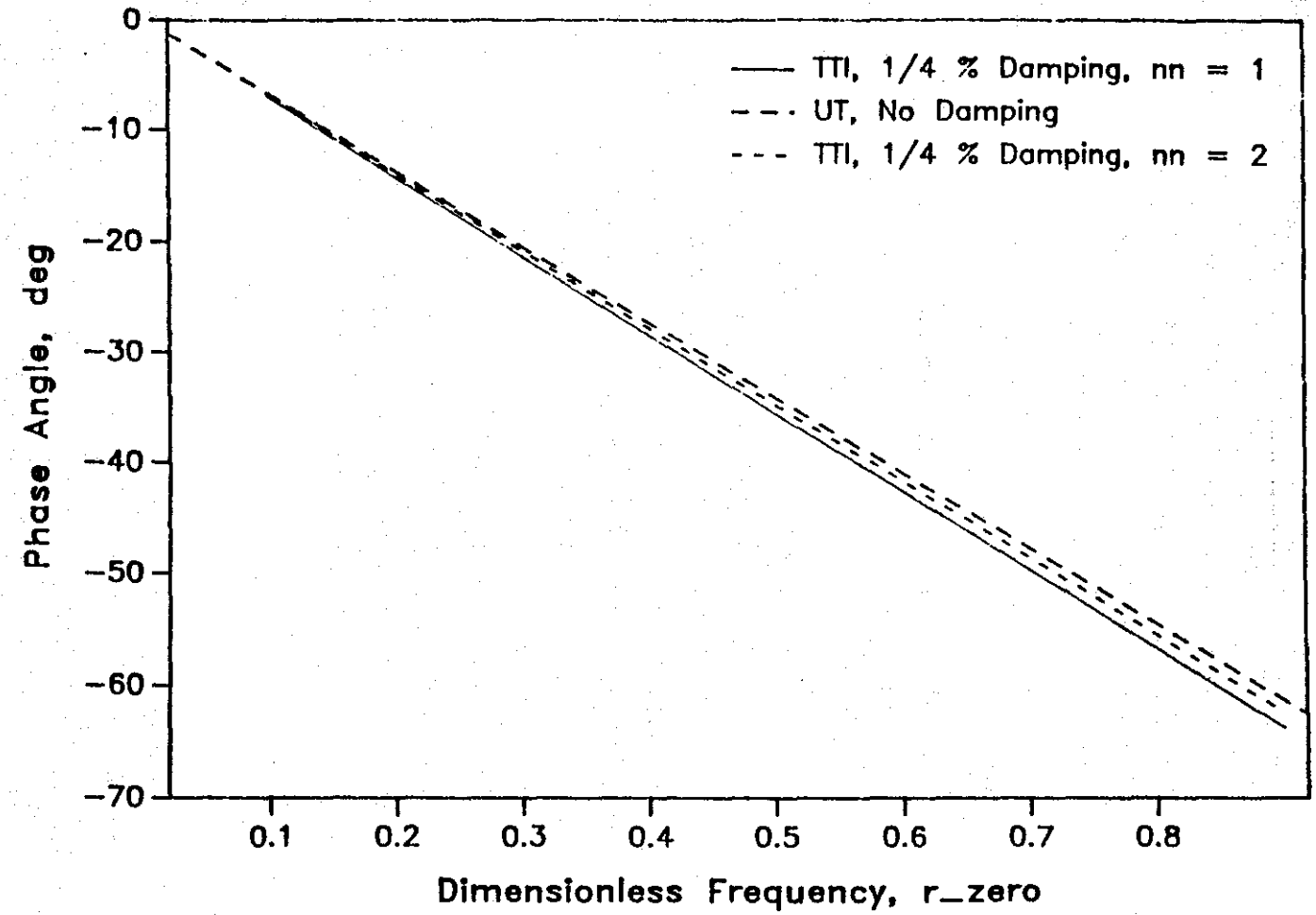

Figure 32. Phase Angle of Normal Surface Displacement at r=1 ft. Versus Dimensionless Frequency (r_0) for a Uniform Pressure Distribution (Poisson's Ratio = 0.3); Comparison of Computed Values.

convergence of the superposition program as the number of area elements was increased. In addition to the previous nn = 1 and nn = 2 cases, nn = 5 (9 elements) and nn = 9 (17 elements) were run (Figure 15). The results are shown in Figures 33 and 34 for magnitude and phase angle, respectively. The magnitude results show even closer agreement to the UTFWIBM results for nn = 5 and nn = 9 (within one-half of one percent). Both the nn = 5 and nn = 9 curves overlaid each other for both magnitude and phase curves, indicating convergence with respect to element size. A significant improvement in agreement is seen going from nn = 2 to nn = 5 for both magnitude and phase. This indicates that future computations should be done for nn = 5 for the r = 1 ft. case.

Summary

The three comparison studies show that the computed results agree well with data from three independent sources. The Reissner-Sung comparison shows agreement with elastic theory as the damping approachs zero for r = 0 response to the uniform pressure distribution, verifying the SCR.C program. The point source comparison study shows that as damping approaches zero, the DELTA.C program agrees with Wong's elastic half-space results. Finally, the comparison with the approximate UTFWIBM solution for uniform loading and r = 1 and 6 ft. verified the superposition program which uses the point load response as a Green's function or elemental solution.

The comparison studies in general indicated that computed values for the lowest damping agreed with undamped (elastic) results to within two to three significant figures. This does not mean that the SCALPOT programs are only accurate to two to three significant figures. The actual accuracy of the results should be around six significant figures. However, the SCALPOT computer program was developed for damping of one precent or higher and is therefore not well suited for simulating elastic responses. This is because the I_1 integral term requires a closer spacing of ordinates as damping decreases. As mentioned in Chapter V, the I_1 integral subdivision was 3000 intervals for a damping of 1/4 percent. To achieve significantly better agreement would have required extremely low

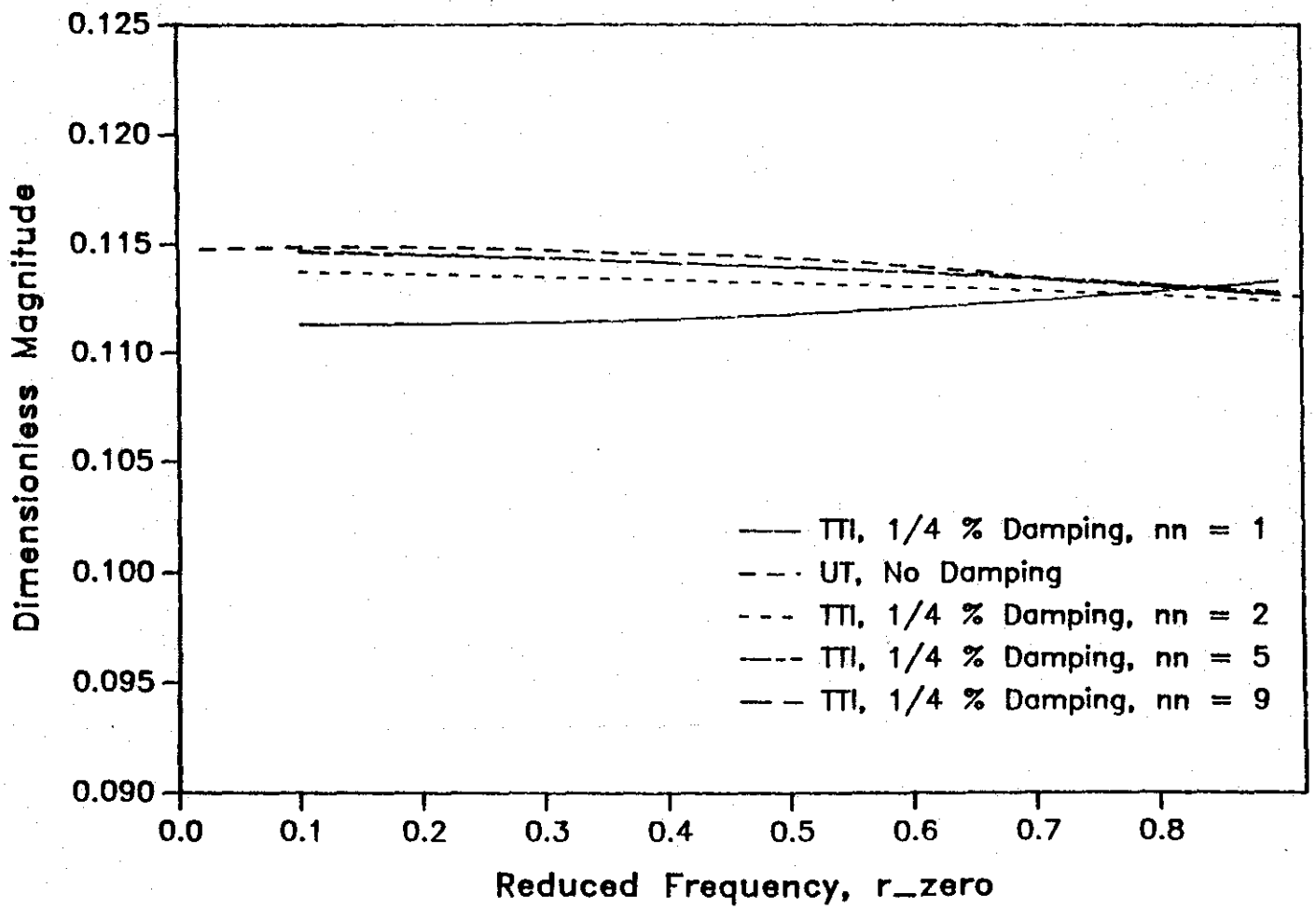

Figure 33. Magnitude of Normal Surface Displacement at r = 1 ft. Versus Dimensionless Frequency (r_0) for a Uniform Pressure Distribution (Poisson's Ratio = 0.3); Convergence Study for Superposition.

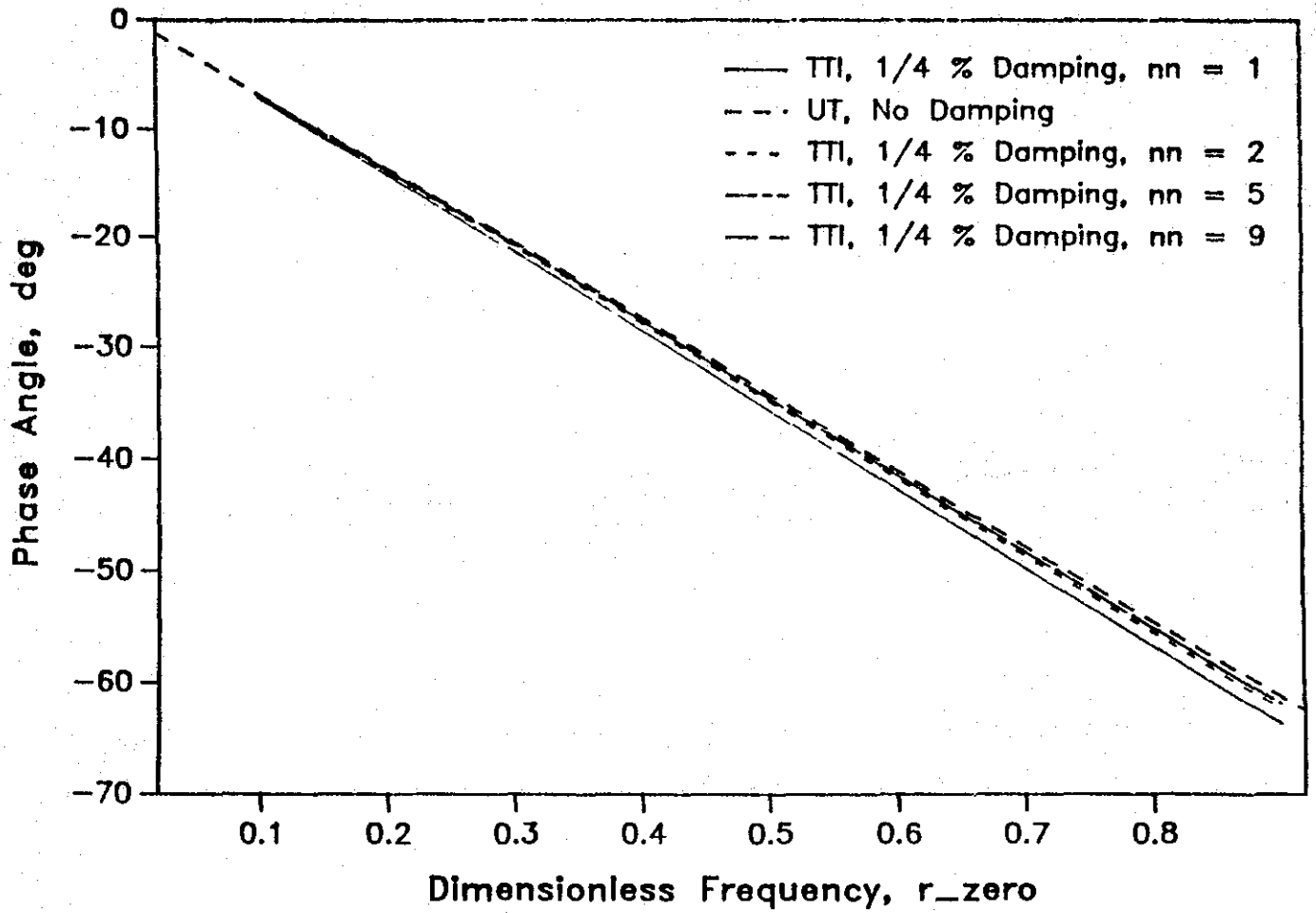

Figure 34. Phase Angle of Normal Surface Displacement at r=1 ft. Versus Dimensionless Frequency (r_0) for a Uniform Pressure Distribution (Poisson's Ratio = 0.3); Convergence Study for Superposition.

damping - 1/100 percent or lower. This would have increased computer CPU time inordinately, so the approach of decreasing damping in steps.

CHAPTER VII

SUMMARY AND CONCLUSIONS

In Chapter I, background information on Falling-Weight Deflectometer testing of asphaltic concrete highway pavements is given. Current and potential uses of FWD data are discussed. Preliminary results are presented on FWD dynamic testing, using deflection data from the TTI Pavement Test Facility Section 9. These results show the effect of damping on pavement frequency-response functions. This indicates that obtaining additional information from dynamic testing is feasible.

Chapter II discusses related work on dynamic analysis of layered elastic and viscoelastic media. The pavement dynamics problem as measured by the FWD is shown to be a near-field or intermediate-field problem requiring different integration techniques than far-field problems arising in seismic work. The discussion shows that a matrix approach to the multilayered formal solution using three-dimensional, viscoelastic vector field equations is most appropriate. Integration of the formal solution is shown to be best treated by direct numerical integration using a newly developed method of estimating truncation error.

The integral expressions for the surface displacement resulting from an oscillatory surface pressure distribution are derived in Chapter III. The approach uses the frequency domain, three-dimensional Navier equations for a homogeneous, isotopic, viscoelastic medium. Solutions are obtained in terms of scalar potential functions that reduce the problem to solving two scalar Helmholtz equations in a cylindrical polar coordinate system with axial symmetry. Solutions are obtained in the form of a Fourier-Bessel integral expansion by applying appropriate stress boundary conditions on the surface of the half-space. The FWD load pressure distribution is assumed to be circular and uniform. The resulting expression for the normal surface displacement is expressed as a wavenumber integral with two oscillatory Bessel functions. The overall problem is split up into two simpler problems, each involving a wavenumber integral with just one Bessel function for convenience in the subsequent integration. A superposition integral representation, using a point load response

function, is used to solve for the uniform load response for nonzero radial distances. Finally, the displacements are expressed in terms of dimensionless quantities.

The method of integration is described in Chapter IV. The two integral forms needed for the solution are treated the same. The integral must be evaluated numerically to a specified level of accuracy, taking into account the effect of truncation of the infinite upper limit, the oscillations due to the Bessel function, the slowness of the convergence of the integral, and the singular behavior of the integrand because of pole and branch points. The method of integration requires that some damping be present in the medium. The integrals are broken up into three terms: the first one includes all the pole and branch singularities; the second term integrates between zero-crossings of the Bessel function up to the truncation point that occurs at a specified number of cycles of oscillation of the integrand; and the third term is the truncation error estimate that uses a modified form of Zhongjin's (1987) method.

The computer programs developed for the solution are described in Chapter V. Three main programs were developed, along with associated "header" files used for auxiliary computations. The complete set of programs and files is referred to as the SCALPOT program (for Scalar Potential). The complex algebra and Bessel function modules are described. The three main programs, SCR.C, DELTA.C, and SUP.C, are shown in block diagram form. Since the structure of all three programs is similar, only the most complicated (SCR.C) is described. The purpose of each module is described in detail.

Results of the validation study are shown in graphical form and discussed in Chapter VI. Each of the programs, SCR.C, DELTA.C, and SUP.C, were verified using results of three separate investigators. The programs SCR.C and DELTA.C were compared to published results for an elastic half-space. These programs were verified by showing that the results converged uniformly to the elastic case as the damping approached zero.

The program SUP.C was verified by comparison with computed results from an approximate solution developed at University of Texas at Austin. The convergence of the superposition algorithm as a function of the number

of surface elements was demonstrated as well.

CONCLUSIONS

A computer algorithm SCALPOT, consisting of a set of programs and linked files, has been developed that computes responses for physical and geometrical conditions simulating the Dynatest Falling-Weight Deflectometer. The results are for a uniform (unlayered), viscoelastic halfspace, although the integration method was designed to be applicable to the multilayered problem which will be treated in Part II of the programming effort. The program has been verified using the results of three previous independent investigations.

REFERENCES

Abramowitz, M. and Stegun, I.A., (1972) Handbook of Mathmatical Functions, Dover, New York.

Apsel, R.J., (1979) "Dynamic Green's function for Layered Media an Applications of Boundary-Value Problems," Ph.D. Thesis, Unive California, San Diego, La Jolla, California.

Apsel, R.J. and Luco, J.E., (1983) "On the Green's Function for a Half-Space, Part II," Bulletin of the Seismological Society o America, Vol. 73, pp. 931-951.

Arnold, R.N., Bycroft, G.N. and Warburton, G.B., (1955) "Forced Vi tions of a Body on an Infinite Elastic Solid," Journal of App Mechanics, Transactions of ASME 77, 391-401.

Brekhovskikh, L.A., (1980) Waves in Layered Media, Second Ed., Aca Press, New York, New York.

Biot, M.A., (1965) Mechanics of Incremental Deformations, John Wil Sons, New York.

Biot, M.A., (1963) "Continuum Dynamics of Elastic Plates and Multi Solids Under Initial Stress," Journal of Mathematocal Mechani 12, pp. 793-810.

Das, B.M., (1983) Fundamentals of Soil Dynamics, Elsevier, New Yor

Davis, P.J. and Rabinowitz, P., (1975) Methods of Numerical Integr Academic Press, New York.

Dravinski, M. and Mossessian, T.K., (1988) "On Evaluation of the G Functions for Harmonic Line Loads in a Viscoelastic Half-Spac International Journal for Numerical Methods in Engineering, V pp. 823-841.

Ewing, W.M., Jardetzki, W.S., and Press, F., (1957) Elastic Waves Layered Media, New York, McGraw-Hill Book Company, Inc.

Filon, L.N.G. (1928-29), "On a Quadrature Formula for Trigonometri Integrals", Proceedings of the Royal Society of Edinburgh, Vo pp. 1743-1761.

Fung, Y.C., (1965) Foundation of Solid Mechanics, Prentice-Hall, Englewood Cliffs.

Hansen, W.W. and Beckerley, J.G., (1937) "Radiation from an Antenn a Plane Earth of Arbitrary Characteristics," Physics 7, pp. 2

Haskell, N.A., (1953) "The Dispersion of Surface Waves on Multilayer Media," Bulletin of the Seismological Society of America, Vol. 43, pp. 15-45.

Jardetzki, W.S., (1953) "Period Equation for an N-Layered Half-space and Some Related Questions," Lamont Geological Observatory Technical Report No. 29, Columbia University.

Kennett, B.L.N. (1983), Seismic Wave Propagation in Stratified Media, Cambridge University Press, London.

Kernighan, B.W. and Ritchey, D.M. (1978), The C Programming Language, Prentice-Hall, Englewood Cliffs.

Kausel, E., (1986) "Wave Propagation in Anisotropic Layered Media," International Journal for Numerical Methods in Engineering, Vol. 23, pp. 1567-1578.

Kausel E., and Peek, R., (1982) "Dynamic Loads in the Interior of a Layered Stratum: An Explicit Solution," Bulletin of the Seismological Society of America, Vol. 72, No. 5, 1459-1481, October.

Kausel, E. and Roesset, J.M. (1981) "Stiffness Matrices for Layered Soils", Bulletin of the Seismological Society of America, Vol. 71, pp. 1743-1761.

Kausel, E., Roesset, J.M. and Waas, G., (1974) "Forced Vibrations of Circular Foundations on Layered Media", Report R74-11, Department of Civil Engineering, Massachusetts Institute of Technology.

Kundu, T. (1983) "Computation of Surface Motion in a Stratified Half-Space", Ph.D. Dissertation, School of Engineering and Applied Science, University of California, Los Angeles.

Kundu, T. and Mal, A.K. (1985) "Elastic Waves in a Multilayered Solid Due to a Dislocation Source," Wave Motion, Vol. 7, pp. 459-471.

Lamb, H., (1904) "On the Propagation of Tremors Over the Surface of an Elastic Soil," Philosophical Transactions of the Royal Society, Vol. 203, pp. 1-42.

Landau, L.D. and Lifschitz, E.M., (1970) Theory of Elasticity, Addison-Wesley, Reading, Massachusetts.

Longman, I.M., (1956) "Note on a Method for Computing Infinite Integrals of Oscillatory Functions," Proceedings of the Cambridge Philosophical Society, Vol. 52, pp. 764-768.

Luco, J.E. and Apsel, R.J., (1983) "On the Green's Functions for a Layered Half-Space, Part I," Bulletin of the Seismological Society of America, Vol. 73, pp. 909-929.

Lytton, R.L., Roberts, F.L., and Stoffels, S.M., (1986) "Determination of Asphaltic Concrete Pavement Structural Properties by Nondestructive Testing," Final Report, Phase I, NCHRP Project 10-27, July.

Magnuson, A.H., (1975a) "Acoustic Response in a Liquid Overlying a Homogeneous Viscoelastic Half-Space," Journal of the Acoustical Society of America, Vol. 57, pp. 1017-1024.

Magnuson, A.H., (1975) "The Acoustic Response in a Liquid Layer Overlaying a Multilayered Viscoelastic Half-space," Journal of Sound and Vibration, Vol. 43, No. 4, pp. 659-669.

Papazian, H.S., (1961) "The Response of Linear Viscoelastic Materials in the Frequency Domain," (Dissertation), Report No. 172-2, Transportation Engineering Center, Engineering Experiment Station, The Ohio State University, Columbus, Ohio.

Pipkin, A.C., (1972) Lectures on Viscoelasticity Theory, Springer-Verlag, New York.

Reissner, E., (1936) "Stationare, Axialsymmetrische Durch Eine Schuttelnde Masseerregte Schwingungen Eines Homogenen Elastischen Halbraumes," Ingenieur-Archiv, Vol. 8 (Part 6), pp. 381-396.

Sommerfield, A., (1964a) Mechanics of Deformable Bodies, Lectures on Theoretical Physics, Vol. II, Academic Press, New York.

Sommerfield, A., (1964b) Partial Differential Equations in Physics, Lectures on Theoretical Physics, Vol VI, Academic Press, New York.

Sung, T.Y., (1953) "Vibration in Semi-Infinite Solids Due to Periodic Surface Loadings," Symposium on Dynamic Testing of Soils, ASTM, STP 156, pp. 35-68.

Thomson, W.T., (1950) "Transmission of Elastic Waves Through a Stratified Solid Medium," Journal of Applied Physics, Vol. 21, pp. 89-93.

Uzan, J., Lytton, R.L., and Germann, F.P., (1988) "General Procedure for Backcalculating Layer Moduli," Prepared for the First Symposium on NDT of Pavements and Backcalculation of Moduli.

Waas, G. (1972), "Linear Two-Dimensional Analysis of Soil Dynamics Problems in Semi-Infinite Layer Media," Ph.D. Thesis, University of California, Berkeley.

Wong, H.L., (1975) "Dynamic Soil-Structure Interaction," Report EERL-75-01, Earthquake Engineering Research Laboratory, California Institute of Technology, Pasadena.

Zhongjin, Y., (1987) "A Method of Finite Integrals of Oscillating Functions," Communications in Applied Numerical Methods, Vol. 3, pp. 1-4.